

NASA Contractor Report 4573

1N:36  
209768  
103P

# Development of Lasers Optimized for Pumping Ti:Al<sub>2</sub>O<sub>3</sub> Lasers

---

*Glen A. Rines and Richard A. Schwarz*

(NASA-CR-4573) DEVELOPMENT OF  
LASERS OPTIMIZED FOR PUMPING  
Ti:Al<sub>2</sub>O<sub>3</sub> LASERS Final Technical  
Report, 10 Apr. 1991 - 17 Dec. 1993  
(Schwartz Electro-Optics) 103 p

N94-26705

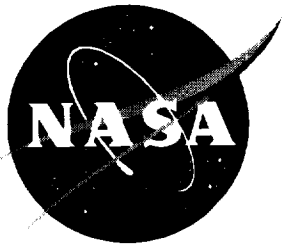
Unclass

H1/36 0209768

Contract NAS1-19304  
Prepared for Langley Research Center

March 1994





# Development of Lasers Optimized for Pumping Ti:Al<sub>2</sub>O<sub>3</sub> Lasers

---

*Glen A. Rines and Richard A. Schwarz  
Schwartz Electro-Optics, Inc. • Concord, Massachusetts*



## Table of Contents

1	Introduction .....	1
2	Executive Summary .....	1
3	Background .....	4
4	Review of Phase I Technical Objectives and Results .....	6
5	Phase II Technical Objectives .....	7
6	Phase II Work Plan .....	8
7	Phase II Statement of Work .....	11
8	CW Laser Development .....	12
8.1	Preliminary Design Considerations .....	12
8.2	CW Gain Module Design and Construction .....	13
8.2.1	Diode Laser Characteristics .....	13
8.2.2	Collimating and Focusing Optics: Design and Performance .....	17
8.2.3	Gain Element Characteristics .....	25
8.3	Laser Development and Performance at the Fundamental Wavelength .....	30
8.3.1	Diode-Pumped Performance vs. $\text{Ti:Al}_2\text{O}_3$ -Pumped Performance .....	30
8.3.2	Resonator Design Issues .....	37
8.3.3	Ring Resonator Design and Performance .....	43
8.3.4	Standing-Wave Resonator Design and Performance .....	44
8.4	Laser Performance at the Second Harmonic Wavelength .....	48
8.4.1	Intracavity Type I SHG Using LBO .....	48
8.4.2	Intracavity Type II SHG Using KTP .....	51
8.4.3	Power Stability and Intensity Noise .....	54
8.4.4	Analysis of SHG Results .....	55
8.5	Demonstration of an All-Solid-State, CW, $\text{Ti:Al}_2\text{O}_3$ Laser .....	57
8.6	Summary of CW Laser Results .....	58
9	Pulsed Laser Development .....	59
9.1	Preliminary Design Considerations for the Diode-Laser-Pumped System .....	59
9.2	Pulsed Gain Module Design and Construction .....	59
9.2.1	Diode Laser Characteristics .....	59
9.2.2	Pumping Configurations .....	60
9.3	Laser Performance, Normal-Mode and Conventionally Q-switched .....	63
9.4	Actively Controlled Q-switch Development .....	71
9.5	Summary of Pulsed Laser Results .....	80
10	Summary and Conclusions .....	81
11	References .....	81
12	List of Acronyms and Abbreviations .....	83

13	Appendix A: 10-W Diode Laser Pump Profiles .....	84
14	Appendix B: CW Laser Development -- Recent Results .....	94
14.1	Increased SHG Output Power .....	94
14.2	High-Frequency Noise Measurements .....	95

## 1 Introduction

This document is the Final Technical Report for a NASA-funded, Phase II, Small Business Innovation Research (SBIR) contract (contract number NAS1-19304). The work described in this report was carried out by the Research Division of Schwartz Electro-Optics (SEO), located in Concord, Massachusetts. The report covers the entire period of performance for the Phase II contract, which began on 10 April 1991 and ended on 17 December 1993. This contract was the continuation of the work that began in Phase I under contract number NAS1-19003.

The goal of this SBIR project was to develop two types of pump lasers optimized for use in a  $\text{Ti:Al}_2\text{O}_3$  lidar system: 1) a diode-laser-pumped, continuous-wave (cw), green laser for the lidar master oscillator, and 2) a diode-laser-pumped, high-energy, pulsed, green laser with a 100-ns pulsewidth (nominal) for the lidar slave oscillator. These are the pump lasers needed for the single-frequency, high-energy,  $\text{Ti:Al}_2\text{O}_3$  lidar transmitter technology that is being developed by NASA Langley Research Center (LaRC) [1]. The Phase I project succeeded in accurately defining the specific pump laser requirements and in beginning the design work on these two lasers. The Phase II project succeeded in demonstrating prototype lasers, in our research laboratory, that provide the required laser output characteristics for both the cw and the pulsed pump lasers.

In keeping with one of the overall SBIR program objectives, SEO intends to continue the development of these lasers beyond the now completed Phase II contract, and to ultimately produce commercial lasers either as scientific laser products or as components of more sophisticated laser systems such as differential absorption lidar (DIAL) systems.

The remainder of the report is organized as follows. The most significant technical results of the Phase II research effort are stated in summary form in Section 2 along with comments regarding future plans for this technology. Section 3 gives the background information that is necessary to understand the basis for and the significance of the technology developed in this SBIR project. Sections 4 through 7 review information that was in the Phase II proposal to provide the reader with the background information necessary to evaluate the success of the Phase II work in the context of the original proposal. Sections 8 and 9 contain the details of the theoretical and experimental work that was carried out to meet the technical objectives of the Phase II contract. Section 10 summarizes the technical results and states our conclusions and plans for future work. The references for the entire document are listed in Section 11. A list of acronyms and abbreviations is provided in Section 12. Appendices that contain additional technical data follow in Sections 13 and 14.

## 2 Executive Summary

As stated above, this project involved the development of two very different lasers, namely, the two pump lasers needed to make a  $\text{Ti:Al}_2\text{O}_3$  lidar-transmitter design practical on space-based platforms: 1) a pump for the  $\text{Ti:Al}_2\text{O}_3$  master oscillator and, 2) a pump for the

Ti:Al<sub>2</sub>O<sub>3</sub> slave oscillator. The technical reasons for this work are described very briefly below. For a complete description of the lidar transmitter design, and the design philosophy that it is based on, see Ref. 1 and Ref. 2.

### **Technical Goals**

The overall goal of the master-oscillator, pump-laser effort was to produce an all-solid-state, single-frequency, broadly tunable, cw, Ti:Al<sub>2</sub>O<sub>3</sub> laser with enough output power to reliably injection seed a high-energy, gain-switched, Ti:Al<sub>2</sub>O<sub>3</sub>, unstable-resonator oscillator. The overall goal of the slave-oscillator pump-laser effort was to produce an all-solid-state, pulsed laser with a nominal 100-ns pulsewidth. This is in contrast to the typical pulsewidths for conventionally Q-switched, frequency-doubled, Nd lasers, which are on the order of 10 ns. The factor of ten greater pulsewidth can significantly reduce the likelihood of optical damage in the Ti:Al<sub>2</sub>O<sub>3</sub> slave oscillator, increasing the system reliability. The results of the master-oscillator effort are summarized below, followed by a summary of the slave-oscillator work.

### **Master-Oscillator Pump Laser**

The master oscillator is a critical subsystem of the lidar transmitter design. The master oscillator, via the well-known injection-seeding mechanism, constrains the high-energy, slave oscillator to operation on a single-longitudinal-mode, hence allowing the final output of the Ti:Al<sub>2</sub>O<sub>3</sub> lidar transmitter to be both near-diffraction-limited in spatial beam quality and near-transform-limited in terms of spectral linewidth. This optimum performance level is required for long-range, DIAL, remote-sensing applications. Furthermore, if the lidar system is to be space-based, all of the lasers used in the system must be solid state lasers in order to meet the requirements of reliability, compactness, efficiency and operational lifetime.

The earlier laboratory-development work on the Ti:Al<sub>2</sub>O<sub>3</sub> master oscillator that was carried out at SEO relied on Ar-ion lasers as the optical pump source. While the Ar-ion laser is extensively used in laboratory environments throughout the world, it is an extremely inefficient laser system. In practice this means these lasers are large in size, require high capacity cooling (for the laser head and the power supplies) and consume a great deal of electrical power. These problems absolutely preclude their use in space-based lidar systems. Hence, one goal of this project was to develop a very compact, efficient "replacement" for the Ar-ion laser. The new laser would have to produce a near-diffraction-limited, cw output beam in the blue-green region of the spectrum where the Ti:Al<sub>2</sub>O<sub>3</sub> absorption is strong.

It was clear at the outset of the Phase I project that the solution would be a diode-laser-pumped, cw, Nd-laser operating at a fundamental wavelength of 1 micron and subsequently frequency doubled to produce a green pump beam. Diode-laser-pumping of Nd-lasers was, in fact, already a rapidly advancing technology area at that time. The challenge for this work was to identify a specific laser design that would meet the specific requirement of our Ti:Al<sub>2</sub>O<sub>3</sub> master oscillator and carry out experiments to demonstrate "reduction to practice". This involved selection of a crystal host for the Nd ion; selection of a pumping geometry (transverse vs. longitudi-



nal); selection of a mounting/cooling geometry for the gain medium; selection of a second harmonic generation (SHG) crystal; selection of a resonator design to accommodate all these components; and, the design and testing of all of the optical and opto-mechanical hardware necessary for the final all-solid-state, master-oscillator demonstration at the end of the program.

The details of the experimental effort for the cw laser are given in Section 8. The important results are summarized here.

The final design arrived at for the cw laser was a longitudinally-pumped, Nd:YLF laser in a standing-wave resonator with intracavity SHG. The best results were obtained using LBO as the SHG crystal. We obtained greater than 900 mW of cw output power at 523.5 nm with 10 W of diode-laser pump power delivered to the Nd:YLF crystal (12 W total output from the diode-laser active area). We used this output to pump a cw, single-frequency, Ti:Al<sub>2</sub>O<sub>3</sub>, ring laser. We obtained up to 16.5 mW of single-frequency, cw output power from the Ti:Al<sub>2</sub>O<sub>3</sub> laser. The output was tunable over a 120-nm wavelength region from 788 to 908 nm, which was limited on the short-wavelength end by the mirror coatings. (With a "short-band" mirror the laser would have tuned down to about 700 nm). This experiment demonstrates for the first time, to our knowledge, an all-solid-state, single frequency, Ti:Al<sub>2</sub>O<sub>3</sub> laser with sufficient output power to injection seed a high-energy oscillator over a 200-nm bandwidth.

### **Slave-Oscillator Pump Laser**

As stated at the beginning of this section, the purpose of the slave-oscillator-pump-laser work was to develop a pulsed, green laser with pulsewidths significantly longer than those produced by conventionally Q-switched, frequency-doubled, Nd lasers. The goal was to increase the reliability of the Ti:Al<sub>2</sub>O<sub>3</sub> slave oscillator by allowing a greater margin with respect to optical damage limits. The optimum pulsewidth for the gain-switched, unstable-resonator oscillator that is the slave oscillator in our lidar transmitter design [1,2] is on the order of 100 ns.

As with the master-oscillator pump, it is essential in space-based systems to employ diode-laser pumping. Therefore, on this project we worked on the development of both diode-laser-pumped oscillator designs and opto-electronics capable of controlling the dynamics of a Q-switched, Nd oscillator.

The details of the diode-laser-pumped oscillator design work are presented in Sections 9.1 through 9.3. The details of the pulsewidth-control work are given in Section 9.4. A summary of the results is given in the following paragraphs.

In the course of the diode-laser-pumped work we designed, fabricated, and tested two pump head configurations: a radial side-pumped head and a linear side-pumped head. Nd:YAG in a rod geometry was selected as the gain medium for the reasons given in Section 6. The radial and linear heads were evaluated in terms of gain distribution, normal-mode and Q-switched operation. We obtained up to 90 mJ of output energy from the radial head in normal-mode operation

and 40 mJ with "conventional" Q-switching (low-order, multi-transverse-mode). The total diode-laser pump energy was 350 mJ, hence the overall optical conversion efficiency was 26% for normal-mode operation and 11% for Q-switched operation.

The actively-controlled Q-switching (ACQS) effort was carried out using a flashlamp-pumped, Nd:YAG test bed. This was to allow maximum flexibility in the ACQS effort and to allow the diode-laser-pumped work to go on in parallel with and independent of the ACQS work. The intent was to integrate the ACQS hardware into the diode-laser-pumped oscillator at the end of the ACQS effort. We were not able to carry out this integration step within the time frame of the Phase II program. This is the next logical step in the development effort, which could be carried out in a Phase III effort at SEO or by NASA researchers.

The ACQS experiments succeeded in demonstrating pulse-stretching in a Q-switched Nd:YAG oscillator. We obtained greater than 50-mJ pulse energies in pulses with 100- to 200-ns pulsewidths (FWHM). This is suitable for use in a Nd:YAG amplifier chain for the generation of Joule-level output energies that are subsequently converted to the green region via SHG.

To summarize, the program succeeded in demonstrating, in laboratory laser experiments, the technical goals of the program: 1) an all-solid-state, broadly tunable, single-frequency, Ti:Al<sub>2</sub>O<sub>3</sub> master oscillator, and 2) a technique for obtaining "long" (nominally 100- to 200-ns FWHM) laser pulses from a Q-switched, Nd oscillator at energy levels commensurate with straightforward amplification to the Joule level.

### 3 Background

Over the last few years, Ti:Al<sub>2</sub>O<sub>3</sub> has emerged as a very useful and versatile solid-state laser medium. It has a single, broad absorption band around 490 nm and has demonstrated laser action from 660 to 1150 nm. It operates well in both cw and short-pulse oscillators provided an appropriate optical pumping technique is available. For cw operation and for reliable, pulsed oscillators, Ti:Al<sub>2</sub>O<sub>3</sub> lasers are optically pumped by another laser. (Flashlamp pumping is possible for pulsed oscillators, however, the short lamp pulse durations necessary severely limit the operational lifetime of the flashlamps and associated driver electronics.) The goal of this project is to develop lasers optimized for use as Ti:Al<sub>2</sub>O<sub>3</sub> pump lasers, that can be engineered for use on a space platform. Optimizing the lasers for this application means defining the pump beam characteristics needed by the Ti:Al<sub>2</sub>O<sub>3</sub> lasers and designing pump lasers with those characteristics. Furthermore, in order to meet the efficiency, reliability and lifetime requirements of space-based systems, the pump lasers must be diode-laser pumped.

The single-frequency, high-energy, Ti:Al<sub>2</sub>O<sub>3</sub>, lidar transmitter currently under development by NASA Langley Research Center [1] requires two types of pump lasers. These pump lasers must operate in the blue-green region near the peak of the Ti<sup>3+</sup> absorption band. The most viable solid state lasers in this region are neodymium (Nd) lasers operating around 1 micron that are frequency doubled to produce laser radiation at nominally 530 nm.

The master oscillator requires a cw (or quasi-cw) pump laser with a nominal output of 1 W. The gain-switched, high energy oscillator requires a pulsed pump with a per-pulse energy of about 2 J to produce 1 J of  $\text{Ti:Al}_2\text{O}_3$  output. The goal of this SBIR project is to develop pump lasers that are optimized for these requirements.

Given the short upper-state lifetime of  $\text{Ti:Al}_2\text{O}_3$ , cw operation can only be achieved with laser pumping. The most practical pump source for space-based, cw  $\text{Ti:Al}_2\text{O}_3$  lasers is a diode-laser-pumped, Nd-laser with efficient intracavity SHG. GaAlAs diode-laser technology has advanced rapidly in recent years, making the realization of an all-solid-state, cw  $\text{Ti:Al}_2\text{O}_3$  laser possible. On the Phase I program we generated a paper design for such a laser. On the Phase II program we reviewed our design in the context of recent diode-laser advances and relevant research publications on diode-laser-pumped Nd lasers. This design review led us to change our baseline design from the transversely pumped, Nd:YAG approach described in the Phase II proposal to a longitudinally pumped, Nd:YLF approach. Using this approach we developed, through a combination of modeling and experimental testing, a prototype, cw, green laser that produced greater than 900 mW in a near-diffraction-limited beam using a 12 W of diode-laser pump power. Using this laboratory laser we pumped a low-threshold, cw,  $\text{Ti:Al}_2\text{O}_3$  laser, thereby demonstrating a major advance in  $\text{Ti:Al}_2\text{O}_3$  laser technology: an all-solid-state, single-frequency, cw,  $\text{Ti:Al}_2\text{O}_3$  laser with an output adequate for injection-seeding a high-energy laser over a broad tuning range.

Pulsed operation of  $\text{Ti:Al}_2\text{O}_3$  is generally achieved by gain-switching a  $\text{Ti:Al}_2\text{O}_3$  oscillator using a frequency-doubled, Q-switched, Nd-laser pulse. Typically the Nd lasers have output pulsewidths of 10-20 ns. This is good for the SHG process, which increases in efficiency quadratically with peak power (energy/pulsewidth). This pulsewidth is, however, somewhat shorter than is required by the upper state lifetime of  $\text{Ti:Al}_2\text{O}_3$  and by the gain-switching dynamics. Consequently, the short pump-pulse leads to pump-induced damage of the  $\text{Ti:Al}_2\text{O}_3$  crystal at unnecessarily low energy-per-pulse levels. Laser-induced, peak-power damage has been shown to be roughly proportional to the inverse square root of the laser pulsewidth [3]. Therefore, increasing the pump pulsewidth decreases the risk of pump-induced damage to  $\text{Ti:Al}_2\text{O}_3$  crystals. This allows reliable operation further above threshold in oscillators, which ultimately means higher overall laser efficiency and greater system reliability. However, the pulsewidth must be kept short enough to ensure single-pulse output from the gain-switched oscillator. If the pump pulse is too long, the  $\text{Ti:Al}_2\text{O}_3$  oscillator will produce an output pulse before the pump pulse ends. This results in multiple-pulse output from the  $\text{Ti:Al}_2\text{O}_3$  oscillator, which is unacceptable in a lidar application. (A Q-switch could, in principle, be added to the  $\text{Ti:Al}_2\text{O}_3$  resonator to effect single-pulse operation, but this is a cumbersome and undesirable solution). The work performed on the Phase I project identified the optimum pump pulsewidth to be nominally 100 ns. With this defined, optimally-designed pumps for pulsed  $\text{Ti:Al}_2\text{O}_3$  could be designed and evaluated on the Phase II project. We did, in fact, demonstrate >50 mJ in pulses with 100- to 200-ns (FWHM) durations.

SEO's involvement in this refinement of Ti:Al<sub>2</sub>O<sub>3</sub>-pump-laser technology is rooted in its past involvement with Ti:Al<sub>2</sub>O<sub>3</sub> technology. SEO has been developing Ti:Al<sub>2</sub>O<sub>3</sub> lasers since the inception of the Research Division in 1985. Through funding from NASA LaRC and internal funding SEO has significantly advanced Ti:Al<sub>2</sub>O<sub>3</sub> technology for both government and commercial applications. The LaRC lidar system development contract mentioned earlier [1] resulted in the first demonstration of Ti:Al<sub>2</sub>O<sub>3</sub> unstable resonators [2]; the highest (to date) single-pulse output from Ti:Al<sub>2</sub>O<sub>3</sub> (430 mJ) [4,5]; and the development of a lidar transmitter design concept [2].

SEO has taken this technology, initially developed for NASA, into the commercial marketplace using its own funds. The first commercial product was a cw, Ti:Al<sub>2</sub>O<sub>3</sub> laser marketed under the tradename, *TITAN-CW*. This laser has been well received in the scientific community and over 160 units are now in the field. The performance characteristics of the *TITAN-CW* laser remain unsurpassed in terms of tuning range and laser threshold.

SEO also offers a pulsed Ti:Al<sub>2</sub>O<sub>3</sub> product, the *TITAN-P*, which employs the unstable-resonator technology developed for the LaRC lidar application. The laser is a self-contained system: the Ti:Al<sub>2</sub>O<sub>3</sub> oscillator and its pump, a frequency-doubled, Nd:YAG laser, are integrated into a compact laser head. The laser produces near-diffraction-limited output and is wavelength-tunable via remote control of a prism/mirror tuning assembly.

The Ti:Al<sub>2</sub>O<sub>3</sub> pump laser technology development being carried out under this SBIR program is clearly germane to SEO's interests and demonstrated capabilities. Furthermore, in keeping with the SBIR program goals, SEO intends to continue to pursue the development of these technologies and ultimately produce commercial laser products and/or systems that employ this technology.

In the following four sections, as a reference for the reader, we provide a review of some of the information that in the Phase II proposal: a summary of Phase I results, the Phase II Technical Objectives, the Phase II Work Plan and the Phase II Statement of Work.

#### **4 Review of Phase I Technical Objectives and Results**

*The goal of this project, which was defined in the original Phase I proposal, was to develop two types of Ti:Al<sub>2</sub>O<sub>3</sub> pump lasers: 1) a cw (or quasi-cw) pump laser for use with a single-frequency, master oscillator, and 2) a pulsed pump laser for use with gain-switched oscillators and amplifiers. These are the pump lasers needed for the single-frequency, high-energy, Ti:Al<sub>2</sub>O<sub>3</sub> lidar transmitter technology that is being developed by NASA LaRC [1]. In a space-based lidar system, both of these pump lasers would, in turn, be optically-pumped by diode lasers to achieve the necessary efficiency and operational lifetime.*

In order to develop pump lasers optimized for this application, it was necessary first to define the pump requirements. For the cw pump laser the power and beam quality are important.

For the quasi-cw alternative the quasi-cw pulsewidth needed to reach steady-state in the  $\text{Ti:Al}_2\text{O}_3$  master oscillator is also important. For the pulsed pump laser the important parameters are pulsewidth, pulse energy and spatial beam quality.

On the Phase I project we were able to better define the cw pump laser requirements. We demonstrated in Phase I experiments that cw,  $\text{Ti:Al}_2\text{O}_3$  oscillators can be made with thresholds as low as 90 mW. This means that 1 W of cw pump power is enough to provide a reliable injection-seeding source for the lidar-system application. We also developed a paper design for a 1 W, diode-laser-pumped, frequency-doubled neodymium (Nd) laser.

In addition, on the Phase I project we experimentally evaluated two types of pulsed pump lasers: a stable-relaxation-oscillation-laser (SROL), and a conventionally Q-switched oscillator/amplifier system. Both lasers were operated at the 1-J level and some second harmonic generation experiments were carried out as well. In addition, we used a laser-rate-equation model to more accurately define the optimum pulsewidth for gain-switched  $\text{Ti:Al}_2\text{O}_3$  lasers. The laser-rate-equation analysis led us to revise our definition of an optimum pulsewidth. In the Phase I proposal we assumed that the ideal pulsewidth would be between 200 and 500 ns. *However, in the Phase-I modeling work we showed that pulsewidths of about 100 ns are best when single-pulse, gain-switched output from the  $\text{Ti:Al}_2\text{O}_3$  oscillator is needed.* This means that either the SROL, or some type of Q-switching approach can be used for the pulsed pump laser.

In summary, the Phase I project was very productive. The pump laser requirements were more accurately defined by experimental and theoretical analysis of the  $\text{Ti:Al}_2\text{O}_3$  lasers used in our lidar system design. With this accomplished, we were able to proceed with a meaningful Phase II program in which we succeeded in demonstrating significant advances for both pump laser requirements.

## 5 Phase II Technical Objectives

The following paragraphs (italicized) are excerpted directly from Section 3.1 of the Phase II proposal as a reference for the reader. We adhered to these objectives throughout the Phase II project and we succeeded in demonstrating working laboratory lasers for both the cw and the pulsed pump laser requirements. With some additional engineering work we believe that the research-level, laboratory hardware produced in this project can be made into practical and useful commercial hardware. Furthermore, with appropriate environmental hardening these lasers could become components of space-based laser systems.

*The overall technical objective of this SBIR project is to develop pump lasers for both cw and pulsed  $\text{Ti:Al}_2\text{O}_3$  oscillators. On the Phase I program we were able to better define the pump requirements of the  $\text{Ti:Al}_2\text{O}_3$  lasers that make up the lidar transmitter. In addition, we began the process of designing appropriate pump lasers. With these performance requirements defined, the Phase II program will continue the development of laser hardware with an emphasis on the*

*design and construction of diode-laser-pumped lasers. With diode-laser-pumping of the Nd-lasers, the  $\text{Ti:Al}_2\text{O}_3$  laser becomes an all-solid-state system. With this in mind, the Phase II objectives will be as follows:*

- 1. To complete the design work on the 1-W, diode-laser-pumped, cw, frequency-doubled, Nd-laser that was begun on Phase I.*
- 2. To construct and test a breadboard prototype of the 1-W, cw green laser, including integration with a cw, single-frequency,  $\text{Ti:Al}_2\text{O}_3$  oscillator.*
- 3. To design a diode-laser-pumped, Q-switched, Nd-laser that produces the desired 100-ns pulsewidth at a pulse energy that is amenable to amplification to the 2-J level.*
- 4. To construct and test a breadboard prototype of the diode-laser-pumped, 100-ns, Q-switched pump laser.*

*To summarize, the experimental goal of Phase II is to build two working prototypes: 1) an all-solid-state,  $\text{Ti:Al}_2\text{O}_3$  master oscillator for a lidar transmitter and 2) a diode-laser-pumped, pulsed laser that would be the oscillator portion of a high-energy, pulsed pump for the slave oscillator in a lidar transmitter.*

All four of these objectives were met during the Phase II contract. Furthermore, SEO has already obtained funding to continue work in both of the technology areas that were developed on Phase II. The cw laser work will be continued in a Phase III level project that is jointly funded by SEO and another non-government sponsor. The ACQS work will continue under a U.S. Air Force-funded project where the ACQS will be further refined and applied to a different solid state laser system, Ho:YLF operating at 2 microns.

## **6 Phase II Work Plan**

In the preceding section the four specific technical objectives defined in the Phase II proposal were listed. In this section we list the tasks that were defined in the Phase II proposal as a means of meeting those objectives and describe the changes that we made to the work plan in the actual execution of the Phase II contract effort. The task headings are listed exactly as they appeared in the Phase II proposal, with comments regarding the actual work carried out and any changes made in the course of the project. This section will provide the reader with a succinct review of the work that was done on the Phase II contract in a manner that also shows how the research effort evolved and led to some significant changes in the experimental plans. Note the tasks are divided into four groups corresponding to the four objectives listed previously.

**Task 1a: *Design and construction of a gain module for use in a modified Nd:YAG ring laser***

We carried out a design review of the "baseline approach" for the diode-laser-pumped, cw green laser that was defined in our Phase II proposal, namely a transversely pumped, Nd:YAG laser with intracavity SHG. As a result of this review we became convinced that a longitudinally pumped approach would be most likely to provide the compact and efficient performance that we were seeking. This was primarily due to advances in cw, diode-laser technology and, in particular, some new results reported for microlens arrays used in conjunction with the relatively new, 1-cm, "diode bars" [6].

An additional conclusion of the design review was that we would be likely to benefit from the inherent thermo-optic properties of Nd:YLF as the gain medium. The uniaxial Nd:YLF crystal, when properly oriented, provides an inherent immunity to the radially symmetric, thermally-induced birefringence that leads to depolarization in isotropic crystal hosts such as Nd:YAG. The 1047-nm ( $\pi$ -polarized) laser transition in Nd:YLF has a stimulated emission cross section ( $\sigma$ ) that is on the order of that for the 1064-nm, Nd:YAG transition and has nominally a factor of two greater upper state lifetime ( $\tau$ ). Hence, its cw figure of merit ( $\sigma \cdot \tau$ ) is commensurate with that for Nd:YAG and it offers superior thermo-optic properties. The ability of Nd:YLF to maintain a highly linear polarization state leads to a significant overall advantage in this application since the intracavity SHG process requires a "pure" polarization state.

**Task 1b: *Gain-module design-verification experiments***

Since the design discussed above led to a significant change in the "baseline approach", the work planned in this task area was no longer relevant. Therefore, instead of doing gain measurements on transversely pumped gain modules, we developed a design for the Nd:YLF gain module that would integrate with the diode-laser bar/microlens array optics assembly, while still providing adequate cooling and a stress-free mechanical mount for the Nd:YLF crystal.

**Task 1c: *Experimental evaluation of SHG with type I KNbO<sub>3</sub>***

A further result of the cw-laser design review was to eliminate KNbO<sub>3</sub> as a candidate SHG crystal. There was already adequate data indicating that the intrinsic absorption of the material at both the fundamental and the second harmonic wavelengths, combined with its high sensitivity to temperature, would preclude efficient operation in a practical configuration.

The primary SHG crystals chosen in the course of the Phase II analysis were potassium titanyl phosphate (KTP) and lithium triborate (LBO). For 1047-nm SHG, in the Type II configuration, KTP has high nonlinearity, broad angular acceptance and a wide temperature bandwidth. It is, however, biaxial, which leads to an inherent difficulty in maintaining linear polarization when used as an intracavity element. This was dealt with by temperature tuning the crystal to maintain full-wave phase retardation at the fundamental wavelength (see Section 8.4.2 for details). LBO provides the most favorable conditions for 1047-nm SHG in the Type I NCPM configuration. In

order to achieve NCPM at 1047 nm the crystal must be heated to 172° C. This provides a challenge in terms of thermo-mechanical design, but is a tractable issue (see Section 8.4.1 for details).

**Task 1d: *Final design of a breadboard, I-W, diode-laser-pumped, frequency-doubled, Nd laser***

The overall laser design was actually completed in several steps with experimental evaluation of the critical subassemblies being carried out before proceeding with the next major laser design step. The design evolution began with a ray-tracing analysis of the diode, collimating and focusing optics and the Nd:YLF gain medium. The ray-tracing model provided a practical means of evolving a microlens-array design that was manufacturable and provided the desired gain distribution in the Nd:YLF laser crystal. The diode laser, the collimating and focusing optics, and the Nd:YLF gain module designs were finalized on the basis of the ray-tracing analysis. Components were purchased and this subassembly was thoroughly evaluated before proceeding with specific laser resonator designs.

Once the gain module was constructed and fully characterized, we began to study laser resonators experimentally. This allowed us to begin to appreciate and qualitatively analyze the thermo-optic properties of the short Nd:YLF crystals under the high thermal loading conditions created by cw pumping. We then carried out a sequence of laser tests and direct thermal lensing measurements to aid us in the design of thermally compensated oscillators. The experimental details of the empirically based design process are presented in Section 8.3.

**Task 2a: *Construction and testing of the breadboard cw green laser***

This task was carried out as planned once the various intermediate design steps described above were completed. The details are presented in Sections 8.3 and 8.4.

**Task 2b: *Evaluation of the breadboard green laser in quasi-cw operation***

We chose not to carry out the quasi-cw operation work given the limited resources and the evidence that the cw laser would most likely be preferred in a lidar system for a number of systems-level reasons.

**Task 2c: *Evaluation of the breadboard green laser and a cw, Ti:Al<sub>2</sub>O<sub>3</sub> laser in cw and quasi-cw operation***

After obtaining the 900-mW power level, we used the Nd:YLF green laser to pump a cw, ring, Ti:Al<sub>2</sub>O<sub>3</sub> laser to demonstrate the complete all-solid-state, master oscillator in a truly single-frequency and broadly tunable configuration. Experimental details are given in Section 8.5.



**Task 3a: *Assessment of current diode-laser-pumping technology.***

As planned, we carried out a design review similar to that done for the cw, green laser. We selected Nd:YAG as the gain medium for the pulsed laser development work, because it has a high stimulated emission cross section and isotropic absorption, which allows simple, efficient operation in the rod geometries that we preferred for this work. Rod geometries provide simple, cylindrically symmetric gain distributions and allow for simple cooling arrangements.

**Task 3b: *Optimization of the 100-ns, oscillator optical design.***

Early in the project we began developing an electrical circuit (using a microwave triode) that was to be used to actively control an electro-optic, intracavity element for the purpose of controlling the pulse-evolution dynamics. The circuit design evolved over the course of the work and resulted in the circuit that is described in Section 9.4.

Separately we developed two optical head designs for the diode-laser-pumped, pulsed laser experiments: a "radial" pump head and a "linear" pump head. Both designs used a side-pumped laser rod geometry.

**Task 4a: *Procurement of breadboard components.***

Optical and mechanical hardware was fabricated for the radial and linear pump head designs.

**Task 4b: *Assembly and testing of diode-laser gain modules.***

The radial pump head was constructed and evaluated first. The linear pump head was constructed and evaluated subsequently. The head designs and the experimental work with them is described in detail in Sections 9.2 and 9.3.

**Task 4c: *Assembly and testing of Q-switched oscillator.***

The ACQS work was carried out using a flashlamp-pumped, Nd:YAG test bed. This was to allow maximum flexibility in the ACQS effort and to allow the diode-laser-pumped work to go on in parallel with and independent of the ACQS work. The intent was to integrate the ACQS hardware into the diode-laser-pumped oscillator at the end of the ACQS effort. We were not able to carry out this integration step within the time frame of the Phase II program. This is the next logical step in the development effort, which could be carried out in a Phase III effort at SEO or by NASA researchers.

## **7 Phase II Statement of Work**

The Work Plan in the original Phase II proposal was summarized in the following formal Statement of Work. This later became the working Statement of Work for the Phase II contract.

1. Given the rapidly evolving state of diode-laser-pumping technology, at the beginning of the Phase II contract period we will carefully assess any recent developments and establish an up-to-date basis for the Phase II design tasks.

2. We will review our cw gain-module design and define a final design for the gain module and the cw, frequency-doubled Nd laser.
3. We will procure all the materials necessary and construct and experimentally evaluate a breadboard prototype of the diode-laser-pumped, cw, frequency-doubled Nd laser.
4. We will use the breadboard laser to pump a single-frequency, cw Ti:Al<sub>2</sub>O<sub>3</sub> oscillator and evaluate the performance of the Ti:Al<sub>2</sub>O<sub>3</sub> with this pump relative to the typical Ar-laser-pumped characteristics.
5. We will operate the breadboard laser in quasi-cw mode and evaluate the characteristics of the pump and the Ti:Al<sub>2</sub>O<sub>3</sub> laser output. This will include temporal and spatial characteristics of the pump and temporal and spectral characteristics of the Ti:Al<sub>2</sub>O<sub>3</sub> oscillator.
6. We will design a diode-laser-pumped, Q-switched, Nd laser that produces 100-ns (FWHM) pulses.
7. We will procure the necessary materials and construct and evaluate a breadboard prototype of the 100-ns, Q-switched, Nd laser.
8. We will deliver to NASA LaRC the two breadboard prototype lasers constructed and tested on the Phase II contract.

All items are now completed except for item 5. As stated earlier, we chose to forego quasi-cw experiments in light of our conclusion that cw pumping would be more desirable in actual lidar systems. This allowed more of our resources to be directed toward the goal of the best possible cw laser performance within the Phase II contract limitations.

As per item 8, the two breadboard prototype lasers were shipped to NASA LaRC on 10 November 1993. Related non-expendable materials purchased on the contract were included in the shipment as well.

## **8 CW Laser Development**

The details of the development of the master-oscillator pump laser are presented in this section. The 900-mW, cw, green output power that was obtained in this effort was proven, experimentally, to be adequate to obtain injection-seeding-level output from a single-frequency, Ti:Al<sub>2</sub>O<sub>3</sub> laser over a tuning range of at least 200 nm. This is a significant advance in the development of practical high-energy, Ti:Al<sub>2</sub>O<sub>3</sub> lidar systems for space-based applications.

### **8.1 Preliminary Design Considerations**

This master-oscillator is a critical subsystem of the lidar transmitter design under development at NASA LaRC [1]. The master oscillator, via the well-known injection-seeding mechanism, constrains the high-energy, slave oscillator to operation on a single-longitudinal-mode, hence allowing the final output of the Ti:Al<sub>2</sub>O<sub>3</sub> lidar transmitter to be both

near-diffraction-limited in spatial beam quality and near-transform-limited in terms of spectral linewidth. This optimum performance level is required for long-range, DIAL, remote-sensing applications. Furthermore, if the lidar system is to be space-based, all of the lasers used in the system must be solid state lasers in order to meet the requirements of reliability, compactness, efficiency and operational lifetime.

The earlier laboratory-development work on the  $\text{Ti:Al}_2\text{O}_3$  master oscillator that was carried out at SEO relied on Ar-ion lasers as the optical pump source. While the Ar-ion laser is extensively used in laboratory environments throughout the world, it is an extremely inefficient laser system. In practice this means these lasers are large in size, require high capacity cooling (for the laser head and the power supplies) and consume a great deal of electrical power. These problems absolutely preclude their use in space-based lidar systems. Hence, one goal of this project was to develop a very compact, efficient "replacement" for the Ar-ion laser. The new laser would have to produce a near-diffraction-limited, cw output beam in the blue-green region of the spectrum where the  $\text{Ti:Al}_2\text{O}_3$  absorption is strong.

It was clear at the outset of the Phase I project that the solution would be a diode-laser-pumped, cw, Nd-laser operating at a fundamental wavelength of 1 micron and subsequently frequency doubled to produce a green pump beam. Diode-laser-pumping of Nd-lasers was, in fact, already a rapidly advancing technology area at that time. The challenge for this work was to identify a specific laser design that would meet the specific requirement of our  $\text{Ti:Al}_2\text{O}_3$  master oscillator and carry out experiments to demonstrate "reduction to practice". This involved selection of a crystal host for the Nd ion; selection of a pumping geometry (transverse vs. longitudinal); selection of a mounting/cooling geometry for the gain medium; selection of a second harmonic generation (SHG) crystal; selection of a resonator design to accommodate all these components; and, the design and testing of the optical and opto-mechanical hardware necessary for the final all-solid-state, master-oscillator demonstration at the end of the program.

## **8.2 CW Gain Module Design and Construction**

The gain module of the cw laser consists of a 10-W, cw, GaAlAs diode-laser array, collimating and focusing optics (including a microlens array), and an end-pumped, Nd:YLF rod. The characteristics of the diode laser, the optical components, and the Nd:YLF gain element are discussed in the sections below.

### **8.2.1 Diode Laser Characteristics**

We selected a 10-W, twelve-element, GaAlAs linear diode laser array for use in this project. We obtained and evaluated several of these diode laser "bars", from two different vendors, during the course of the program. All of the cw diode lasers that we used shared the following characteristics: 10-W nominal output; 797-nm nominal wavelength; twelve-element linear array structure; 200- $\mu\text{m}$  individual element width; 1- $\mu\text{m}$  individual element height; 800- $\mu\text{m}$  center-to-center element spacing; overall array length of approximately 1 cm; and output polarization par-

allel to the plane of the array. The collimating and focusing optics described in the next section were designed specifically for this array structure. An EMS-7.5-130-1-D power supply from Electronic Measurements, Inc. (Neptune, NJ) was used as the diode laser driver. The diode laser was mounted on a copper heatsink cooled by 0.8 gallons per minute of closed-loop water flow from a chiller with variable temperature control.

The first 10-W cw diode laser we obtained was model number SDL-3490-S from Spectra Diode Labs (SDL, San Jose, California). We checked the output power and wavelength of this device and then installed it in the gain module. After approximately 100 hours of mostly low- and medium-power use, the device failed during full-power operation. This proved to be a major setback to the program schedule, due to the lead time required to obtain a replacement. In order to minimize the possibility of further delays, we ordered two 10-W devices (from different vendors) and evaluated them much more thoroughly when they arrived. The first device was a replacement SDL-3490-S from SDL; the second was model number AOI-A010-798-CS from Opto Power Corporation (OPC, City of Industry, California).

The following tests and measurements were performed on the SDL and OPC devices: I/O curves to the full, 10-W, power level; relative power outputs of the twelve individual emitters; absolute wavelength and linewidth for each of the twelve emitters; spatial uniformity of the emitters; and temperature tuning of the average output wavelength.

Both devices produced 10 W of output at the specified operating current. However, the output power per junction was much more uniform in the OPC device. For the OPC device, the standard deviation of a single emitter's output power was 5% of the average, while for the SDL device the standard deviation was 22% of the average. In the SDL device the variation was so great that some emitters produced more than twice as much power as others.

The wavelength uniformity over the twelve emitters was also better in the OPC device. The OPC device had a standard wavelength deviation of 0.2 nm, while the SDL device had a standard wavelength deviation of 0.8 nm. However, in terms of the linewidth of a single emitter, the SDL device was slightly better: the average FWHM linewidth for a single emitter was 1.3 nm for the SDL device, compared to 1.8 nm for the OPC device.

The spatial uniformity of the emitters was measured in terms of tilt (angular deviation of the emitters from the horizontal) and liftoff (displacement of the edge emitters upwards from the horizontal plane). Both devices showed the characteristic "smile", that is, tilt and liftoff of the edge emitters. In the OPC device the smile was more pronounced, and somewhat lopsided, with a liftoff of about 20  $\mu\text{m}$  at one end only. Tilt of up to 30 arc minutes was observed at the edge emitters. In the SDL device, the liftoff was very slight, less than about 5  $\mu\text{m}$  at each end, and the tilt was less than 10 arc minutes.

For each device, a representative average-wavelength emitter was chosen for temperature-tuning experiments. The manufacturer-specified output wavelengths were 798 nm at 27.5°C for the OPC device, and 796 nm at 25°C for the SDL device. We measured the average output wavelength of each device as a function of the power level and the cooling water temperature. For example, at full power and 24°C water temperature, the average wavelength of the OPC device was 800.2 nm, while the average wavelength of the SDL device was 795.5 nm. Our goal was to maintain the wavelength at 797 nm for pumping Nd:YLF; in order to do so, the cooling water temperature had to be set correctly for each device at each output power level. For the OPC device, at threshold a water temperature of 26°C was required for operation at 797 nm, while at full power a water temperature of 14°C was required. For the SDL device, at threshold the required water temperature for operation at 797 nm was well over 30°C (we did not attempt to operate the device at such a high temperature), while at full power a water temperature of 29°C was required.

Table 8-1 summarizes the data taken on the OPC and SDL 10-W cw diode lasers used in this program. For comparison, data are also shown for three other (different-wavelength) 10-W cw diode lasers being used in other SEO programs. As the table indicates, our particular SDL device was considerably substandard in terms of power uniformity and wavelength uniformity. Primarily for this reason, we chose to use the OPC device as our pump source and keep the SDL device as a spare. Complete data are unfortunately not available on the original SDL device that failed during operation.

**Table 8-1.** Comparison of 10-W cw GaAlAs Diode Laser Arrays

	Devices used in this program		Devices used in other programs		
Manufacturer	OPC	SDL	OPC	SDL	SDL
Serial Number	00100071	GD969	00100038	GD429	GF178
Manufacturer's Wave- length Specification	798 nm @ 27.5°C	796 nm @ 25°C	795 nm @ 27.5°C	810 nm @ 25°C	806 nm @ 25°C
Desired Operating Wavelength	797 nm	797 nm	794 nm	808 nm	808 nm
Measured Average Wavelength @ Full Power & 24°C	800.2 nm	795.5 nm	793.4 nm	808.7 nm	806.3 nm
Standard Deviation of Emitter Wavelength	0.2 nm	0.8 nm	0.2 nm	0.4 nm	1.0 nm
Average Emitter Linewidth (FWHM)	1.8 nm	1.3 nm	1.7 nm	1.6 nm	1.3 nm
Standard Deviation of Emitter Output Power (% of Average)	5%	22%	7%	6%	5%
Maximum Emitter Tilt Observed	30 arc min	10 arc min	20 arc min	20 arc min	*
Maximum Emitter Liftoff Observed	20 $\mu$ m	5 $\mu$ m	10 $\mu$ m	8 $\mu$ m	*
Temperature Required to Maintain Desired Operating Wavelength...					
... at threshold:	26°C	*	*	*	*
... at 5 W power:	21°C	*	*	*	*
... at 10 W power:	14°C	29°C	26°C	21°C	*

\* Data not available

### 8.2.2 Collimating and Focusing Optics: Design and Performance

The use of a linear diode-laser array to end-pump a laser crystal requires appropriate collimating and focusing optics. In order to achieve good mode-matching between the resonator mode and the pump volume, it is usually desirable to have a circularly symmetric pump beam; and in order to achieve a high inversion density in the laser crystal, it is desirable to keep the pump-beam size small in the absorption region. However, the output characteristics of a linear diode laser array do not lend themselves easily to the creation of a small, symmetric pump beam. The overall emission region of the array is highly asymmetric, approximately  $1\text{ cm} \times 1\text{ }\mu\text{m}$  in our case. It consists of twelve individual asymmetric emitters, each  $200\text{ }\mu\text{m} \times 1\text{ }\mu\text{m}$  in size. The output beam is asymmetric in divergence as well: in the plane perpendicular to the array the output is near diffraction-limited with a typical beam divergence of  $30\text{--}45^\circ$ , while in the plane parallel to the array the output is many times diffraction-limited with a typical beam divergence of  $10^\circ$ . The collimating and focusing optics must be designed to image this highly asymmetric, astigmatic output into a pump beam as small and symmetric as possible.

Various combinations of collimating and focusing optics may be used for end pumping with linear arrays of this type. The optical layout typically includes a fast rod/cylinder lens to collect the highly divergent output in the plane perpendicular to the array, possibly a cylinder lens or other optical element to collimate the light in the plane parallel to the array, and an imaging lens to create a focus at the location of the laser crystal. Elliptical focused pump spots of  $1.1\text{ mm} \times 150\text{ }\mu\text{m}$  and  $1.12\text{ mm} \times 250\text{ }\mu\text{m}$  have been reported using a rod lens, cylinder lens, and aspheric imaging lens combination [7,8]. A reasonably symmetric pump spot of  $2.2\text{ mm}$  diameter has been reported using simply a rod lens and an imaging lens; in the same system, the addition of a lens array made of  $\text{SiO}_2$  fibers after the rod lens reduced the spot diameter to approximately  $0.8\text{ mm}$  [6].

Based on the available literature, we set our goal to be a reasonably symmetric pump spot approximately  $1\text{ mm}$  in diameter. We chose to use a cylinder lens, microlens array, and aspheric imaging lens combination in order to achieve that goal. The use of a microlens array was the most novel element in our approach to the problem. The array consists of twelve individual cylinder lenses, each matched to an individual emitter on the diode laser, on a single substrate. The microlens array is conceptually similar to the  $\text{SiO}_2$  fiber lens array mentioned above [6], but the construction of the array is quite different. The components of the optical system, including the microlens array, are described in more detail in the following paragraphs. A layout of the optical system is shown in Figure 8-1.

We made the cylinder lens by having a  $2\text{-mm}$ -diameter gradient index rod lens ground in half (a "D-shape" in cross section) and using it in the transverse orientation. The cylinder lens, placed approximately  $1\text{ mm}$  from the diode laser, collects and almost collimates the highly diver-

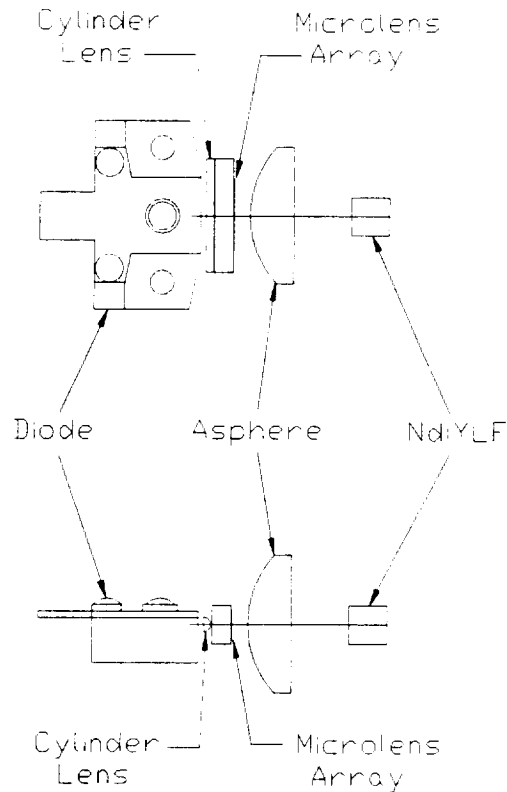


**Figure 8-1.** Layout of the 10-W cw diode laser array, focusing optics, and Nd:YLF crystal in the diode-pumped cw Nd:YLF laser.

gent output in the plane perpendicular to the diode array. (The beam is allowed to remain slightly diverging in this plane, for reasons to be explained shortly.) The cylinder lens is AR coated for 797 nm, the diode laser operating wavelength.

The microlens array consists of twelve individual cylinder lenses, each matched to an emitter on the diode laser. The array of cylinder lenses is formed by an epoxy layer deposited on the surface of a 2-mm-thick glass substrate. The glass substrate is AR coated on the opposite side. The microlens array was fabricated by Adaptive Optics Associates (AOA, Cambridge, MA) according to an SEO design. In the optical system, the microlens array is placed immediately after the cylinder lens. The microlens array collimates the output of the individual diode laser emitters in the plane parallel to the diode array.

It should be noted that there are other methods of fabricating microlens arrays which may prove to be more practical. While we were satisfied with the laboratory performance of these epoxy-layer microlens arrays made by AOA, we have reservations about the long-term durability of the epoxy layer. In addition, the microlens arrays we received from AOA were of variable quality, with some arrays showing bubbles and other imperfections in the epoxy. SEO is cur-



rently investigating alternative fabrication techniques, including a sol-gel technique for making fused silica microlens arrays. Typically the major expense in the production of microlens arrays lies in the fabrication of a "master" lens array mold, from which multiple microlens arrays can then be made at a relatively low cost.

The imaging lens is an aspheric, 12-mm focal length, AR coated lens placed approximately 10 mm after the microlens array. This asphere creates a focused pump spot at the location of the laser crystal. The drastically different beam characteristics in the planes perpendicular and parallel to the array are accounted for in the optical system design, to create a pump spot as symmetric as possible. In the plane parallel to the array (in which the beam is many times diffraction limited), the beam is focused by the asphere to the tightest possible waist at the location of the laser crystal. The beam then diverges rapidly. In the plane perpendicular to the array (in which the beam is near diffraction limited), the beam would be much too small relative to the other plane if it were similarly focused to the tightest possible waist. Therefore the beam in this plane is allowed to remain slightly diverging as it enters the asphere, so that it is only slightly converging (not at a waist) at the location of the laser crystal. In this manner a focused pump spot is formed which is roughly symmetric over a length of several millimeters.

The optical system was designed and modelled at SEO using a raytracing program. The highlights of the raytracing analysis are presented in Figures 8-2, 8-3, and 8-4. Figure 8-2 shows a top view of the optical path from the microlens array, through the aspheric lens, to the Nd:YLF crystal. Only rays from the center and edge emitters of the diode laser are shown. Figure 8-3 shows a side view of the optical path from the diode, through all of the collimating and focusing optics, to the Nd:YLF crystal. Figure 8-4 is a closeup top view of the focused pump beam in the Nd:YLF crystal, with rays from all twelve emitters shown. The raytrace model predicted a symmetric spot of 1.2 mm diameter at the focus inside the Nd:YLF rod, with the beam rapidly diverging in the horizontal plane (parallel to the array) and very slightly converging in the vertical plane (perpendicular to the array). The pump spot obtained experimentally was in excellent agreement with the model: 1.4 mm  $1/e^2$  diameter at the focus (1.0 mm top-hat equivalent diameter), with the beam rapidly diverging in the horizontal plane and very slightly converging in the vertical plane. The measured pump beam size in each plane in the region of the focus is shown in Figure 8-5, with the dimensions of a 4-mm diameter by 5-mm long Nd:YLF rod superimposed. A pump beam profile at the location of the focus appears in Figure 8-6. Additional profiles of the beam throughout the region near the focus may be found in Appendix A (Section 13), Figures A-1 through A-9.

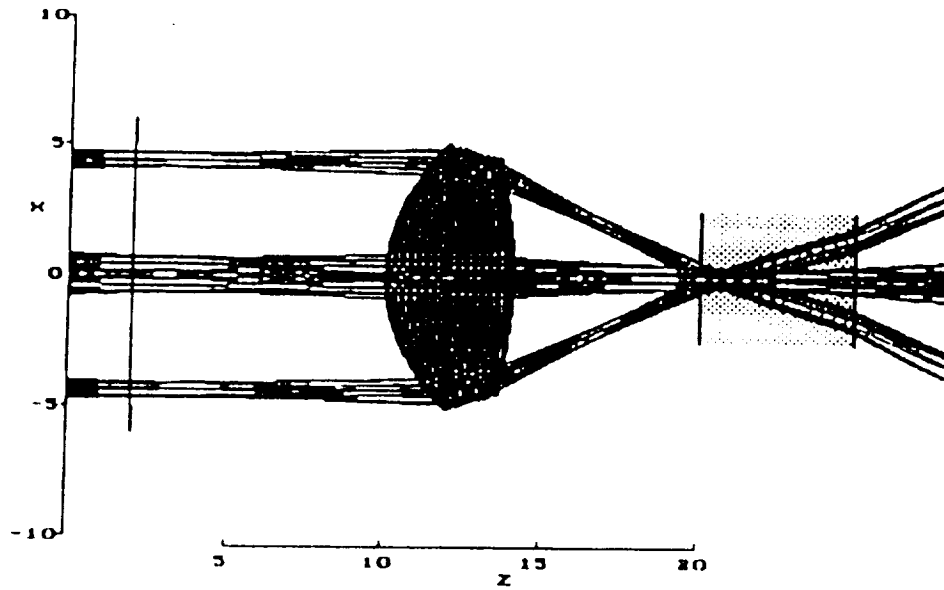


Figure 8-2. Raytrace model of the focused 10-W cw diode laser pump beam, top view, showing edge and center emitters only.

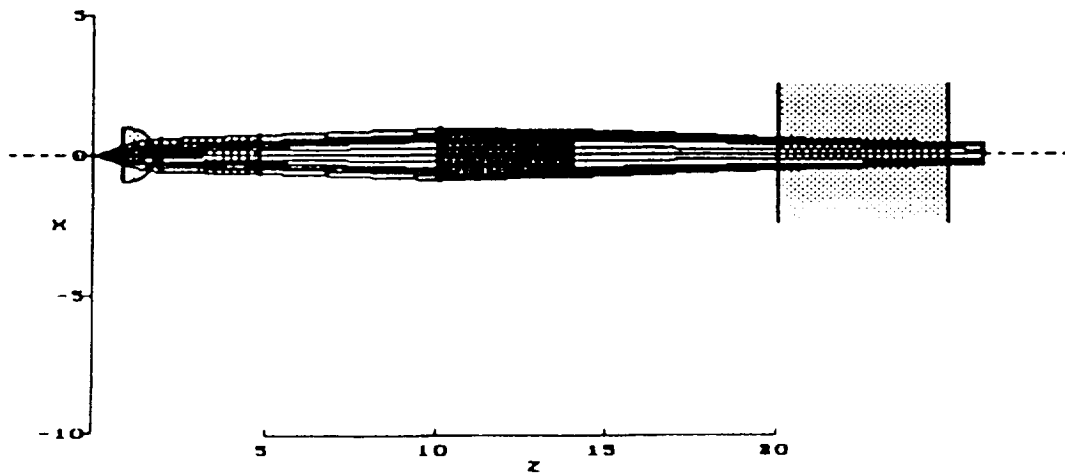
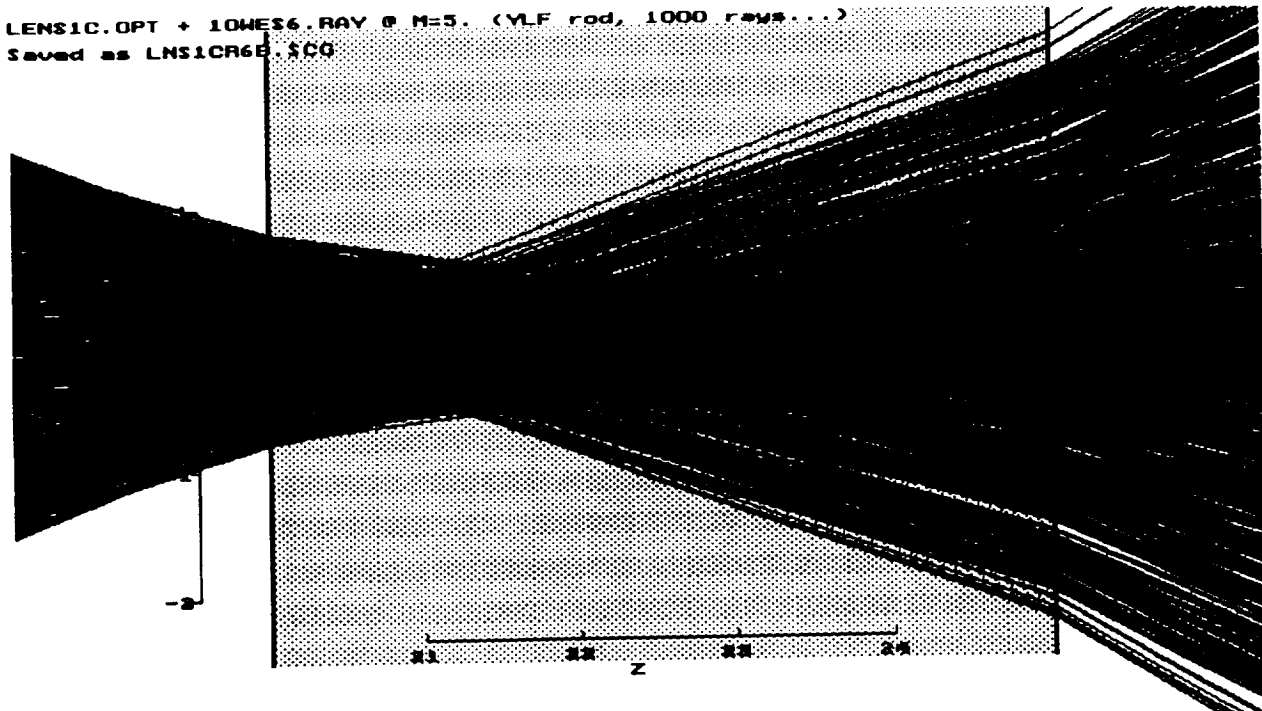


Figure 8-3. Raytrace model of the focused 10-W cw diode laser pump beam, side view.

LENS1C.OPT + 10WES6.RAY @ M=5. (YLF rod, 1000 rays...)  
 Saved as LNS1CR6B.\$CO



starts= 1000 finishes= 1000: 100.0x  
 LAYOUT: Annotate BlankMenu Zaxis Hdim Udim Pos Mag Rand ElAz Quads CAD ESC

Figure 8-4. Raytrace model of the focused 10-W cw diode laser pump beam in the Nd:YLF crystal, top view.

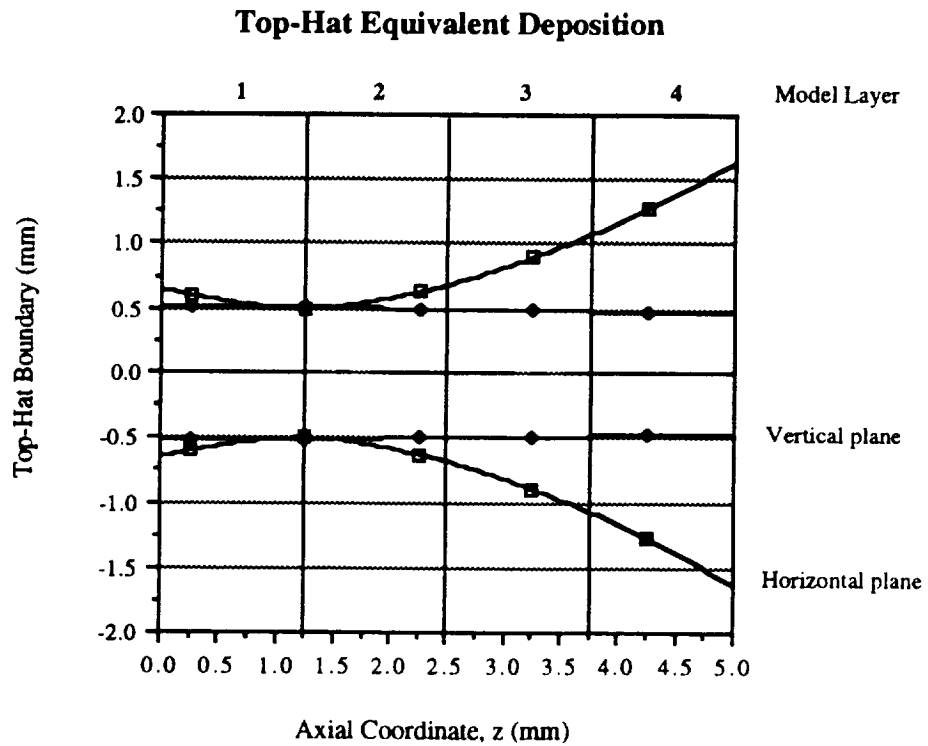
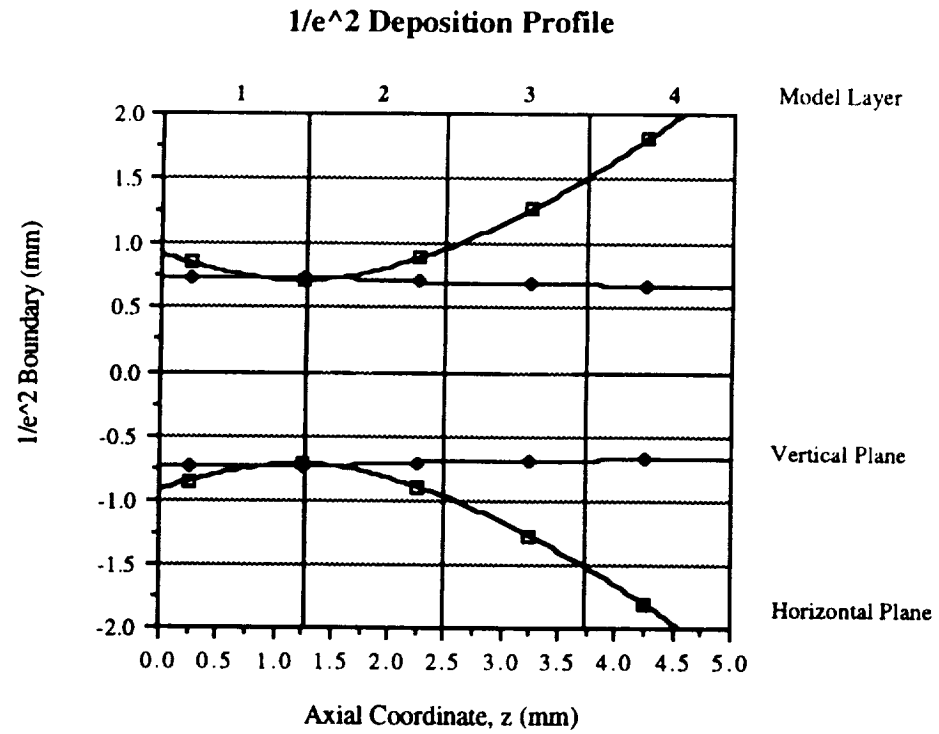
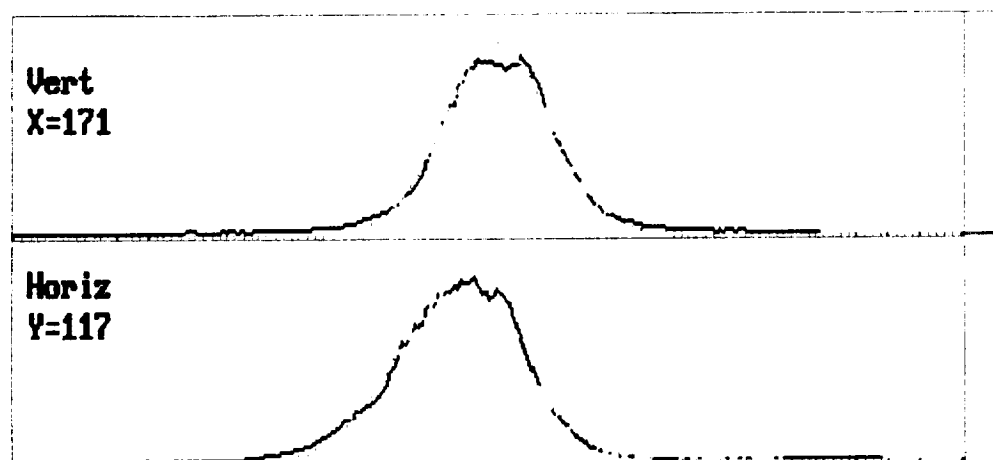


Figure 8-5. Measured beam size of the focused 10-W cw diode laser pump beam in the region of the focus, with dimensions of a 4x5 mm Nd:YLF rod superimposed.

(Gaussian Fit Data)		
	Vert	Horiz
Correlation Coeff.	= 0.959	0.946
Peak Position	= 121	172
Beam Dia. @ $1/e^2$ [mm]	= 1.438	1.481
Percent of Peak	= 91.732	81.382

(Cursor Location)	
<b>CENTROID</b>	
(X,Y) = (171,117)	
Profile Location	
X (Vert)	= 171
Y (Horiz)	= 117

Active Cursor: Contour



LEFT MOUSE BUTTON draws profile.

Press <ESC> to abort printing.

Figure 8-6. Profile of the 10-W cw diode laser pump beam at the location of the focus.

As mentioned above, all of the optical elements were AR coated for 797 nm. The microlens array and the aspheric lens were measured to have excellent power transmission, approximately 98% each. The transmission of the cylinder lens was strongly dependent on its distance from the diode laser: the closer it was placed, the better its measured transmission, since it would collect more of the rapidly diverging diode output. However, its placement was fixed at approximately 1 mm from the diode laser by optical system constraints. At that distance its transmission was approximately 84%. Therefore the overall transmission of the optical system (the percentage of raw diode output power delivered to the Nd:YLF crystal) was approximately 80%. In the laser performance data presented later in this section, the "pump power level" refers to the pump power actually delivered to the Nd:YLF crystal, not the raw output power of the diode laser array.

The diode laser and its collimating and focusing optics were mounted in a custom-designed fixture which allowed many degrees of freedom in positioning the various components. The fixture consisted of two stacked translators for mounting the diode laser and its heatsink, and two adjustable nested plates to hold the optical components. The inner plate held the cylinder lens and microlens array; the outer plate held the aspheric lens. The positioning degrees of freedom available included longitudinal translation of the entire pump assembly, transverse translation of the diode laser with respect to the microlens array, tilt and height adjustment of the optical components, longitudinal positioning and tilt of the cylinder lens/microlens array, and longitudinal positioning and tilt of the aspheric lens. This custom-designed fixture was useful in the lab for characterizing the performance of the optical system over a wide range of parameters; now, with the ideal parameters established, future versions of the mounting fixture can be simpler and less versatile.

Of the multiple degrees of freedom available, three adjustments were found to be particularly important for the collimating and focusing optics. One was the transverse positioning of the diode laser with respect to the microlens array. The second was the longitudinal positioning of the cylinder lens with respect to the diode laser -- a highly sensitive adjustment which determined the vertical size of the pump beam at the laser crystal. The third was the longitudinal positioning of the entire pump assembly with respect to the Nd:YLF rod -- that is, the longitudinal positioning of the pump focus within the laser crystal. Optimum laser performance was typically obtained with the pump focus located 1.0-1.5 mm inside the pumped face of the Nd:YLF crystal. This last adjustment was found to be useful for actively fine-tuning the pump distribution during laser operation, particularly when varying the laser resonator parameters; all of the other adjustments for the collimating and focusing optics were basically set once and then left alone for the duration of the experiments.

In summary, the optical system that we designed and built was highly successful in focusing the asymmetric, astigmatic output from the linear diode laser array into a small, symmetric pump beam. The microlens array, in particular, worked as anticipated in this application. We were able to couple approximately 80% of the output power from the diode laser array into a

symmetric pump spot 1.4 mm in  $1/e^2$  diameter, and 1.0 mm in top-hat equivalent diameter. The focused pump spot that we obtained experimentally was in excellent agreement with our raytrace model and very close to the goal that we set initially.

### 8.2.3 Gain Element Characteristics

The gain element in the cw laser is an end-pumped Nd:YLF rod. The Nd:YLF crystal is oriented with the c-axis horizontal, parallel to both the pump beam polarization and the laser polarization. Thus the pump polarization and the laser polarization are both in the  $\pi$  orientation, and the lasing wavelength is 1047 nm.

Four different Nd:YLF crystals were procured on this program: two short, highly doped crystals, and two longer, lighter doped crystals. A flat/flat version and a flat/Brewster-cut version of each type were obtained. The characteristics of the four crystals are summarized below:

**All crystals:** Nd:YLF; 4 mm diameter; "pumped" surface flat, and coated for high reflectivity at 1047 nm and high transmission at 797 nm.

**Crystal #1:** 1.0% Nd; 5 mm long; "unpumped" surface flat, and AR coated for 1047 nm.

**Crystal #2:** 1.0% Nd; 5 mm long on short side; "unpumped" surface Brewster-cut, and uncoated.

**Crystal #3:** 0.5% Nd; 10 mm long; "unpumped" surface flat, and AR coated for 1047 nm.

**Crystal #4:** 0.5% Nd; 10 mm long on short side; "unpumped" surface Brewster-cut, and uncoated.

The different doping levels were chosen to give us the option of absorbing the pump power over a shorter or longer region of the laser crystal. Initial pumping experiments quickly showed that it was desirable to absorb the pump power over as short a distance as possible, in the region near the pump focus where the pump beam was most symmetric. For this reason, the highly doped crystals (#1 and #2) were used in the laser experiments, while the lighter doped crystals (#3 and #4) were kept as spares.

The absorption of crystal #1 at 797 nm was measured directly using a cw Ti:Al<sub>2</sub>O<sub>3</sub> probe laser. The rod absorbed 99% of the incident power over its 5-mm length, indicating an absorption coefficient of  $\alpha = 9.2 \text{ cm}^{-1}$ . Accurate pump power absorption measurements using the actual diode pump beam are more difficult, since the pump beam diverges rapidly as it exits the crystal. Measurements carried out with the same crystal, diode-pumped at 797 nm, indicated that  $(93 \pm 2)\%$  of the incident power was absorbed over the 5-mm length. This is lower than the 99% absorption observed with Ti:Al<sub>2</sub>O<sub>3</sub> pumping, which is an expected result due to the greater spectral linewidth of the diode-laser pump beam.

Of the highly doped crystals, the flat/Brewster crystal (#2) produced the best results in the laser experiments. This was due to two factors: the lower loss at its Brewster surface, compared to the AR coated back surface of the flat/flat crystal; and better resonator mode-matching to the "effective" pump profile, as discussed in the following paragraph.

Although the pump beam is symmetric at the focus, it is rapidly diverging in the horizontal plane (refer to Figure 8-5). Outside the immediate region of the focus the pump beam is elliptical (elongated in the horizontal dimension). Most of the pump power is absorbed near the "pumped" face of the Nd:YLF, in the region near the focus, where the pump beam is reasonably symmetric. However, some absorption does take place in the regions where the pump beam is more elliptical. Consequently, over the 5-mm length of the Nd:YLF rod there is inevitably some ellipticity in the pump deposition pattern. From fluorescence profiles, such as the one shown in Figure 8-7, we estimated the "effective" pump profile over the length of the Nd:YLF rod to have an ellipticity of roughly 1.5 to 1.0. This ellipticity can be a problem when trying to match the pump profile to a circular resonator mode. However, in the case of a flat/Brewster crystal, the resonator mode itself is elliptical inside the laser crystal, by a factor equal to the crystal index. In our case the resonator mode inside the flat/Brewster Nd:YLF crystal had an ellipticity of 1.47 to 1.00, which proved to be an excellent match to the elliptical "effective" pump profile.

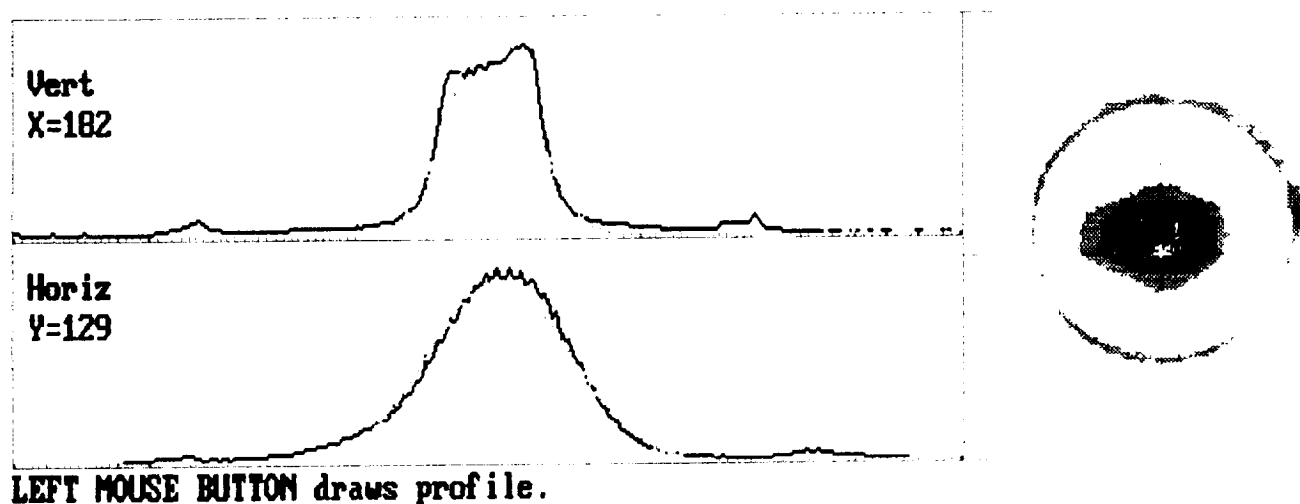
Each of the four Nd:YLF crystals was mounted in its own custom-designed copper heat-sink using a thermal RTV compound. The heatsinks were designed to provide radial cooling for the crystals along their entire lengths, with only their front and rear surfaces exposed. The heatsinks were constructed to allow water to flow in a path over and around the crystal, to further improve the cooling conditions. Water flow was provided by the same closed-loop water system used to cool the diode laser heatsink.

Proper cooling for the Nd:YLF crystal is necessary because of the great thermal stresses associated with the deposition of 10 W of pump power in a 1-mm-diameter region of the end-pumped rod. These thermal effects are the subject of a thermal modeling study currently being performed at SEO. The study, which is being conducted under separate funding, uses some of the data obtained on this program as a starting point. A few highlights of the initial results of the study are presented here. In the model, a 4-mm diameter by 5-mm long flat/flat Nd:YLF rod is end-pumped by a focused diode pump beam with the characteristics measured experimentally under this program. The radial edges of the rod are held at 20°C to simulate perfect cooling. The resulting calculated three-dimensional temperature distribution within the rod, at 5 W pump power, is shown in Figure 8-8. Profiles of the calculated temperature distribution across the front and rear faces of the rod appear in Figures 8-9 and 8-10, respectively. Notice that the center temperature of the rod at the front face is approximately 40°C. The temperature is expected to scale linearly with pump power, so the center temperature at the front face is expected to be approximately 60°C at 10 W pump power. This corresponds to a 20°C/mm temperature gradient across the front face of the rod. As the study progresses we hope to characterize the stresses associated with such a temperature distribution and their effects on laser performance.



(Gaussian fit Data)			Cursor location =	
	Vert	Horiz	PEAK	
Correlation Coeff.	= 0.879	0.945	(X,Y) = (182,129)	
Peak Position	= 120	182	Profile location	
Beam Dia. @ 1/e <sup>2</sup> [mm]	= 1.095	1.619	X (Vert) = 182	
Percent of Peak	= 103.877	86.787	Y (Horiz) = 129	

Active Cursor: Contour



Press <ESC> to abort printing.

Figure 8-7. Fluorescence profile from the Nd:YLF rod pumped by the focused 10-W cw diode laser.

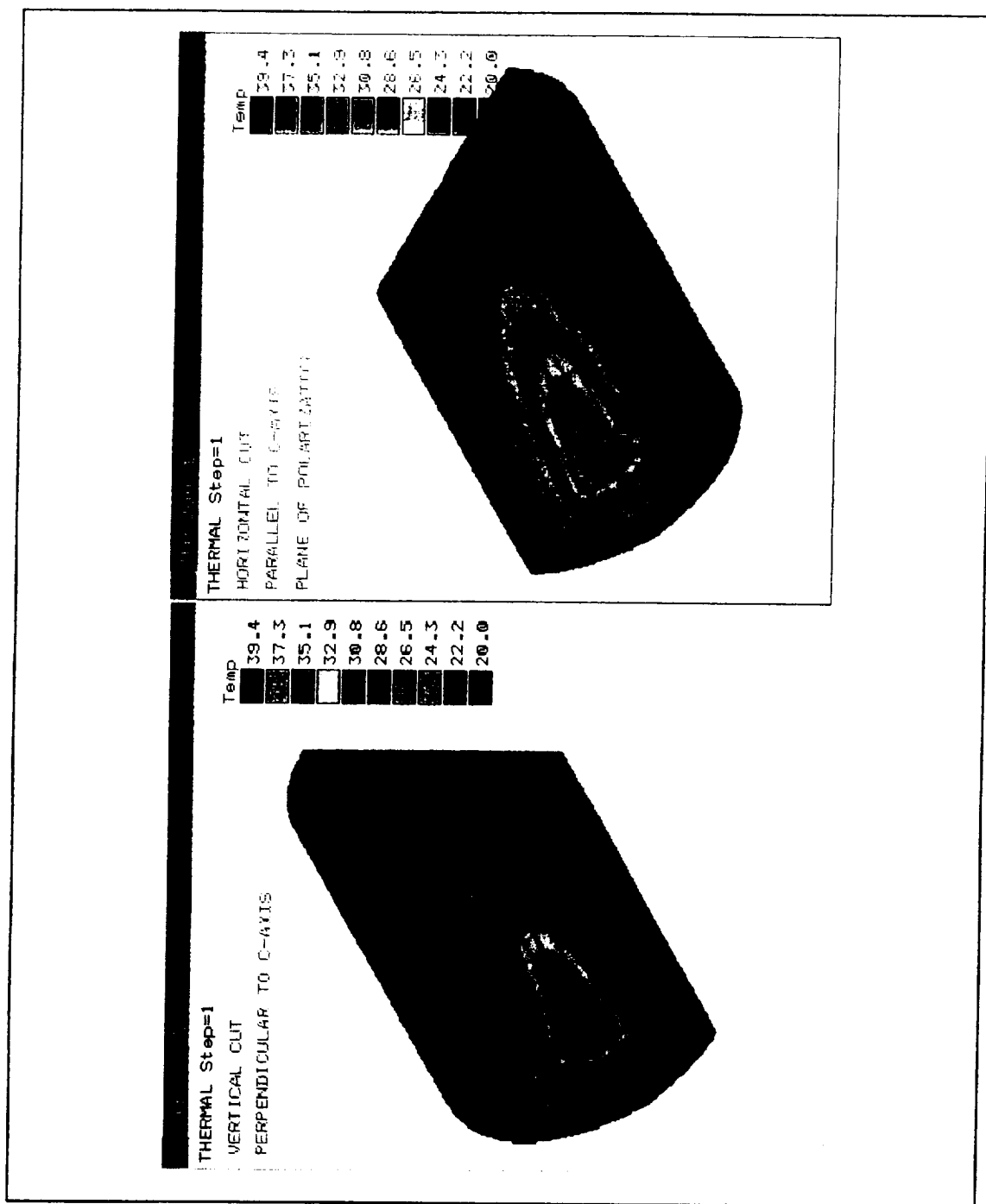


Figure 8-8. Calculated temperature distribution in the diode-pumped Nd:YLF rod.

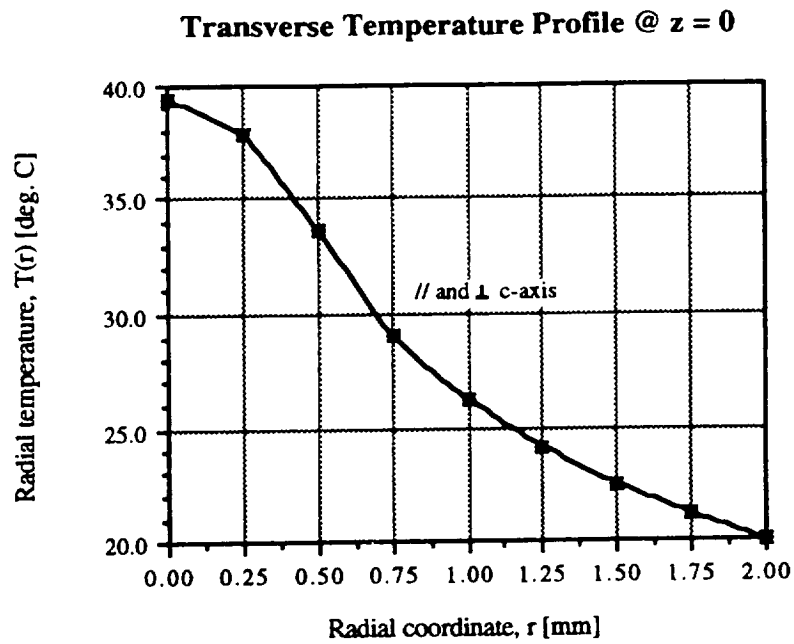


Figure 8-9. Calculated temperature distribution across the front face of the Nd:YLF rod at 5 W pump power.

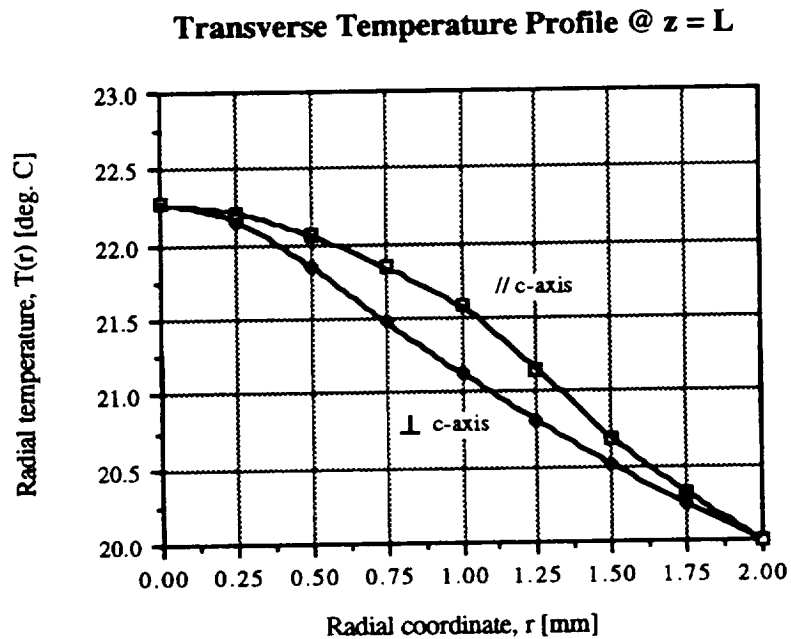


Figure 8-10. Calculated temperature distribution across the rear face of the Nd:YLF rod at 5 W pump power. Note scale change with respect to Figure 8-9.

### 8.3 Laser Development and Performance at the Fundamental Wavelength

This section contains the cw Nd:YLF laser performance data obtained at the fundamental wavelength, 1047 nm. It also traces the development of the laser resonator design over the course of the program. The topics within this section are presented in an order that roughly corresponds to the chronological order in which the work took place. Section 8.3.1 compares diode-pumping to Ti:Al<sub>2</sub>O<sub>3</sub>-pumping in simple standing-wave laser resonators. Section 8.3.2 discusses the resonator design issues which had to be addressed (including thermal lensing effects in the Nd:YLF) and explains the evolution of the laser resonator design. Section 8.3.3 presents the results obtained with a ring laser resonator design, which had a number of excellent features but several drawbacks as well. Section 8.3.4 discusses the development and performance of a standing-wave resonator that incorporated the best features of the ring laser resonator, without its drawbacks. The standing-wave resonator described in Section 8.3.4 was the final version of the cw Nd:YLF laser, in which the SHG experiments were then conducted.

#### 8.3.1 Diode-Pumped Performance vs. Ti:Al<sub>2</sub>O<sub>3</sub>-Pumped Performance

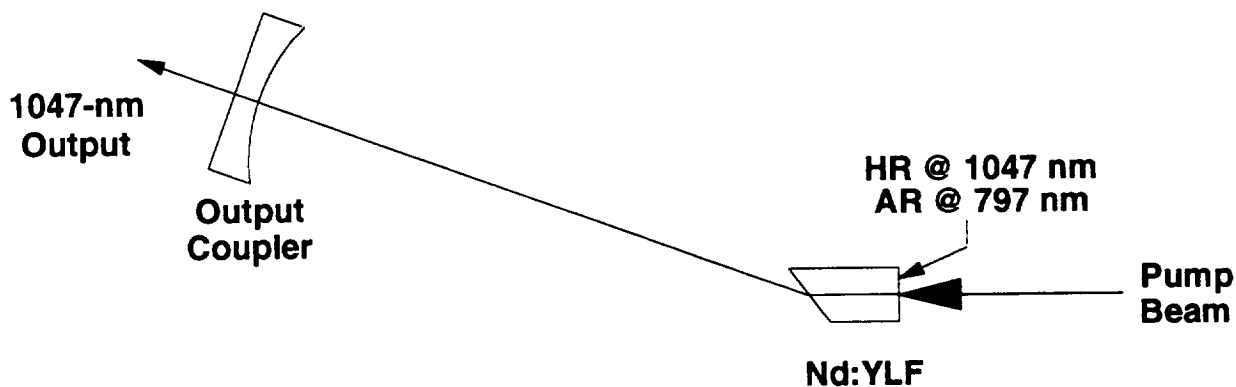
Initial laser experiments at the fundamental wavelength were carried out with very simple standing-wave resonators. Figure 8-11 shows the simple standing-wave resonator layouts for the flat/flat Nd:YLF crystal and for the flat/Brewster Nd:YLF crystal. In each case the "pumped" surface of the Nd:YLF, which was HR coated for 1047 nm, served as one end mirror of the cavity, and an output coupler was placed a short distance away. The curvature of the output coupler and the length of the resonator were chosen to produce the desired resonator mode size in the Nd:YLF crystal. We typically used an output coupler with a 4-5 m radius of curvature (concave) and a resonator length of 10-15 cm in these experiments. In the flat/flat Nd:YLF rod this combination produced a theoretical resonator mode size of 1.0 x 1.0 mm, which was intended to be a good match to the pump beam size. In the flat/Brewster Nd:YLF rod, the theoretical resonator mode size was 1.5 x 1.0 mm due to the effect of the Brewster surface; this was intended to match both the pump beam size and the ellipticity of the "effective" pump volume (as discussed in Section 8.2.3).

Low-power laser experiments were conducted using a cw Ti:Al<sub>2</sub>O<sub>3</sub> laser tuned to 797 nm, rather than the 10-W diode laser array, as a pump source. With the cw Ti:Al<sub>2</sub>O<sub>3</sub> laser we were limited to about 2.5 W of pump power. However, the Ti:Al<sub>2</sub>O<sub>3</sub> pump beam was TEM<sub>00</sub>, so these results provided a useful baseline for comparison with multimode diode-pumping.

The Ti:Al<sub>2</sub>O<sub>3</sub>-pumping experiments were carried out using the simple standing-wave resonators shown in Figure 8-11. We compared different output couplers (97%R vs. 99.5%R), different pump beam sizes (1.1 x 1.1 mm vs. 0.9 x 0.9 mm), and different Nd:YLF crystal types (flat/flat vs. flat/Brewster). We also tried pumping at 792 nm, another local peak absorption wavelength for Nd:YLF, rather than 797 nm; but we found that the laser performance was better at the design wavelength, 797 nm.



(a)



(b)

**Figure 8-11.** Simple standing-wave resonator layout for the cw Nd:YLF laser, (a) with flat/flat Nd:YLF; (b) with flat/Brewster Nd:YLF.

The results of the  $\text{Ti:Al}_2\text{O}_3$ -pumping experiments are summarized in Figures 8-12 and 8-13. Figure 8-12 compares the 97%R and the 99.5%R output couplers, with the 97%R output coupler producing the expected better slope. At these low pump powers the 95%R output coupler (not shown) gives approximately the same results as the 97%R output coupler; however, later diode-pumping experiments demonstrated that the 95%R output coupler was slightly better at high pump powers. Figure 8-13 shows the improvement in threshold that was obtained with a slightly smaller pump beam ( $0.9 \times 0.9 \text{ mm}$  vs.  $1.1 \times 1.1 \text{ mm}$ ) pumping the flat/flat Nd:YLF crystal, with a given resonator mode size ( $1.0 \times 1.0 \text{ mm}$ ). The results obtained with the flat/Brewster crystal are also displayed in Figure 8-13. In the case of the flat/Brewster crystal the resonator mode was elliptical inside the crystal ( $1.5 \times 1.0 \text{ mm}$ ); the  $\text{Ti:Al}_2\text{O}_3$  pump beam was expanded to

1.5 x 1.0 mm to match the resonator mode, using an anamorphic prism. The superior performance of the flat/Brewster crystal was most likely due to the low loss at its Brewster surface, as compared to the AR coated rear surface of the flat/flat rod.

Laser experiments were then conducted up to the full 10-W pump power using the 10-W diode laser array as the pump source. These experiments were carried out using the simple standing-wave resonators shown in Figure 8-11. The results appear in Figures 8-14 and 8-15, along with the best previous  $\text{Ti:Al}_2\text{O}_3$ -pumping results for comparison.

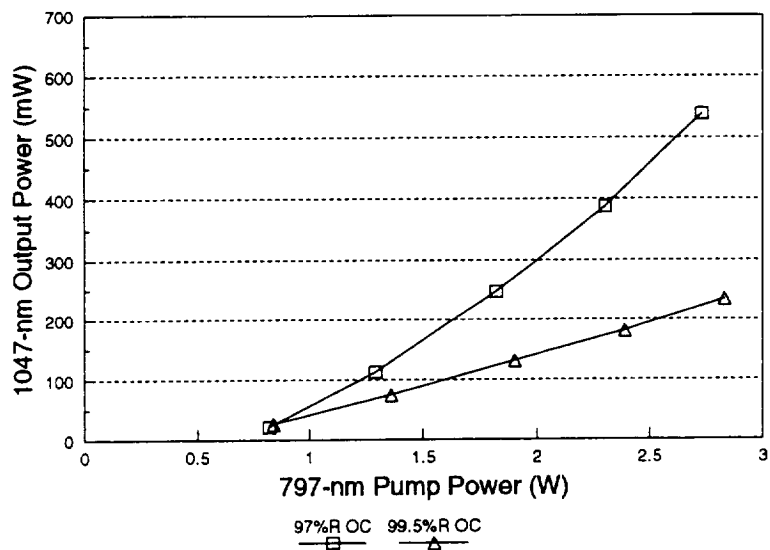


**Figure 8-12.** Ti:Al<sub>2</sub>O<sub>3</sub> pumping of the cw Nd:YLF laser: output coupler comparison (97%R vs. 99.5%R) with flat/flat Nd:YLF, 1.1x1.1 mm pump beam size, and 1.0x1.0 mm mode size.

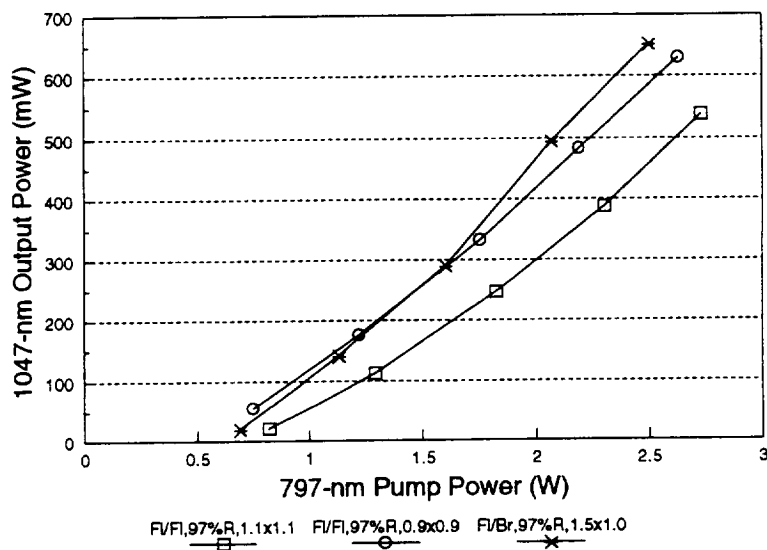


**Figure 8-13.** Ti:Al<sub>2</sub>O<sub>3</sub> pumping of the cw Nd:YLF laser: pump beam size comparison (1.1x1.1 mm vs. 0.9x0.9 mm) with flat/flat Nd:YLF, 97%R OC, and 1.0x1.0 mm mode size. Also shown: Flat/Brewster Nd:YLF with 97%R OC, 1.5x1.0 mm pump beam size, and 1.5x1.0 mm mode size.

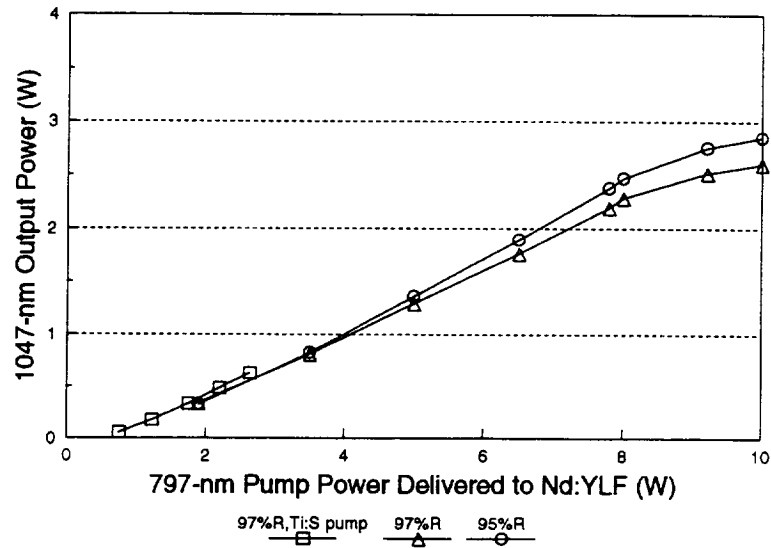


**Figure 8-14.** Diode pumping of the cw Nd:YLF laser: output coupler comparison (97%R vs. 95%R) with flat/flat Nd:YLF. Also shown: Ti:Al<sub>2</sub>O<sub>3</sub> pumping data with 97%R OC.

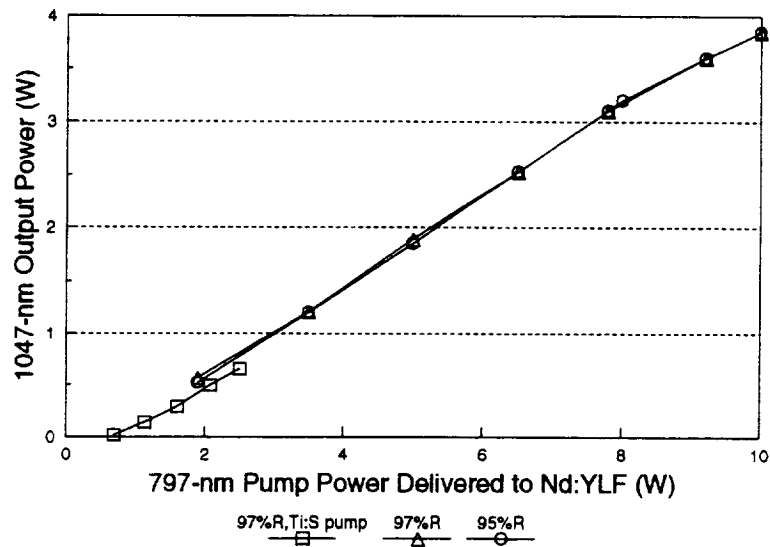


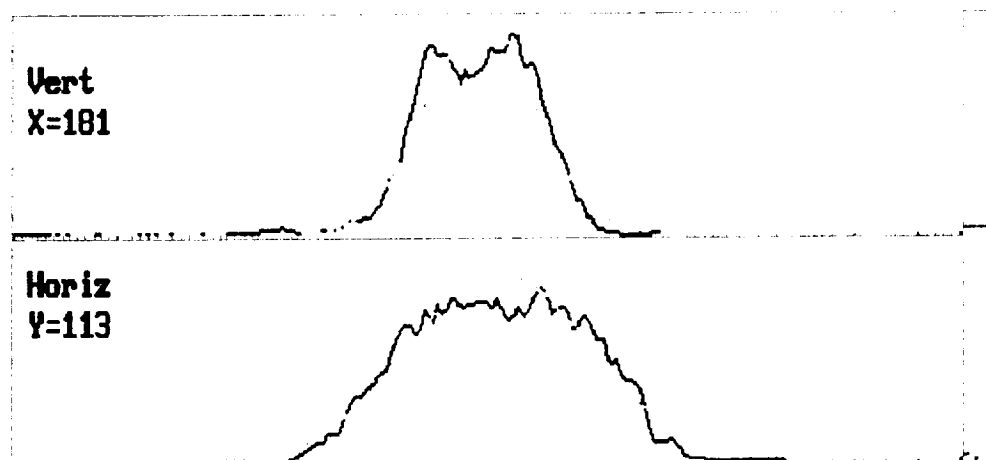
**Figure 8-15.** Diode pumping of the cw Nd:YLF laser: output coupler comparison (97%R vs. 95%R) with flat/Brewster Nd:YLF. Also shown: Ti:Al<sub>2</sub>O<sub>3</sub> pumping data with 97%R OC.



	Vert	Horiz
Correlation Coeff.	= 0.863	0.891
Peak Position	= 117	182
Beam Dia. @ 1/e <sup>2</sup> [mm]	= 1.487	2.144
Percent of Peak	= 102.914	89.632

<b>CENTROID</b>
(X,Y) = (181,113)
X (Vert) = 181
Y (Horiz) = 113

Active Cursor: Contour



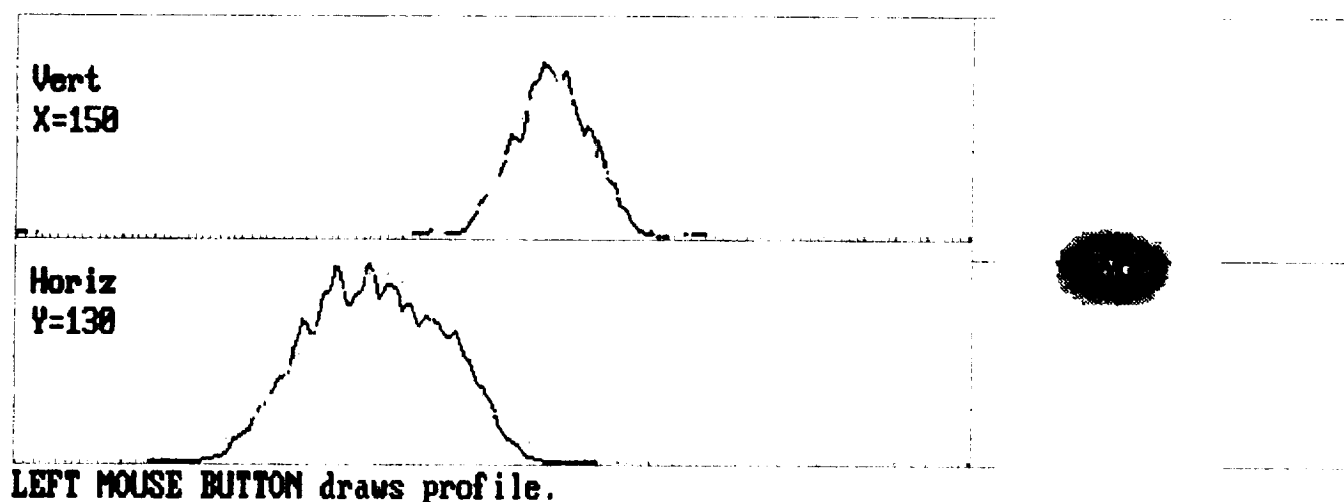
LEFT MOUSE BUTTON draws profile.

Press <ESC> to abort printing.

Figure 8-16. Output beam profile from the diode-pumped cw Nd:YLF laser, simple standing-wave resonator, flat/flat Nd:YLF rod.

<Gaussian Fit Data>			<Cursor Location>	
	Vert	Horiz	CENTROID	
Correlation Coeff.	= 0.966	0.913	(X,Y) = (150,130)	
Peak Position	= 133	149	Profile Location	
Beam Dia. @ 1/e <sup>2</sup> [mm]	= 1.056	1.678	X (Vert) = 150	
Percent of Peak	= 77.681	90.389	Y (Horiz) = 130	

Active Cursor: Contour



Press <ESC> to abort printing.

Figure 8-17. Output beam profile from the diode-pumped cw Nd:YLF laser, simple standing-wave resonator, flat/Brewster Nd:YLF rod.

Figure 8-14 shows the results obtained with the flat/flat Nd:YLF rod. At the 10-W pump power level, the 1047-nm output was 2.60 W with the 97%R output coupler, and 2.85 W with the 95%R output coupler. The diode-pumped performance was very close to the Ti:Al<sub>2</sub>O<sub>3</sub>-pumped performance, indicating that the power output of the laser did not suffer significantly from the fact that the pump beam was multimode rather than TEM<sub>00</sub>. At high power the output beam, shown in Figure 8-16, was highly multimode, two-lobed in the near field, astigmatic, and fairly sensitive to slight changes in resonator alignment.

Figure 8-15 shows the results obtained with the flat/Brewster Nd:YLF rod. At the 10-W pump power level, the 1047-nm output was 3.85 W with both the 97%R and 95%R output couplers. This was a significant improvement over the results obtained with the flat/flat Nd:YLF crystal. We attributed the improvement to the lower loss of the Brewster surface and the ellipticity of the resonator mode, which better matched the elliptical "effective" pump volume. In this case the diode-pumped performance was actually slightly better than the Ti:Al<sub>2</sub>O<sub>3</sub>-pumped performance. At high power the output beam, shown in Figure 8-17, was still multimode and astigmatic; but the mode quality was somewhat improved and more stable than it had been for the flat/flat crystal.

In summary, using a simple standing-wave resonator, we obtained up to 3.85 W of output power at the fundamental wavelength with 10 W of diode-laser pump power delivered to the crystal. The output was multimode and astigmatic. In terms of power output, multimode pumping with the focused diode-laser pump beam was as effective as TEM<sub>00</sub> pumping with a cw Ti:Al<sub>2</sub>O<sub>3</sub> laser.

### 8.3.2 Resonator Design Issues

#### *Design Goals*

The ultimate goal of this portion of the program was to produce 1 W of cw power at the second harmonic wavelength, 523.5 nm, in a TEM<sub>00</sub> beam. In view of that goal, several constraints and requirements were placed on the resonator design and performance at the fundamental wavelength. First, sufficient power had to be generated at the fundamental wavelength for conversion to 1 W of second harmonic power. (Our initial goal was 4 W of power at 1047 nm.) Second, that power had to be generated in a TEM<sub>00</sub> beam. Third, the resonator was required to have an intracavity waist on the order of 100  $\mu$ m in diameter, for intracavity frequency-doubling. Fourth, the resonator had to be constructed to allow efficient extraction of the second harmonic power, preferably in a single output beam. Fifth, the depolarization effects introduced by the frequency-doubling crystal, in the case of Type II SHG, had to be accounted for. Finally, the resonator was required to be as short and compact as possible, for reasons of mechanical stability and packaging practicality.

With the simple standing-wave resonator we successfully met the output power requirements, but clearly a more complex resonator would be needed to achieve the other goals. Our approach was to build the complexity of the resonator in stages; the first step was to modify the standing-wave resonator as necessary to produce a TEM<sub>00</sub> output beam. Our end goal was a unidirectional ring laser meeting all of the requirements listed above. The unidirectional ring laser was our baseline design because it offered two advantages: (1) the second harmonic output would be inherently unidirectional; and (2) the ring laser could be made single-frequency, which we anticipated might be necessary to make the second harmonic output power stable.

### ***Mode Quality in the Simple Standing-Wave Resonator***

The first task was to modify the simple standing-wave resonator to produce as much power as possible in a TEM<sub>00</sub> output beam. As described earlier, the output of the simple standing-wave resonator at full power was multimode and astigmatic. We made a series of measurements to further characterize the beam quality. We found that at low power the output was near-TEM<sub>00</sub> ( $M^2 < 1.1$  and only slightly astigmatic), up to approximately 4 W of pump power, corresponding to about 1 W of output power. As the pump power increased, the output beam quality deteriorated and the astigmatism became more severe. In addition, a marked difference developed between the beam characteristics in the horizontal plane and the beam characteristics in the vertical plane; for this reason it became necessary to characterize the beam quality separately in the two planes, using values of  $M_x^2$  and  $M_y^2$ . At a pump power of 8 W (output power of 3.2 W), values of  $M_x^2 = 2.3$  and  $M_y^2 = 1.7$  were measured. At the full pump power of 10 W, the beam quality worsened further and the beam developed lobes in the far field, making it difficult to obtain accurate  $M^2$  values.

We theorized that the poor mode quality of the output beam was due to an overfilling of the resonator mode by the pump volume. Accordingly, we attempted to improve the mode quality by increasing the resonator mode size inside the Nd:YLF crystal. This was done by adjusting the curvature of the output coupler and the length of the resonator. However, during the course of these experiments it became clear that the poor mode quality was primarily due to a different factor: strong, positive, asymmetric thermal lensing effects in the Nd:YLF crystal.

### ***Thermal Lensing Measurements***

The thermal lensing effects in the flat/Brewster Nd:YLF crystal were measured directly, as a function of diode-laser pump power, using a 1064-nm cw probe laser. The Nd:YLF crystal was found to have strong, positive, asymmetric net thermal lensing. At 10 W pump power, with a p-polarized probe beam, the crystal acted as a thermal lens with a focal length of  $f_x = 40$  cm (in the horizontal plane) and  $f_y = 100$  cm (in the vertical plane). A plot of the thermal lens focal lengths  $f_x$  and  $f_y$ , as a function of pump power, appears in Figure 8-18. Values are shown for both "p" and "s" probe-beam polarizations; the "p" polarization is the relevant one in our case. This asymmetric thermal lensing was determined to be a major factor contributing to the astigmatism and poor mode quality of the output beam.

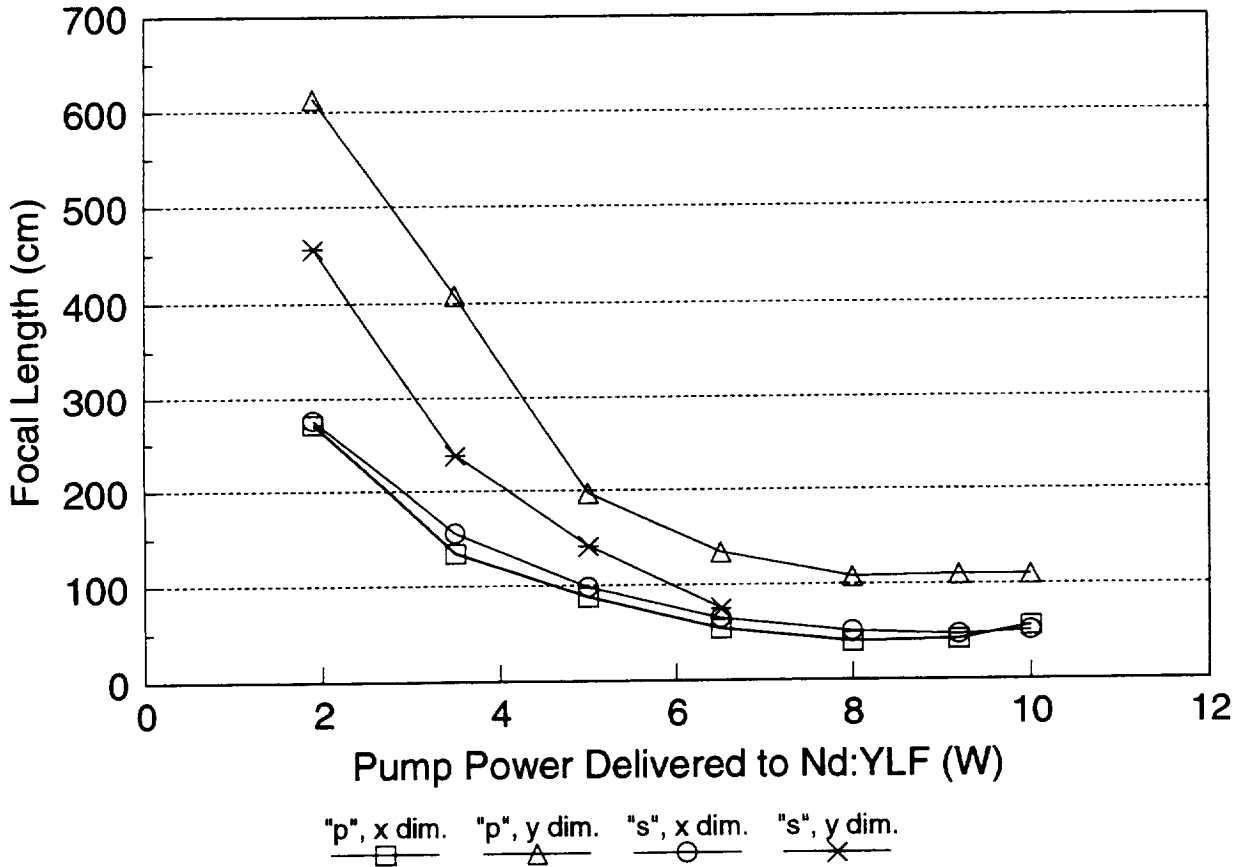


**Figure 8-18.** Thermal lensing in the flat/Brewster Nd:YLF crystal as a function of pump power.

Thermal lensing in Nd:YLF, while astigmatic, is generally considered to be a relatively minor effect. For example, in one comparison of Nd:YAG and Nd:YLF rods lamp-pumped at 700 W average power, the Nd:YAG rod was reported to have a focal length of 8 m, while the Nd:YLF rod had a focal length of -60 m for the "p" polarization and  $>\pm 150$  m for the "s" polarization [9]. In another study, a Nd:YLF rod lamp-pumped at 5 kW was reported to have focal lengths of -2 m ("p" polarization, a-b plane), -4 m ("p" polarization, a-c plane), +7 m ("s" polarization, a-b plane), and -7 m ("s" polarization, a-c plane) [10]. But these results, like most of the available thermal lensing data for Nd:YLF, are for long rods side-pumped by flashlamps. Our particular configuration is different in that the Nd:YLF crystal is only 5 mm long, and it is end-pumped by an extremely high pump fluence. The short crystal length and high-fluence end-pumping conditions may help to explain the fact that strong positive thermal lensing effects were encountered in our Nd:YLF crystal. Our speculation is that the thermal lensing is due to three competing effects: end face curvature of the Nd:YLF rod (which would tend to produce positive lensing), refractive index variation with temperature (which would tend to produce negative lens-

ing), and an unknown stress-optic contribution. We speculate that in our case, the end face curvature is a strong effect due to the high-fluence end-pumping, and the refractive index variation is a weak effect over the short length of the rod. The net result is therefore positive lensing. So far this explanation is only supposition; we anticipate that as the thermal modeling study described in Section 8.2.3 progresses, it will shed further light on thermal lensing effects in end-pumped Nd:YLF.

One interesting consequence of the positive thermal lensing in the Nd:YLF crystal was that the simple standing-wave resonator could be operated with a flat output coupler, a configuration which would be unstable in the absence of thermal lensing. We constructed such a resonator using the flat/Brewster Nd:YLF crystal and a 95%R flat output coupler. At 8 W pump power we obtained 3.0 W output with  $M_x^2 = 1.8$  and  $M_y^2 = 1.1$ , compared to 3.2 W output with  $M_x^2 = 2.3$  and  $M_y^2 = 1.7$  obtained previously with the concave output coupler. Thus, the simple standing-wave resonator, operated with a flat output coupler, produced slightly less output in a somewhat better mode. However, the beam was still too multimode and astigmatic to be satisfactory; and an attempt to lengthen the resonator and insert intracavity lenses resulted, predictably, in extremely poor mode quality.

From both theoretical resonator modeling and experimental results, it was clear that the resonator would have to incorporate some form of compensation for the asymmetric thermal lensing. In an uncompensated resonator, such as the simple standing-wave configuration, the thermal lensing effects would asymmetrically distort the resonator mode and lead to poor output beam quality.

### ***Compensated Resonator Design: Proof of Principle***

Quantification of the thermal lensing effects allowed us to take those effects into account in the resonator design. Specifically, the introduction of astigmatic optical elements into the resonator enabled us to compensate for the asymmetric thermal lensing in the laser crystal. In this "compensated" resonator design approach, the x and y planes of the resonator were modelled separately, each with its appropriate thermal lens; and astigmatic optical elements such as cylindrical reflectors and tilted curved mirrors were used to produce the desired resonator mode in each plane.

We conducted a proof-of-principle experiment in compensated resonator design, using optics available in the laboratory. We designed a standing-wave resonator with a series of concave mirrors at 30° incidence, chosen to produce a symmetric resonator mode at the output coupler. This resonator is shown in Figure 8-19. There was some leakage through the curved mirrors at this angle of incidence. With this resonator we obtained 2.75 W of 1047-nm output power, plus 0.36 W in the combined leakage beams, at the 10-W pump power level. The mode quality of the output beam was excellent ( $M^2 \leq 1.2$  at high power) and the astigmatism was virtually eliminated. A profile of the beam appears in Figure 8-20.

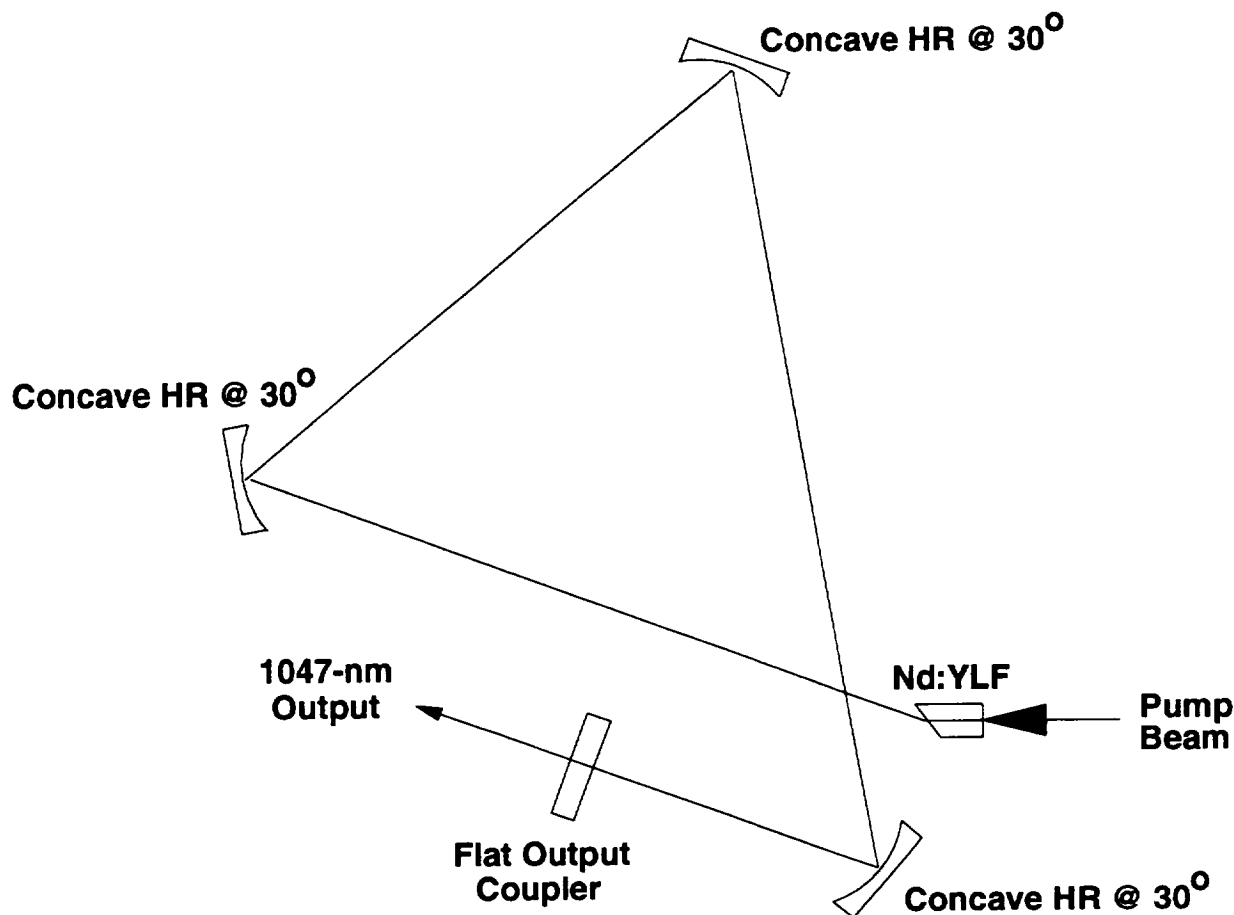


**Figure 8-19.** Standing-wave cw Nd:YLF resonator, with off-axis curved mirrors for compensation of asymmetric thermal lensing (proof-of-principle experiment).

This proof-of-principle experiment successfully demonstrated, using available optics, compensation for asymmetric thermal lensing in order to achieve good mode quality. It also demonstrated the necessity of designing the resonator for a specific operating point. Since the thermal lensing effects are pump-power dependent, the resonator mode may change significantly, or even become unstable, at some pump-power levels. This was the reason for the poor mode quality at high power in the simple standing-wave resonator, which was designed for zero thermal lensing. In contrast, this proof-of-principle resonator was designed for the full-pump-power lensing, and was actually unstable at pump powers below about 5 W. (An I/O curve is not given for the resonator for this reason -- it would show an artificially high slope.)

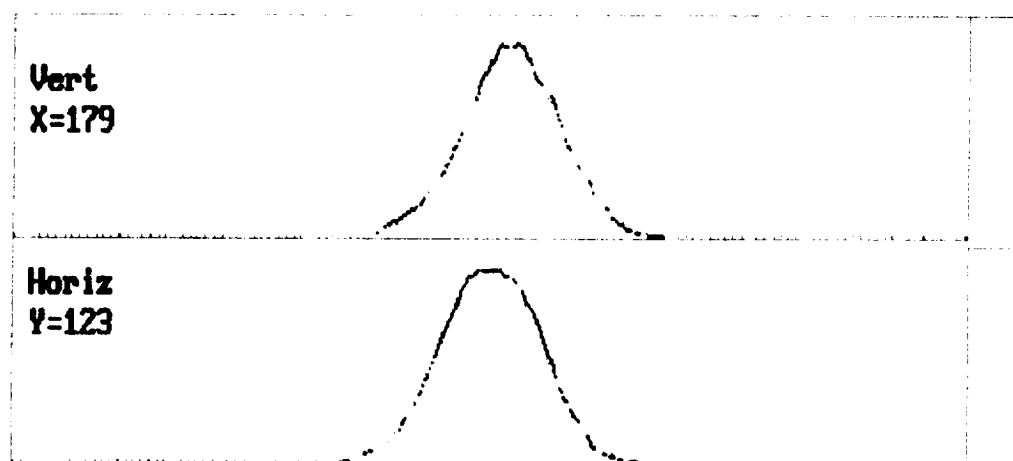
Using the information gained from this proof-of-principle experiment, we proceeded with the design of a ring resonator with appropriate compensation for the asymmetric thermal lensing.



(Gaussian Fit Data)		
	Vert	Horiz
Correlation Coeff.	= 0.985	0.977
Peak Position	= 124	179
Beam Dia. @ $1/e^2$ [mm]	= 1.291	1.184
Percent of Peak	= 88.851	94.295

(Cursor Location)	
<b>CENTROID</b>	
(X,Y) = (179,123)	
Profile Location	
X (Vert)	= 179
Y (Horiz)	= 123

Active Cursor: Contour



LEFT MOUSE BUTTON draws profile.

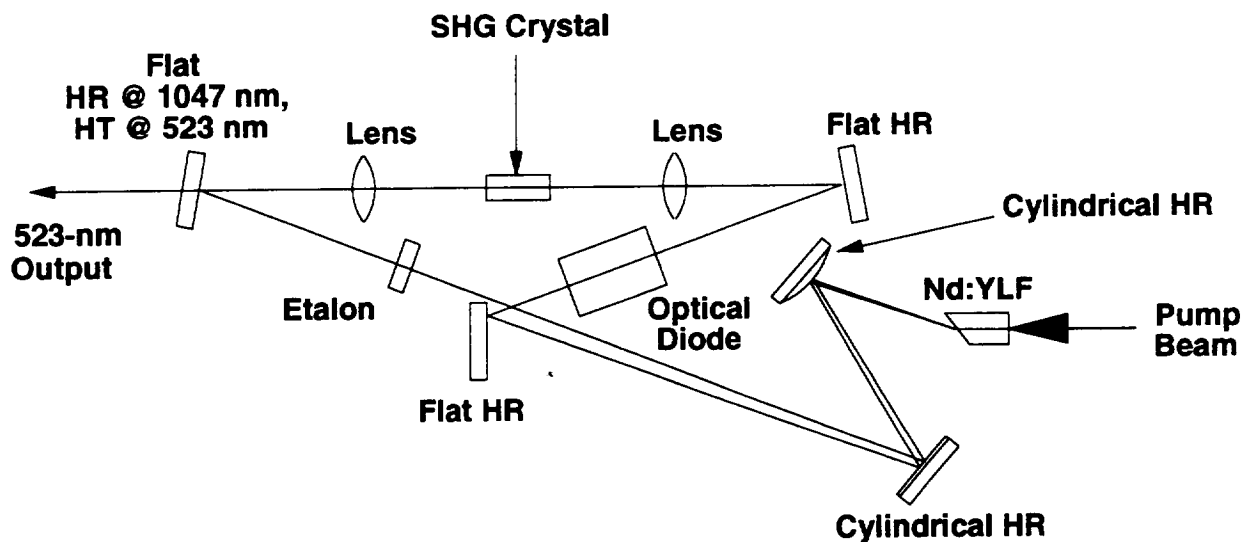
Press <ESC> to abort printing.

Figure 8-20. Output beam profile from the diode-pumped cw Nd:YLF laser, standing-wave resonator with off-axis curved mirrors for compensation of asymmetric thermal lensing (proof-of-principle experiment).



### 8.3.3 Ring Resonator Design and Performance

The issues addressed in our ring resonator design included compensation for the asymmetric thermal lensing, shortest practical overall resonator length, placement of intracavity line-narrowing elements, and creation of an intracavity beam waist for SHG crystal placement. We chose to use cylindrical reflectors in our design, which allowed us to achieve the necessary compensation for asymmetric lensing while minimizing the overall resonator length and the angles of incidence on the turning optics. The ring resonator design is shown in Figure 8-21. The two cylindrical reflectors compensate for the full-pump-power thermal lensing in their leg of the resonator, so that the resonator mode is symmetric throughout the rest of the resonator. Space is provided for an optical diode and an etalon (or other line-narrowing elements). Intracavity lenses create a beam waist at the location of the SHG crystal. The SHG output power is extracted through one of the corner fold mirrors of the resonator.



**Figure 8-21.** Unidirectional ring resonator design for the cw Nd:YLF laser, compensated for thermal lensing.

We built the ring resonator as shown in Figure 8-21, initially leaving out the optical diode, etalon, and SHG crystal. With a flat 95%R 1047-nm output coupler taking the place of the corner HR/HT mirror, we evaluated the performance of the ring laser at the fundamental wavelength. The output was two-directional since the optical diode was not yet in place. Summing the two output beam powers, we obtained a maximum of only 560 mW output at 1047 nm from the ring laser. This was much lower than we had anticipated, and too low to be of practical use.

The output mode symmetry was good, indicating that the thermal lensing compensation was working well; but the beam quality was highly alignment-sensitive, and varied greatly even with small adjustments that did not alter the output power.

Several variations on the ring resonator were tried, including concave output couplers, output couplers of different reflectivities, and different lens spacings. Some of these variations produced more output power, but in poor-quality modes; none of the configurations produced a useful amount of output power in a good mode.

We attributed the ring laser's low output power to the greater number of surfaces and longer cavity length of the ring resonator. Even without the optical diode, etalon, and SHG crystal, the ring resonator contained eight reflective and six transmissive surfaces per round trip (as compared to the simple standing-wave resonator, for example, which contained two reflective and two transmissive surfaces per round trip). The unavoidably longer path length of the ring resonator, approximately two meters, was a factor as well. We attributed the alignment sensitivity of the mode to the greater inherent difficulty of maintaining optimum alignment in a ring laser, as compared to a standing-wave laser. These were all problems that we had anticipated during the design, but we had expected more success in overcoming them with high-quality optical coatings and careful resonator alignment. The HR coatings on the cylindrical reflectors were indeed lossier than we had anticipated, which contributed to the problem, but the main difficulty appeared to be the length and complexity of the ring resonator itself.

Nevertheless, the ring resonator did have some excellent features. The resonator mode size in the Nd:YLF crystal ( $1.58 \times 1.00$  mm) was well matched to the effective pump volume. The mode was symmetric throughout the resonator, except in the section containing the cylindrical reflectors and the laser crystal. The intracavity lenses proved to be a low-loss method of producing an intracavity waist. Lens pairs of various focal lengths could be inserted to vary the waist size, without disturbing the stability or compensation of the resonator. Most importantly, the thermal lensing compensation arrangement, using two cylindrical reflectors, was successful. It was also found to work well over a wide range of thermal lensing values, not only the full-pump-power values that it was designed for. We decided to use these features of the ring resonator design as the basis for building a compensated standing-wave resonator.

### **8.3.4 Standing-Wave Resonator Design and Performance**

As mentioned earlier, the unidirectional ring laser had been our baseline design because it offered two advantages: (1) the second harmonic output would be inherently unidirectional; and (2) the ring laser could be made single-frequency, which we anticipated might be necessary to make the second harmonic output power stable. However, a unidirectional ring laser is not the only way to achieve unidirectional and stable second harmonic output; and in view of the low output power of the ring laser, we decided to revise our approach. We used the ring resonator design as the basis for a compensated standing-wave resonator design that incorporated the best features of the ring resonator, without its drawbacks.

The compensated standing-wave resonator design is shown in Figure 8-22. It is identical in resonator mode parameters and cylindrical reflector configuration to the ring resonator design. However, the standing-wave design requires less complexity, fewer folds, and a shorter overall cavity length. Again, the resonator mode in the Nd:YLF crystal (1.58 x 1.00 mm) is a good match to the effective pump volume. The cylindrical reflectors perform the same compensation for full-pump-power thermal lensing. Again, the resonator mode is symmetric in the resonator leg which contains the lenses and the SHG crystal. The intracavity waist size may be easily varied by changing intracavity lens pairs. No optical diode or line-narrowing elements are required, since unidirectionality and single-frequency operation are not issues. The flat mirror at the end of the resonator may be a 1047-nm output coupler for evaluating the performance at the fundamental wavelength, a 1047-nm HR for SHG operation, or a dual-band (1047-nm and 523.5-nm) HR for SHG operation in which the two-directional second harmonic output is recombined into a single output beam.

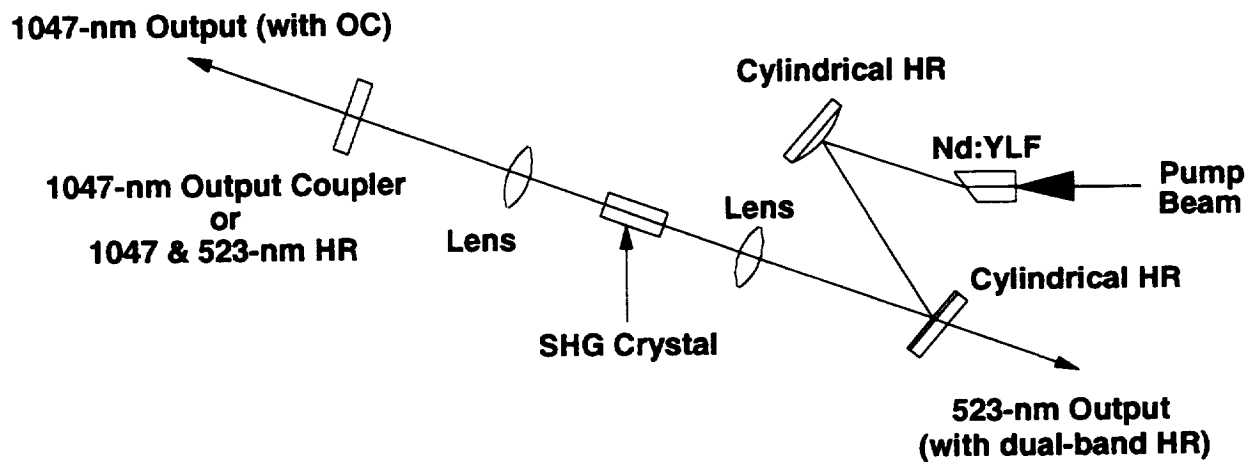


**Figure 8-22.** Standing-wave resonator design for the cw Nd:YLF laser, compensated for thermal lensing.

The compensated standing-wave resonator was built as shown in Figure 8-22, initially leaving out the SHG crystal. Its performance at the fundamental wavelength was evaluated using a flat 95%R 1047-nm output coupler. There was some leakage through the cylindrical reflectors since, as noted previously, their HR coatings were lossier than anticipated. An I/O curve for the laser appears in Figure 8-23, showing the main beam output power and the total output power including leakage. The I/O does not show a constant slope because the resonator parameters change due to thermal lensing over the pump power range. A main output of 1.45 W (1.78 W including leakage) was obtained at the 10-W pump power level. We considered this a

respectable output power level for a laser that satisfied so many other requirements, particularly one having good mode quality and an intracavity waist. Note that the performance of the laser was quite good even at low pump power levels, which indicates that the thermal lens compensation was successful over a wide range of lensing values. The output beam mode quality was excellent; a profile of the full-power output beam appears in Figure 8-24.

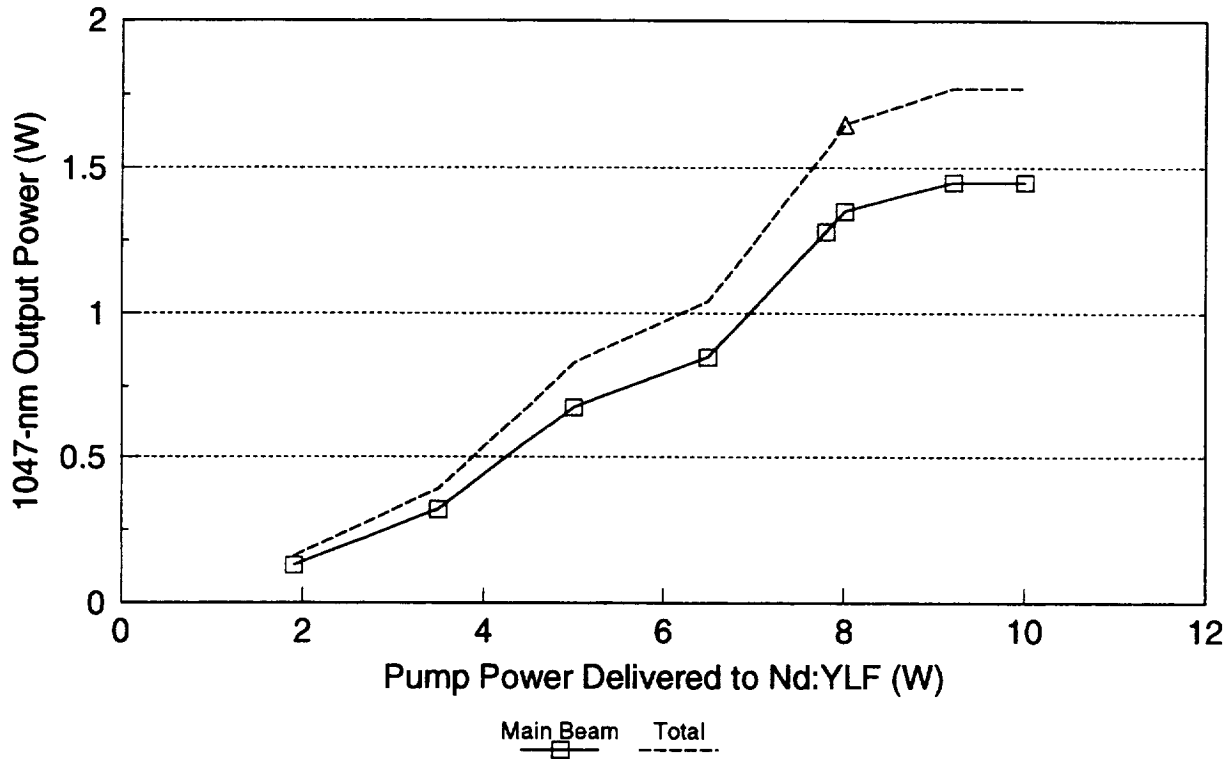


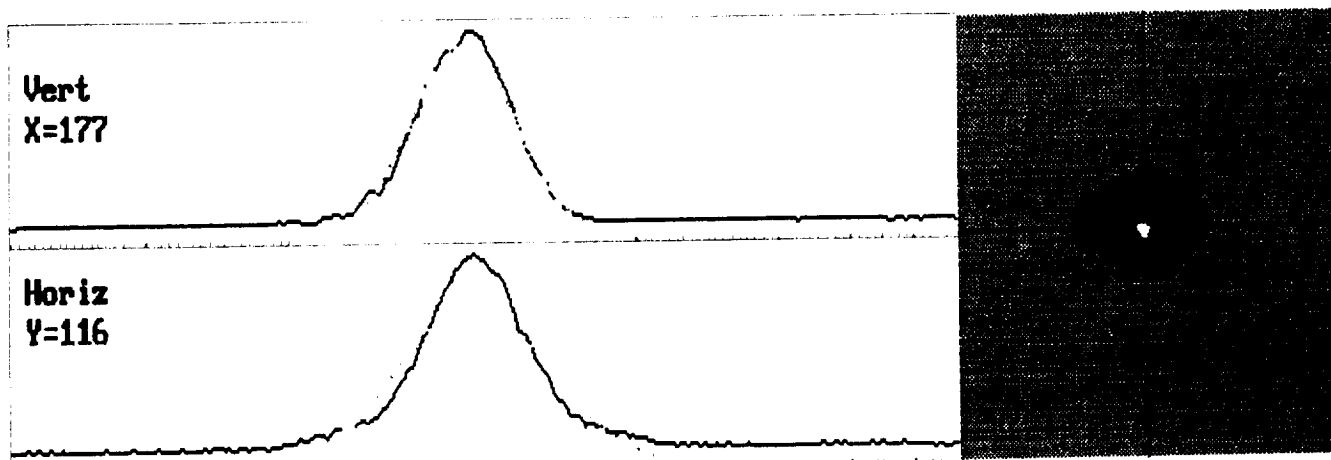
**Figure 8-23.** I/O data at the fundamental wavelength for the standing-wave cw Nd:YLF laser.

The compensated standing-wave resonator was successful in meeting the basic requirements set for laser performance at the fundamental wavelength. Sufficient power was obtained for useful conversion to the second harmonic wavelength; the power was obtained in a beam of good mode quality; an intracavity waist for the SHG crystal was provided; the SHG power could be extracted through the end mirror and the second cylinder lens, or through the second cylinder lens alone by making the end mirror a dual-band HR; the resonator was reasonably short and compact; and the asymmetric thermal lensing effects in the Nd:YLF were well compensated. With this task accomplished, we began actual SHG experiments in the compensated standing-wave resonator.

Gaussian Fit Data		
	Vert	Horiz
Correlation Coeff.	= 0.928	0.864
Peak Position	= 114	176
Beam Dia. @ $1/e^2$ [mm]	= 1.448	1.738
Percent of Peak	= 92.784	76.581

(Cursor Location)	
PEAK	
(X,Y) = (177,116)	
Profile Location	
X (Vert)	= 177
Y (Horiz)	= 116

Active Cursor: Contour



LEFT MOUSE BUTTON draws profile.

Press <ESC> to abort printing.

Figure 8-24. Output beam profile from the diode-pumped cw Nd:YLF laser, standing-wave resonator compensated for thermal lensing.

## 8.4 Laser Performance at the Second Harmonic Wavelength

The standing-wave resonator compensated for thermal lensing, discussed in Section 8.3.4 and shown in Figure 8-22, was used for the intracavity frequency-doubling experiments. We investigated the performance of two SHG crystals: LBO (Type I) and KTP (Type II). Section 8.4.1 discusses the results obtained with the LBO crystal. Section 8.4.2 presents the results obtained with the KTP crystal. Power stability and intensity noise are discussed in Section 8.4.3. An analysis of the results of the SHG experiments is given in Section 8.4.4.

### 8.4.1 Intracavity Type I SHG Using LBO

The LBO we used for the SHG experiments was a 3x3x15 mm, Type I, 90° noncritically phase-matched crystal available at SEO. The crystal was mounted in an oven supplied by a commercial vendor for heating to 172°C, the phase-matching temperature for SHG at 1047 nm. Since LBO is a Type I crystal, it was oriented with its axes parallel to the fundamental polarization, so it did not introduce any depolarization effects in the resonator. The circulating fundamental power remained p-polarized, and the second harmonic power was generated in an s-polarized beam.

We began the SHG experiments with an intracavity lens pair of focal lengths  $f = 10$  cm, which produced a waist of approximately 160  $\mu\text{m}$  diameter at the location of the LBO crystal. In this configuration we obtained 332 mW of SHG output at a pump power level of 10 W. The SHG output was two-directional since we had not yet installed the dual-band HR. By measuring the 1047-nm leakage through mirrors of known reflectivity in the resonator, we were able to estimate the circulating fundamental power and calculate the SHG conversion efficiency. Under these conditions the conversion efficiency with respect to intracavity fluence was 0.9%.

We installed an intracavity lens pair with shorter focal lengths,  $f = 5$  cm, in order to reduce the waist size to approximately 80  $\mu\text{m}$  at the location of the LBO crystal. We installed the dual-band HR to recombine the two-directional SHG output into a single output beam. During the course of the experiments we found that the second cylindrical reflector (the long-radius one) could be replaced by a flat 1047-nm HR/523-nm HT mirror without significantly affecting the mode quality, which gave us better green transmission out of the resonator. In this configuration we obtained 900 mW of SHG output, in a single beam, at a pump power level of 10 W. This corresponded to a conversion efficiency of 2.8% with respect to intracavity fluence. Figure 8-25 shows the SHG output as a function of diode-laser pump power delivered to the Nd:YLF crystal. The laser performed well at the second harmonic wavelength even at low pump power, indicating good compensation for the changing thermal lens effects over the pump power range. The mode quality of the SHG output beam was excellent:  $M_x^2 = 1.2$  and  $M_y^2 = 1.6$ , with no significant astigmatism. A profile of the 523-nm output beam appears in Figure 8-26.

Further LBO SHG experiments were performed under separate funding. For this reason they not included here, but are instead presented in Appendix B of this report (Section 14). In these experiments we obtained a total of 1.25 W of SHG output in two beams, at a pump power of 10 W. See Appendix B for details.

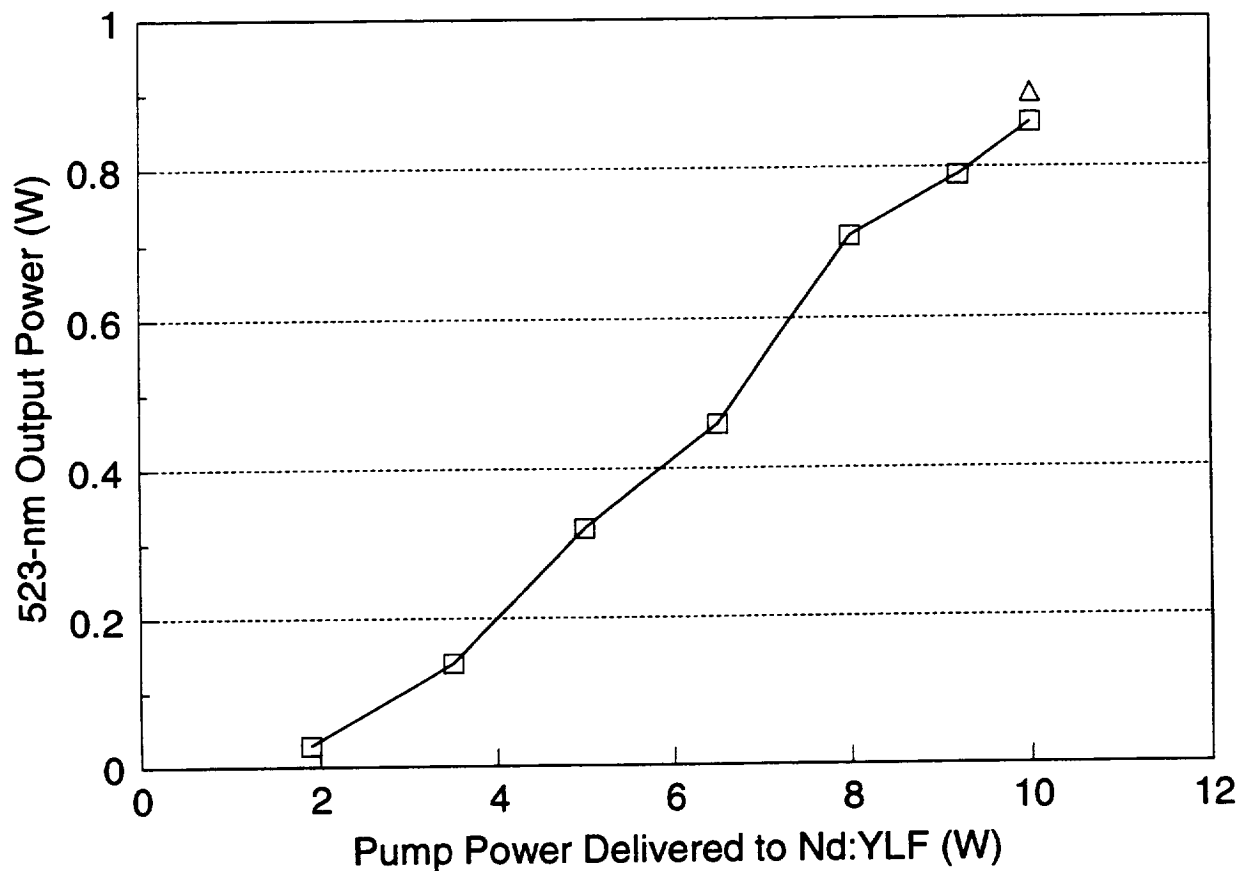
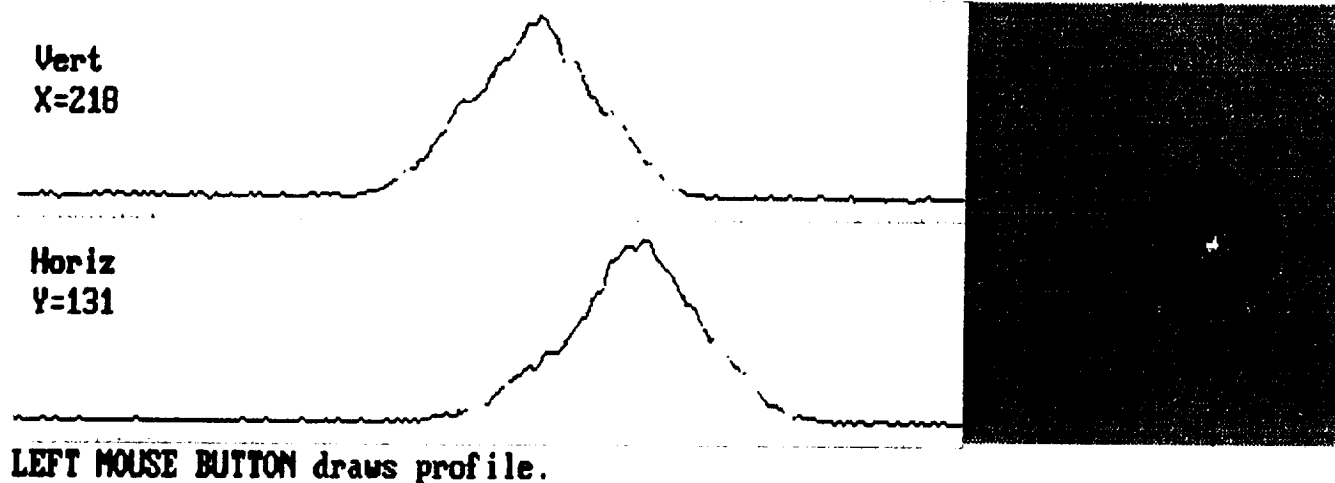


**Figure 8-25.** 523-nm I/O for the cw diode-pumped Nd:YLF laser, intracavity doubled using LBO.

Correlation Coeff.	= 0.894	0.876
Peak Position	= 129	215
Beam Dia. @ $1/e^2$ [mm]	= 2.071	2.033
Percent of Peak	= 84.543	77.977

PEAK	
(X,Y) = (218,131)	
X (Vert)	= 218
Y (Horiz)	= 131

Active Cursor: Contour



Press <ESC> to abort printing.

Figure 8-26. Second harmonic (523-nm) output beam profile from the diode-pumped cw Nd:YLF laser, intracavity doubled using LBO.



### 8.4.2 Intracavity Type II SHG Using KTP

The KTP we used for the SHG experiments was a 3x3x5 mm, Type II, 39°-cut crystal. It was mounted in a sealed, heated cell designed and assembled at SEO. The KTP was heated for two reasons. First, heating reduced the likelihood of "grey tracking" damage to the KTP crystal. Second, heating was necessary for polarization control in the resonator. Since KTP is a Type II SHG crystal, it must be mounted with its axes at 45° to the fundamental polarization, introducing depolarization effects in the resonator. The original plan was to tune the KTP to a full-wave temperature in order to eliminate the depolarization effects. For our KTP crystal, full-wave temperatures occurred at approximately every 25°C. In practice we found that while a full-wave temperature was readily determined and set (we chose 60.3°C), the polarization purity of the KTP crystal was not good enough even at that temperature. It was necessary to add an AR coated quarter-wave plate in the resonator, between the KTP crystal and the dual-band HR, to further reduce the depolarization effects.

We conducted the KTP SHG experiments with the 5-cm intracavity lenses, the dual-band HR, and the flat HR/HT replacing one of the cylindrical reflectors (the same resonator configuration in which we obtained 900 mW of SHG with the LBO crystal). The major differences were the Type II SHG crystal, the addition of the AR coated quarter-wave plate, and the 5° angle of incidence necessary to achieve phase-matching with the KTP crystal at this wavelength and temperature. In this configuration, we obtained 304 mW of SHG output at a pump power level of 10 W. This corresponded to a conversion efficiency of 1.9% with respect to intracavity fluence. The SHG output as a function of diode-laser pump power is shown in Figure 8-27. A profile of the SHG output beam appears in Figure 8-28.

It should be noted that while the SHG output obtained with the KTP crystal was low compared to the output obtained with the LBO crystal, the actual conversion efficiencies were not dissimilar. The circulating fundamental power in the resonator was lower in the case of the KTP crystal. This was primarily due to the depolarization effects in the Type II KTP, the addition of an intracavity quarter-wave plate, and the off-normal angle of incidence required for the KTP crystal in the resonator. These issues are further discussed in Section 8.4.4.

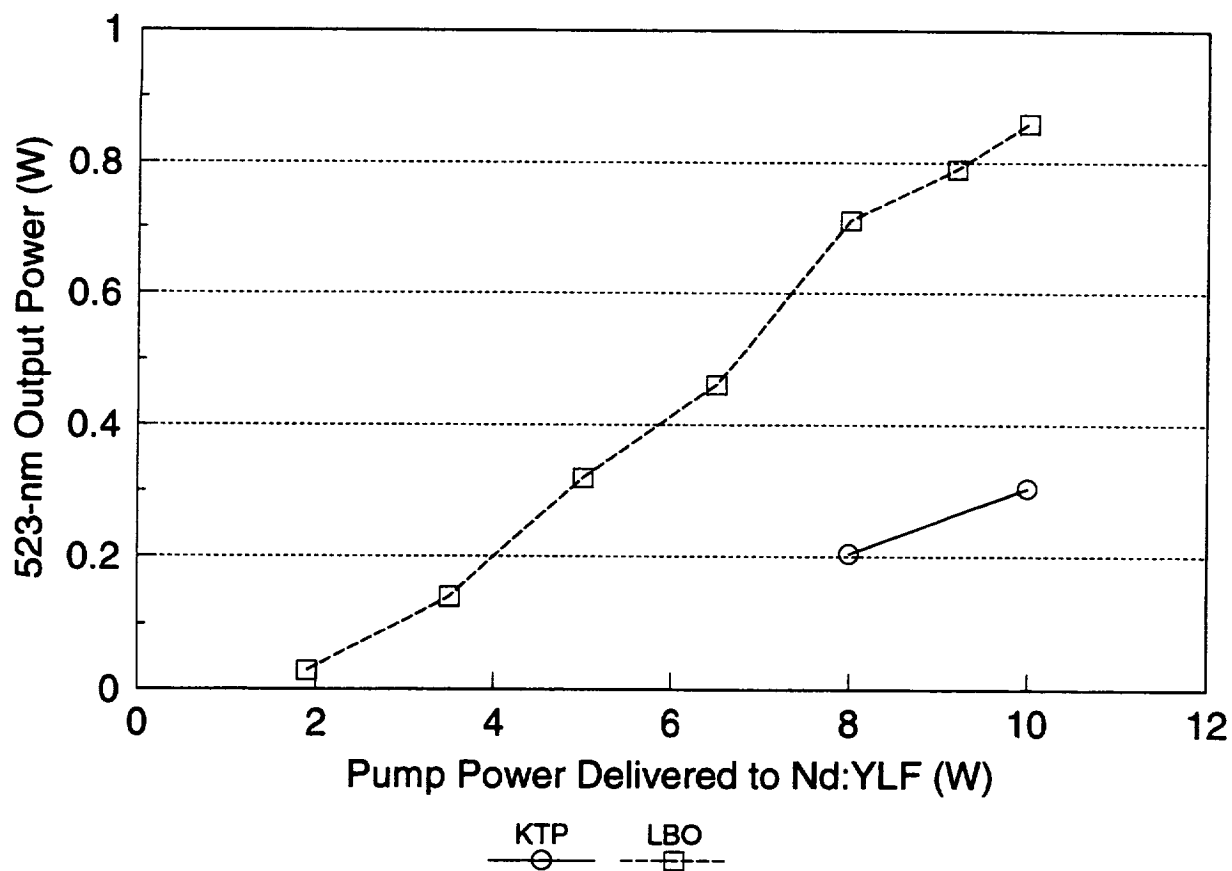
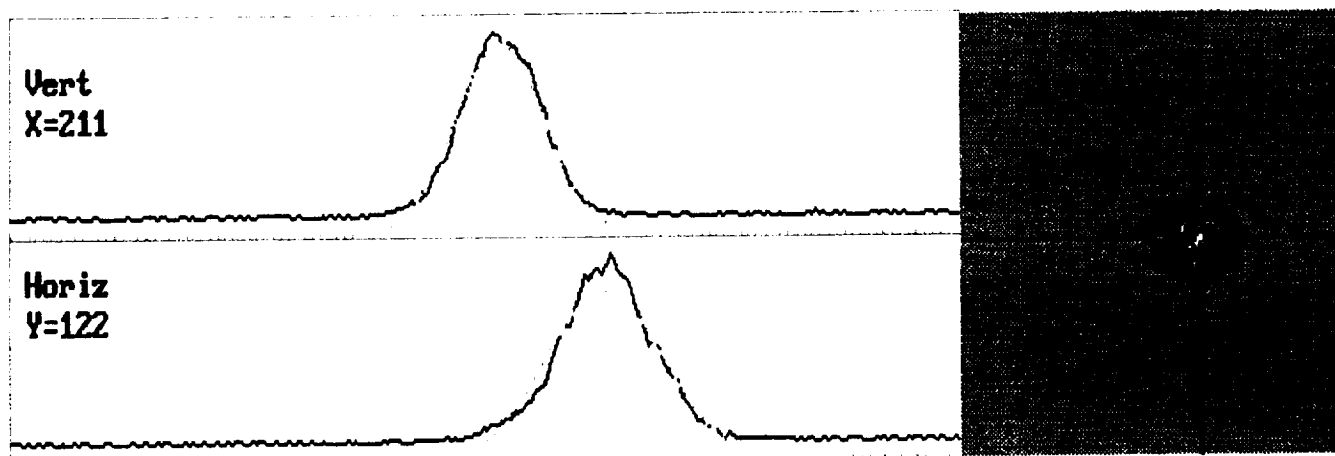


**Figure 8-27.** 523-nm I/O for the cw diode-pumped Nd:YLF laser, intracavity doubled using KTP. The previous I/O obtained using LBO is shown for comparison.

(Gaussian Fit Data)			(Cursor Location)	
	Vert	Horiz	PEAK	
Correlation Coeff.	= 0.925	0.982	(X,Y) = (211,122)	
Peak Position	= 123	289	Profile Location	
Beam Dia. @ 1/e <sup>2</sup> [mm]	= 1.225	1.337	X (Vert) = 211	
Percent of Peak	= 91.261	88.388	Y (Horiz) = 122	

Active Cursor: Contour



LEFT MOUSE BUTTON draws profile.

Press <ESC> to abort printing.

Figure 8-28. Second harmonic (523-nm) output beam profile from the diode-pumped cw Nd:YLF laser, intracavity doubled using KTP.

### 8.4.3 Power Stability and Intensity Noise

#### *Power Stability*

During the initial SHG experiments using LBO, we found that the SHG output power tended to drift slowly over time. The typical pattern was a gradual power drift down to two-thirds or so of the peak power over the course of five or ten minutes, sometimes with slow oscillations back up near the peak. Most or all of the power could typically be recovered by fine-tuning the temperature setting of the LBO oven. We theorized that this drift was caused by thermomechanical effects in the commercially-purchased LBO oven assembly. The oven was windowless, so thermal air currents were one source of instability. The cell had a plastic outer sheath that deformed significantly at high temperature, leading to crystal misalignment. Finally, the actual temperature of the LBO crystal underwent small oscillations which were not reflected in the temperature readout of the heating system. We believed that these thermomechanical problems could be minimized or eliminated by the appropriate design of our own heated SHG cell.

We evaluated the KTP SHG crystal in a heated ceramic cell designed at SEO. We found that the SHG output power was highly stable over time, even without windows on the cell. The ceramic sheath and the improved temperature control loop were enough to improve the power stability. Accordingly, we adapted the ceramic SHG cell to the higher temperature required for the LBO crystal, and repeated the LBO SHG experiments using the new cell. We found that the SHG output power was stable as long as the LBO crystal was protected from air currents. Rather than placing windows on the cell, which would have increased the intracavity loss, we built a plexiglass cover for the entire laser. With the cover in place, the SHG output was extremely stable over time, even at the highest output power levels that we obtained.

#### *Intensity Noise Measurements*

High-frequency intensity noise measurements were performed and analyzed under separate funding. For this reason they not included here, but are instead presented in Appendix B of this report (Section 14). A brief summary of the results is given in the following paragraph.

We measured and characterized the high-frequency intensity noise in the fundamental and SHG output beams under various operating conditions. This high-frequency noise is independent of the long-term power stability characteristics discussed above. The laser output displayed chaotic high-frequency intensity noise of varying magnitude, depending on the particular laser configuration. In the worst-case, high-feedback configuration, severe intensity noise values (over 30% rms) were measured over the 0-1 MHz frequency band. In the best-case, low-feedback configuration, the noise was reduced to 2-3% rms over the same frequency band. This is still significant noise, but it should be within acceptable limits for pumping the  $\text{Ti:Al}_2\text{O}_3$  master oscillator in a lidar system. For comparison, a typical Ar-ion laser noise specification is 0.5% rms over the 10 Hz - 2 MHz frequency band.

#### 8.4.4 Analysis of SHG Results

For critically phase-matched (CPM) SHG not limited by walkoff, length of focus, or absorption, the second harmonic power  $P_{2\omega}$  obtained from a fundamental input power  $P_\omega$  is given by [11]:

$$P_{2\omega} = CP_\omega^2 L^2 / w_0^2$$

where  $L$  is the SHG crystal length,  $w_0$  is the beam waist radius inside the crystal, and  $C$  is proportional to the square of the nonlinear optical coefficient  $d_{\text{eff}}$  as shown below:

$$C = [2\mu_0^{3/2} \epsilon_0^{1/2} \omega^2 d_{\text{eff}}^2] / [\pi n_{2\omega} n_\omega^2]$$

For noncritically phase-matched (NCPM) SHG, the optimum second harmonic power is given by:

$$P_{2\omega} = (1.068)CP_\omega^2 L k_\omega$$

where  $k_\omega$  is the wave vector of the fundamental and the other parameters are as defined above.

The CPM formulas apply to the KTP Type II SHG crystal used in our experiments, while the NCPM formulas apply to the LBO Type I crystal. In each case the conversion efficiency improves with longer crystal length, until the practical limits of walkoff, absorption, or reconversion are reached. For the KTP crystal we chose a length of 5 mm, since longer crystals are limited by walkoff. For the LBO crystal we chose a length of 15 mm, since longer crystals are limited by absorption and reconversion.

In these SHG configurations, KTP has a nonlinear optical coefficient  $d_{\text{eff}}$  more than five times greater than that of LBO. Accordingly, despite the longer length and lower refractive index of the LBO crystal, we expected the KTP crystal to perform considerably better than the LBO. Figure 8-29 shows the expected performance of each SHG crystal based on the above formulas. The conversion efficiencies are given with respect to circulating intracavity fluence at the fundamental wavelength. In this approximation, the conversion efficiency is linear when plotted against circulating fluence.

Figure 8-29 also shows experimental data obtained with the KTP and LBO crystals. The fact that the experimental data are not in absolute agreement with the predicted values is not surprising: there is considerable uncertainty in the experimental data due to the difficulty of accurately measuring the circulating intracavity fluence; and the formulas themselves are approximations that do not take into account practical effects such as absorption and

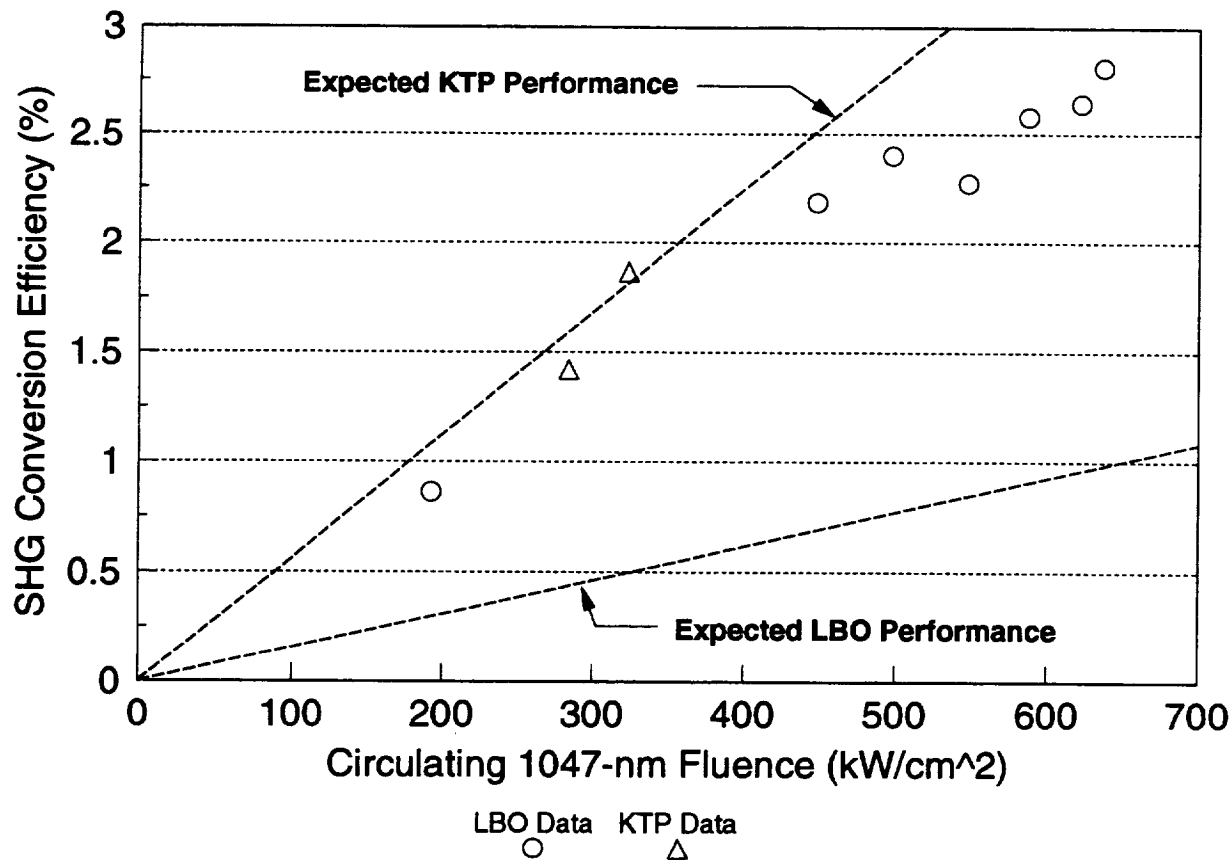


**Figure 8-29.** Expected and measured intracavity SHG conversion efficiencies for KTP and LBO. Conversion efficiencies are given with respect to circulating fundamental intracavity fluence.

depolarization. What is surprising is the performance of LBO relative to KTP in terms of SHG conversion efficiency. The LBO performed about as well as the KTP in practice, even though its performance was expected to be much worse than KTP. Furthermore, use of the LBO allowed us to achieve a higher circulating intracavity fluence in the resonator. This was because the LBO (Type I) crystal did not introduce any depolarization effects. The KTP (Type II) crystal introduced depolarization effects that had to be corrected via temperature-tuning and the addition of a quarter-wave plate. The additional intracavity surfaces, plus the off-normal angle of incidence required for the KTP crystal, limited the intracavity fluence to lower levels than those obtained with the LBO crystal. As a result, more SHG output was obtained with the LBO crystal.

In summary, LBO performed surprisingly well relative to KTP in our intracavity SHG experiments. We obtained similar SHG conversion values from both crystals, and the simplicity of the LBO Type I configuration eliminated the need for polarization correction in the resonator. At this point LBO appears to be a good choice for the intracavity SHG crystal in the cw green laser, with its only disadvantage being the high temperature required for phase-matching (172°C).

### 8.5 Demonstration of an All-Solid-State, CW, $\text{Ti:Al}_2\text{O}_3$ Laser

The best cw, green-laser results were obtained using LBO as the SHG crystal. We obtained greater than 900 mW of cw output power at 523.5 nm with 10 W of diode-laser pump power delivered to the Nd:YLF crystal. We then used the green output to pump a cw, ring  $\text{Ti:Al}_2\text{O}_3$  laser. The  $\text{Ti:Al}_2\text{O}_3$  laser, shown in Figure 8-30, is the proposed master oscillator in the space-based  $\text{Ti:Al}_2\text{O}_3$  lidar system. We obtained up to 16.5 mW of single-frequency, cw output power from the  $\text{Ti:Al}_2\text{O}_3$  laser. The  $\text{Ti:Al}_2\text{O}_3$  laser was tuned over a 120-nm wavelength region from 788 to 908 nm, which was limited on the short-wavelength end by the mirror coatings. (With a "short-band" mirror the laser would have tuned down to about 700 nm). The wavelength-tuning data obtained in this demonstration are shown in Figure 8-31. This experiment demonstrates for the first time, to our knowledge, an all-solid-state, single frequency,  $\text{Ti:Al}_2\text{O}_3$  laser with sufficient output power to injection-seed a high-energy oscillator over a 200-nm bandwidth.

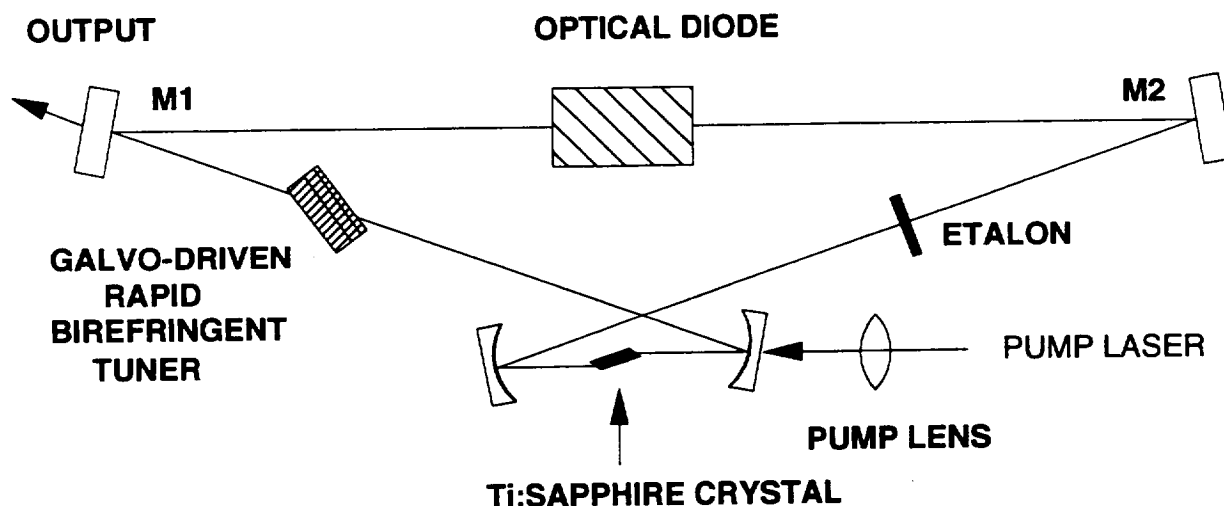


**Figure 8-30.** Layout of the cw, single-frequency, ring,  $\text{Ti:Al}_2\text{O}_3$  laser. This is the master oscillator that was pumped with the cw, green laser developed on this program.

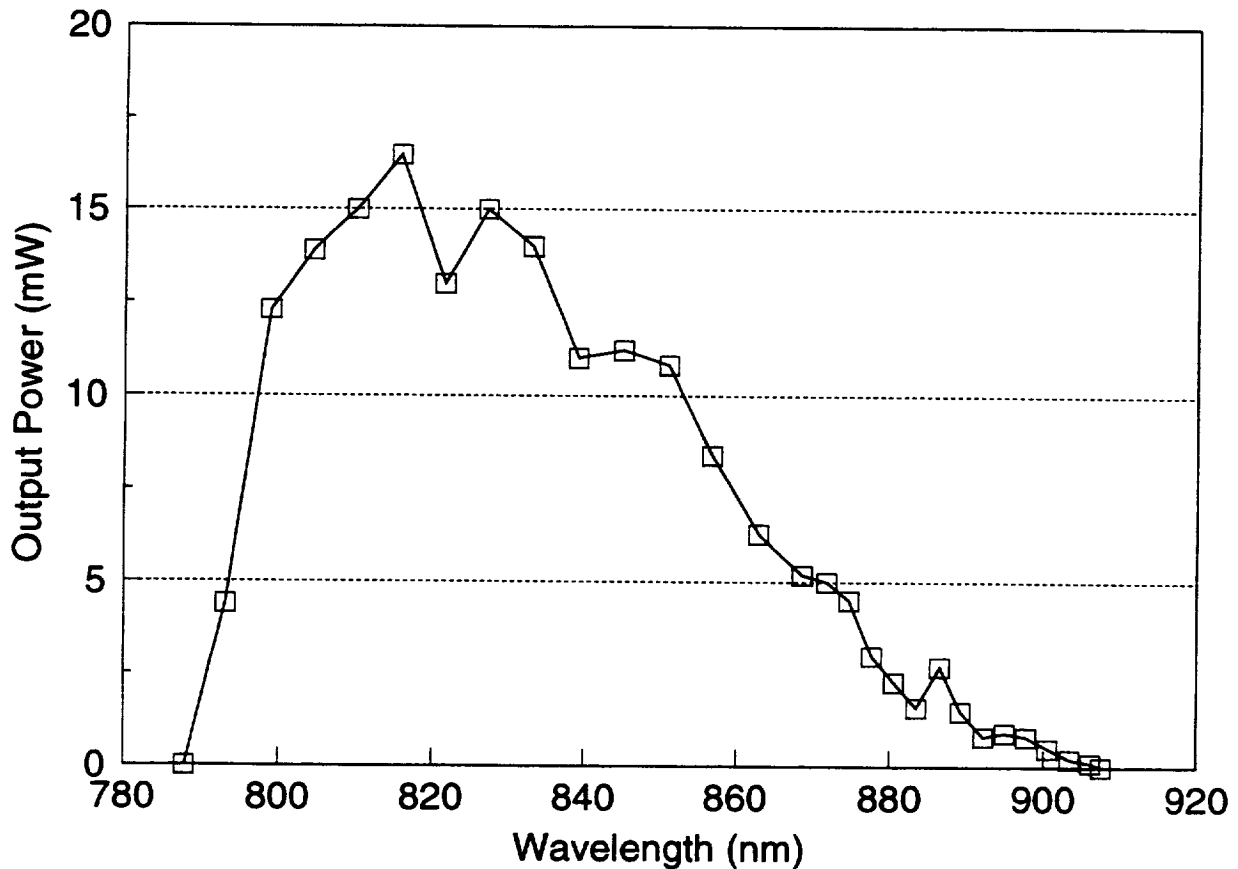


**Figure 8-31.** Wavelength-tuning data for the all-solid-state, master oscillator laser. This is single-frequency output from a cw, ring,  $\text{Ti:Al}_2\text{O}_3$  laser obtained by pumping with the 900-mW, 523.5-nm, Nd:YLF laser described in this report.

## 8.6 Summary of CW Laser Results

The cw, diode-pumped, intracavity-doubled, Nd:YLF laser produced over 900 mW of output at 523.5 nm. This output was used to pump a cw,  $\text{Ti:Al}_2\text{O}_3$ , single-frequency ring laser, thereby demonstrating a tunable, all-solid-state,  $\text{Ti:Al}_2\text{O}_3$  master oscillator. The design of the cw Nd:YLF laser is relatively simple and amenable to compact packaging. There are still some problems that should be addressed further before proceeding with a final opto-mechanical package design. In particular, we need to work on minimizing the intensity noise and improving the thermo-mechanical mounting hardware for the SHG crystal. With these modifications and appropriate packaging, this could be a suitable pump laser for the master oscillator in a space-based  $\text{Ti:Al}_2\text{O}_3$  lidar system.



## 9 Pulsed Laser Development

As stated earlier in this report, the purpose of the slave-oscillator pump laser work was to develop a pulsed, green laser with pulsewidths significantly longer than those produced by conventionally Q-switched, frequency-doubled, Nd lasers. The goal was to increase the reliability of the  $\text{Ti:Al}_2\text{O}_3$  slave oscillator by allowing a greater margin with respect to optical damage limits. The optimum pulsewidth for the gain-switched, unstable-resonator oscillator that is the slave oscillator in our lidar transmitter design [1,2] is on the order of 100 ns.

As with the master-oscillator pump, it will be essential in space-based systems to employ diode-laser pumping for this laser. Therefore, on this project we worked on the development of both diode-laser-pumped oscillator designs and opto-electronics capable of controlling the dynamics of a Q-switched, Nd oscillator.

The details of the diode-laser-pumped oscillator design work are presented in Sections 9.1 through 9.3. The details of the pulsewidth-control work are given in Section 9.4.

### 9.1 Preliminary Design Considerations for the Diode-Laser-Pumped System

As planned, we carried out a design review similar to that done for the cw, green laser. We selected Nd:YAG as the gain medium for the pulsed laser development work, because it has a high stimulated emission cross section and isotropic absorption, which allows simple, efficient operation in the rod geometries that we preferred for this work. Rod geometries provide simple, cylindrically symmetric gain distributions and allow for simple cooling arrangements.

### 9.2 Pulsed Gain Module Design and Construction

The gain module of the pulsed laser consists of four to eight GaAlAs quasi-cw diode laser arrays (each a four-bar stack of linear arrays), reflectors opposite the diode arrays (in some cases), and a side-pumped Nd:YAG rod. The characteristics of the diode laser arrays, and the various pumping configurations investigated, are discussed in the sections below.

#### 9.2.1 Diode Laser Characteristics

A total of nine quasi-cw GaAlAs diode laser arrays, part # SDL-3230-ZHC from SDL, were purchased for use in this program. Eight were used in the laser experiments and one was kept as a spare. Each of the arrays was a four-bar stack of linear arrays with a total peak power output of 240 W. The nominal output wavelength was 808 nm. The diode lasers were driven by four SDL-928 quasi-cw laser drivers (each driving two diode lasers in series). The pulse duration and the repetition rate were variable. We typically operated with a pulse duration of 200  $\mu\text{s}$  and a repetition rate of 25 Hz, for an average power output of 1.2 W (48 mJ/pulse at 25 Hz) per diode laser array. The power output of each array was measured experimentally; all were found to operate as specified.

The diode laser packages were the impingement-cooled type with barbed fittings for water line attachment. This package type was chosen for its great versatility in the laboratory, where it can be easily mounted in different experimental pumping arrangements. (More compact and robust packages are available for applications that require less versatility.) The diode lasers, along with the Nd:YAG laser rod, were cooled in parallel with approximately 20 psi of water pressure across the pump head. Closed-loop water flow was provided by a chiller with variable temperature control.

### **9.2.2 Pumping Configurations**

Two different side-pumping configurations were investigated during the course of the program: a radial pumping arrangement and a linear pumping arrangement. In addition, the use of reflectors to redirect the unabsorbed pump light back into the Nd:YAG rod was investigated. The final pulsed laser configuration included two gain modules, each consisting of a Nd:YAG rod side-pumped by four diode lasers and four reflectors in a linear pumping arrangement. The details of the pumping configurations are presented below; laser performance in the various configurations is discussed in the next section.

The radial pump head configuration is shown in Figure 9-1. The laser rod is a 5-mm diameter by 85-mm long Nd:YAG rod. It is mounted inside a sapphire or quartz flowtube. Eight diode laser arrays are mounted around the rod in a radial side-pumping configuration, with their emitting faces within a millimeter of the flowtube surface. No focusing optics are used, other than the flowtube itself which provides some focusing. This radial pumping scheme is designed to deposit pump energy in a radially symmetric pattern throughout the entire Nd:YAG rod, with the pump energy concentrated in the center of the rod.

The linear pump head configuration is shown in Figure 9-2. The laser rod and flowtube configuration are the same as in the radial pump head. Eight diode laser arrays are mounted alongside the rod, four on each side, in a linear side-pumping configuration. Again, their emitting faces are placed immediately adjacent to the flowtube. This linear pumping scheme is designed to deposit pump energy in a smaller region within the Nd:YAG rod, in order to produce higher gain, at the expense of radial symmetry, as the pump distribution is elliptical.

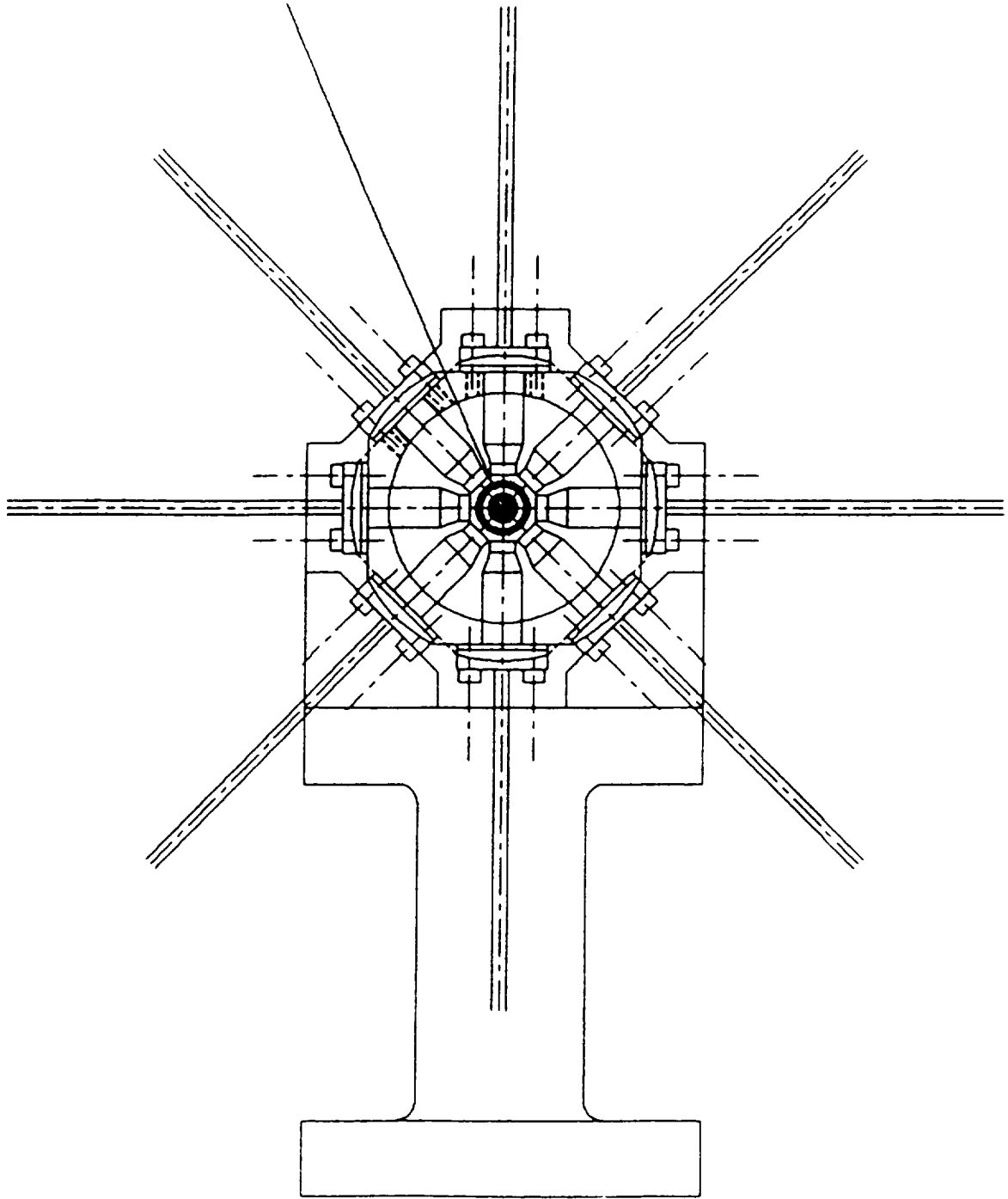


Figure 9-1. Radial pump head configuration for the pulsed diode-pumped Nd:YAG laser.

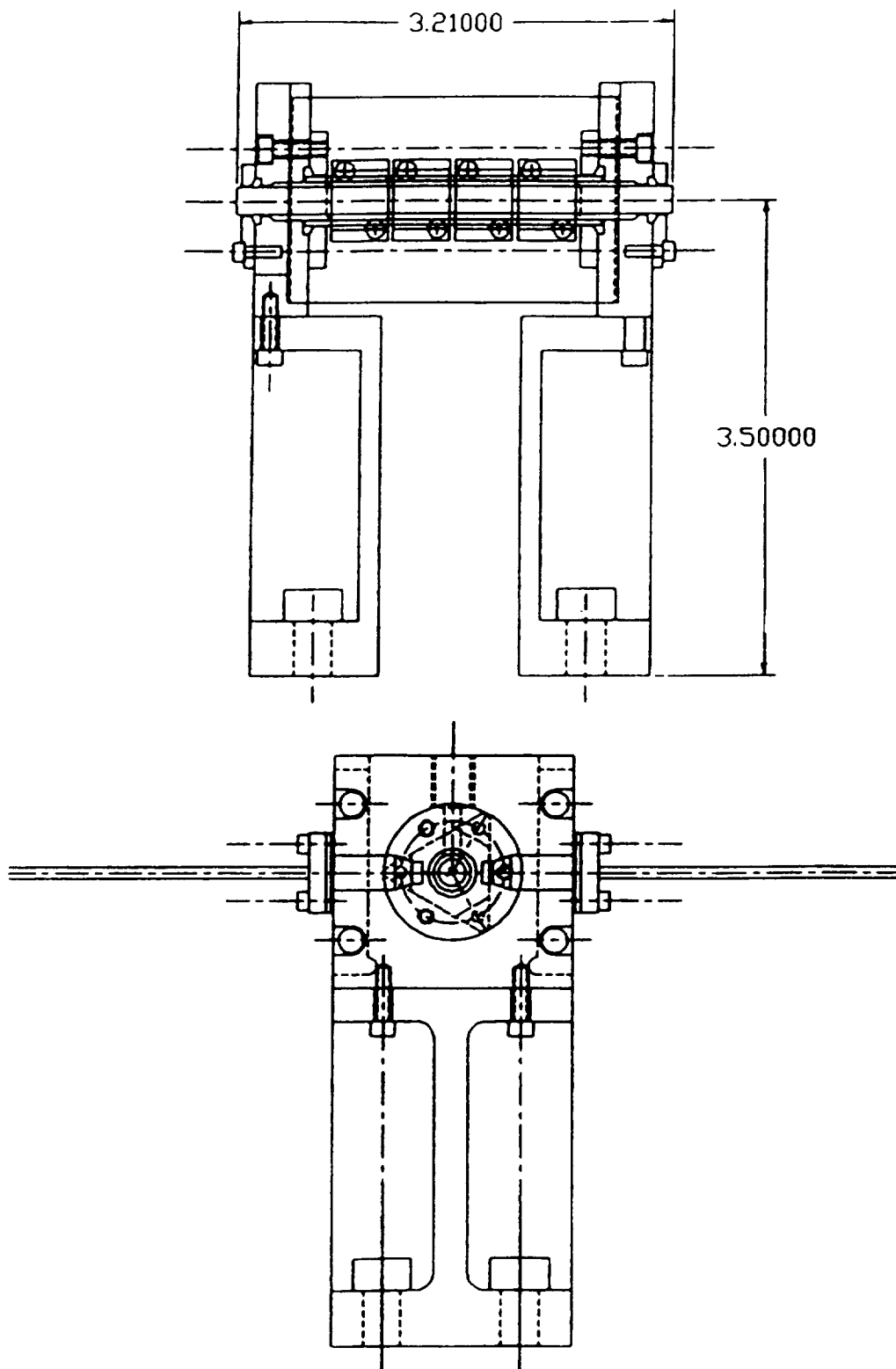


Figure 9-2. Linear pump head configuration for the pulsed diode-pumped Nd:YAG laser.

A small fraction of the pump energy from the diode lasers passes through the Nd:YAG rod unabsorbed. We designed reflectors to redirect this unabsorbed pump light back into the laser rod. The reflectors are made to mount interchangeably with the diode lasers. The reflecting surface is cylindrically concave, with a curvature matching the curvature of the flowtube. The reflectors we initially used to test the concept had gold coatings on a reflective surface of only machined-finish quality. These proved to be highly successful in improving the performance of the laser, so we made a second generation of reflectors with a more durable gold plating on a higher-quality polished reflective surface. As it turned out, the second-generation reflectors did not produce any greater performance improvement than the first generation. They will be more durable in the long run, however.

The reflectors were installed in the linear pump head by simply removing four of the diode lasers and mounting reflectors in their places. (The reflectors were not tried in the radial pump head.) Since this left four diode lasers available, we built a second, identical, linear pump head. In this way we arrived at the final configuration of the pulsed laser: two gain modules, each consisting of a Nd:YAG rod side-pumped by four diode lasers and four reflectors in a linear pumping arrangement.

### **9.3 Laser Performance, Normal-Mode and Conventionally Q-switched**

The diode-pumped pulsed Nd:YAG laser was operated normal-mode in the radial pump head configuration. The pump pulsewidth was 200  $\mu$ s and the pulse repetition rate was 25 Hz. A number of different output couplers were compared. Figure 9-3 shows the normal-mode I/O curves obtained with the various output couplers. The 80%R output coupler produced the best results: at the maximum pump energy of 384 mJ, a normal-mode 1064-nm output energy of 90 mJ was obtained. The normal-mode output beam profile is shown in Figure 9-4.

The laser was then operated with a conventional Q-switch. Figure 9-5 shows the Q-switched I/O data; an output energy of 38 mJ at 25 Hz was obtained using the 80%R output coupler. In going to higher energy while Q-switching, we damaged one face of the Nd:YAG rod. This indicated that in order to avoid damage problems, we would have to use a lower-reflectivity output coupler to reduce the intracavity fluence relative to the output energy. To offset the increase in threshold associated with a lower-reflectivity output coupler, we converted to a linear pumping geometry designed to deposit the pump energy in a smaller cross-sectional area of the Nd:YAG rod.

In the radial pumping geometry, the eight four-bar diode arrays were arranged in a circular pattern around the laser rod. Pump energy was deposited in a roughly circular distribution throughout the entire cross-sectional area of the rod. In the linear pumping geometry, the eight four-bar diode arrays were arranged in two rows on opposite sides of the laser rod. The pump energy was therefore deposited in a smaller, elliptical distribution within the rod. The smaller

pump volume provided higher gain and allowed us to obtain comparable output energies with a lower-reflectivity output coupler. This reduced the likelihood of damage to the laser rod at a given output power level.

The improvement in normal-mode laser performance obtained with the linear pumping geometry is shown in Figure 9-6. These results are for a single pump head, which accommodates eight diode lasers in the radial case and four in the linear case. The linear pumping geometry produces more output power for a given pump energy. Results are also shown for the linear pump head with reflectors installed as described in Section 9.2.2. A 13% improvement in performance was observed with the reflectors at the 200-mJ pump level.

During the course of these experiments we made a comparison between sapphire flowtubes and quartz flowtubes. We expected that the sapphire flowtube might produce slightly better results, since its higher index of refraction would assist in focusing the pump energy in the laser rod. However, no significant difference in overall laser performance was observed.

We built a second linear pump head, identical to the first (including reflectors), and installed it in the resonator. In this configuration the laser included two gain modules, each consisting of a Nd:YAG rod side-pumped by four diode lasers and four reflectors in a linear pumping geometry. A 1064-nm, normal-mode I/O for the reconfigured laser is plotted in Figure 9-7. In the new configuration, the maximum output energy increased from 90 mJ to 101 mJ with the 80%R output coupler, and from 77 mJ to 92 mJ with the 60%R output coupler. Therefore, in the reconfigured laser, we were able to maintain the same output energy while reducing the output coupler reflectivity from 80% to 60%.

Due to the linear pumping geometry, the laser output beam was roughly elliptical. A normal-mode profile of the beam appears in Figure 9-8. We had originally planned to use intracavity anamorphic prisms to compensate for the ellipticity; however, we decided to proceed with a porro-prism resonator design for the laser instead.

The porro resonator that was evaluated experimentally is shown in Figure 9-9. This resonator design has some merit and may be considered in future work, however, we not satisfied with the spatial mode quality that it produced with the linear pump head.

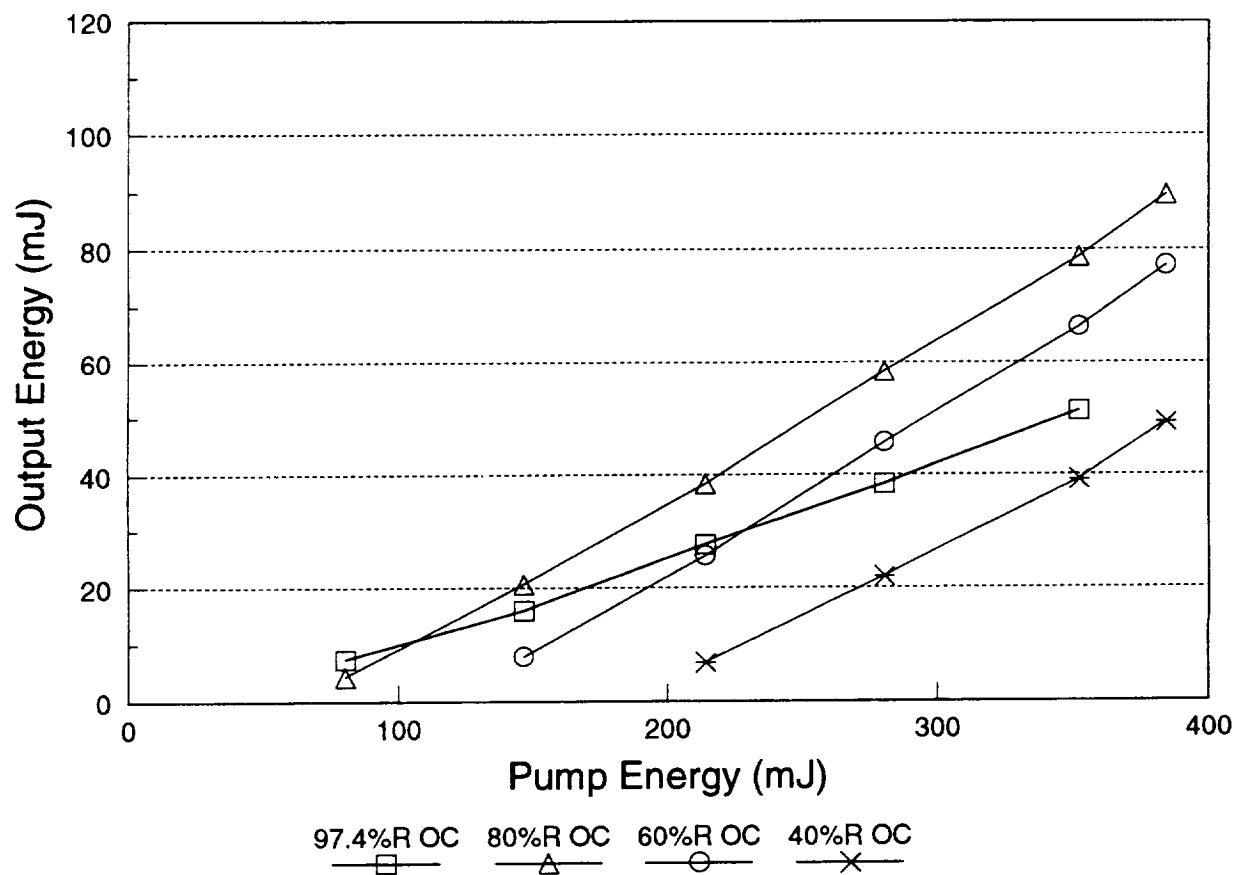


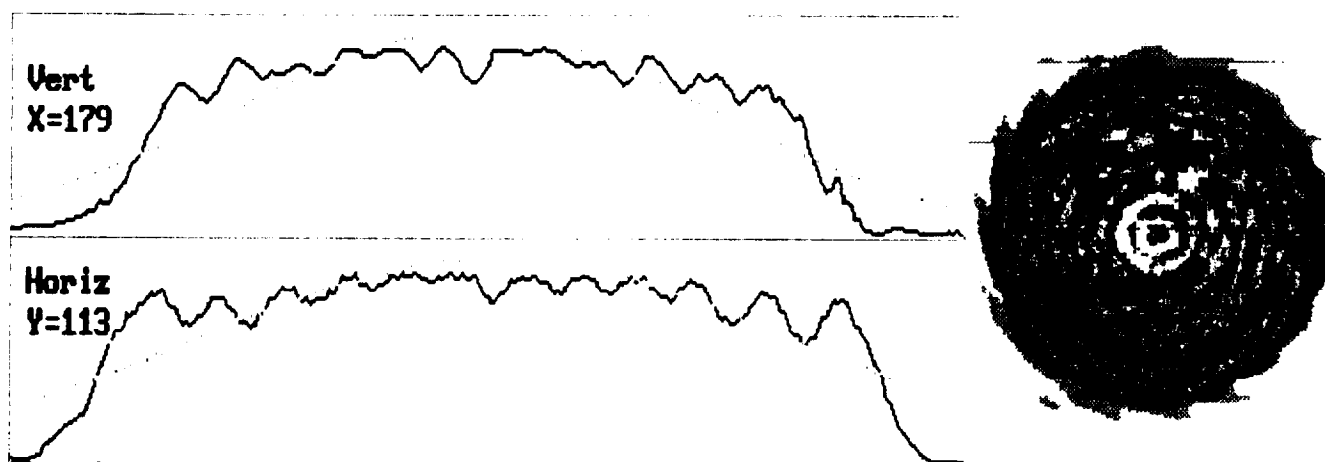
**Figure 9-3.** Normal-mode 1064-nm pulsed laser I/O data, radial pump head configuration with various output couplers.



(Gaussian Fit Data)		
	Vert	Horiz
Correlation Coeff.	= 0.727	0.689
Peak Position	= 115	181
Beam Dia. @ 1/e <sup>2</sup> [mm]	= 6.617	6.908
Percent of Peak	= 97.844	96.114

(Cursor Location)	
<b>CENTROID</b>	
(X,Y) = (179,113)	
Profile Location	
X (Vert)	= 179
Y (Horiz)	= 113

Active Cursor: Contour

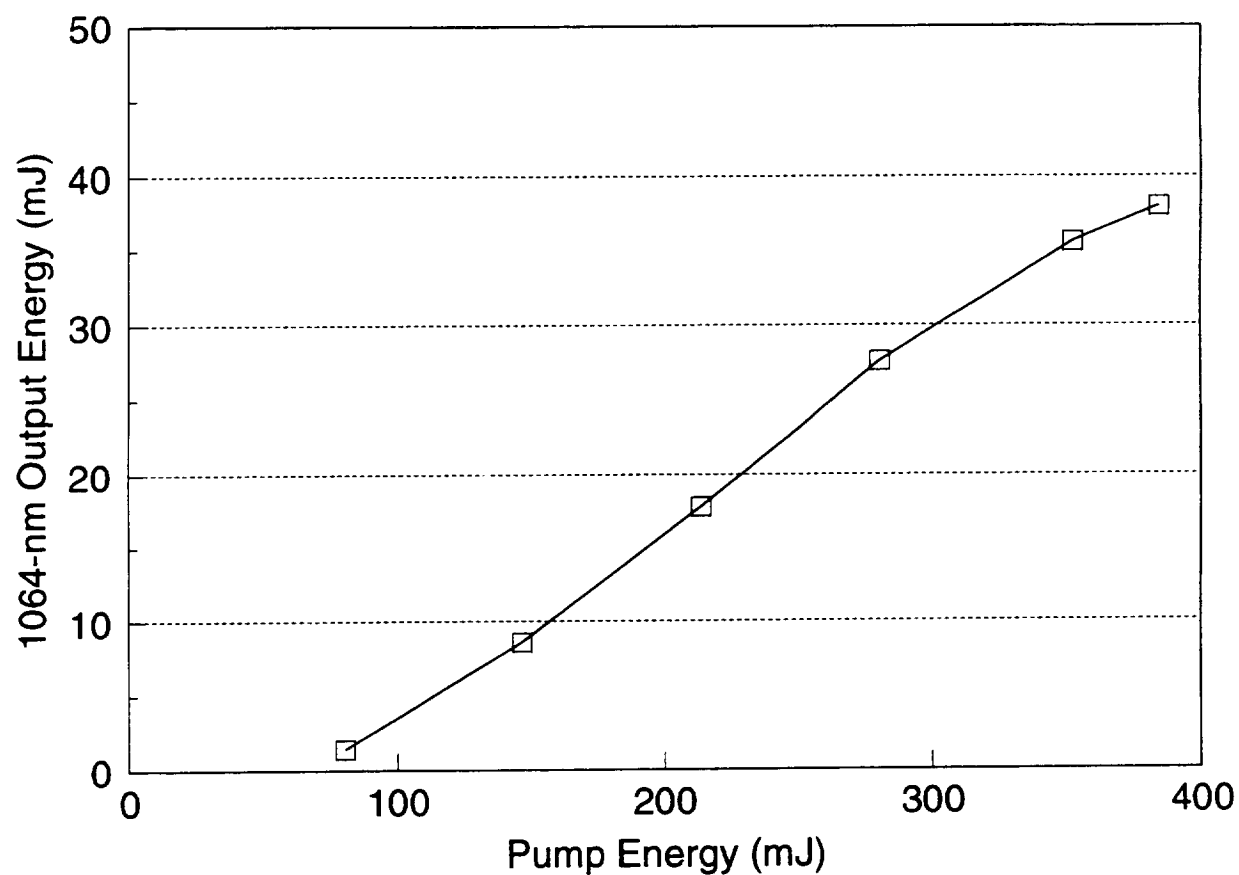


LEFT MOUSE BUTTON draws profile.

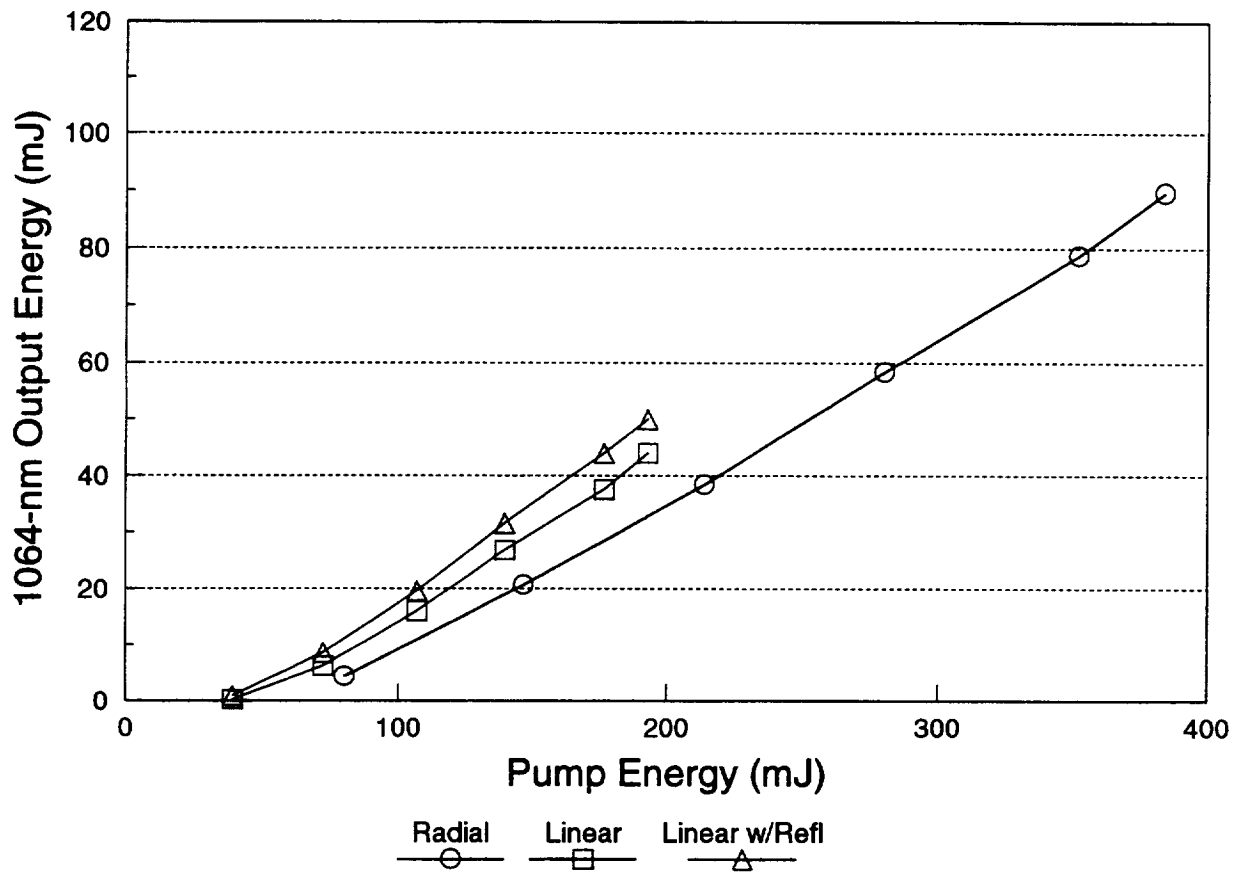
Press <ESC> to abort printing.

Figure 9-4. Normal-mode output beam profile from the diode-pumped pulsed Nd:YAG laser, radial pump head configuration.





**Figure 9-5.** Q-switched 1064-nm pulsed laser I/O data, radial pump head configuration with 80%R output coupler.



**Figure 9-6.** Normal-mode 1064-nm pulsed laser I/O data with 80%R OC: radial pump head, single linear pump head, single linear pump head with reflectors.

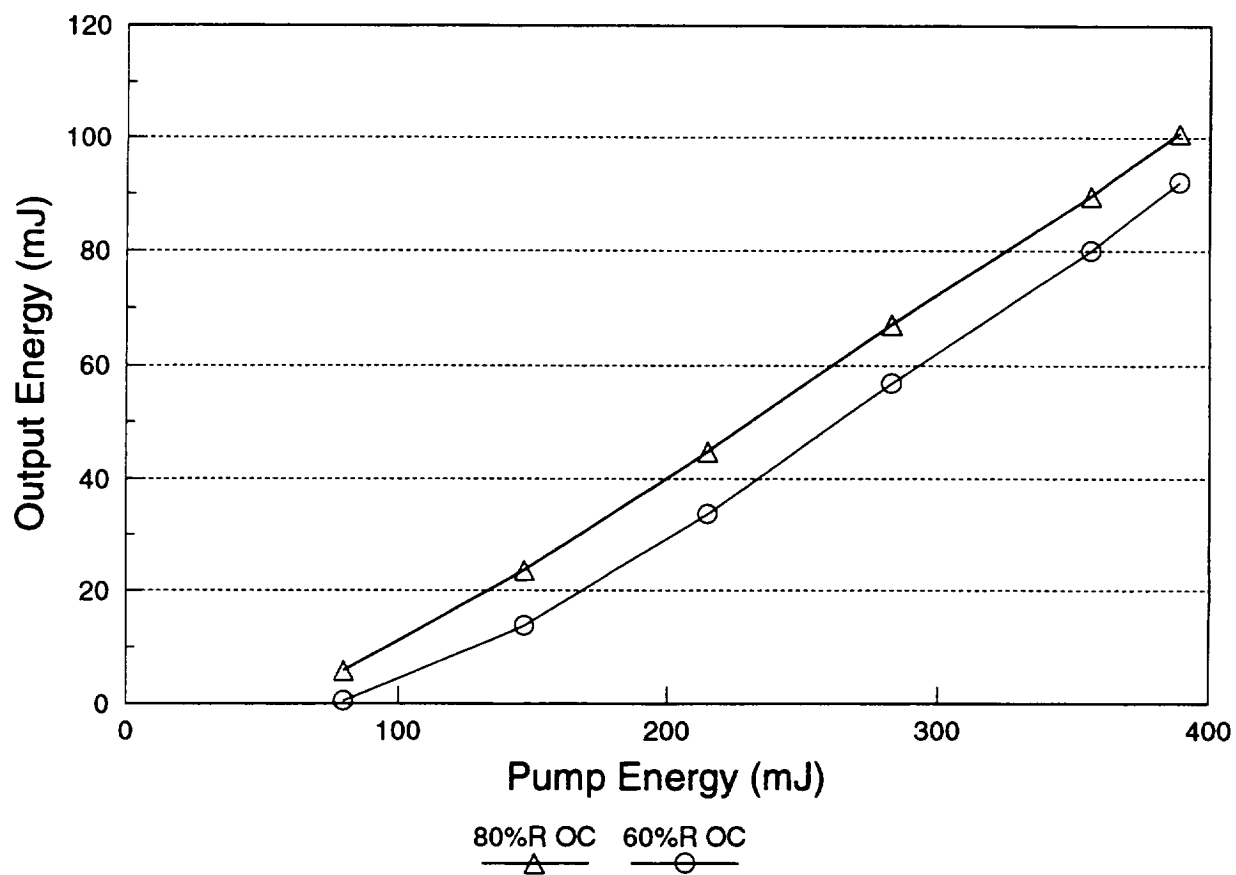
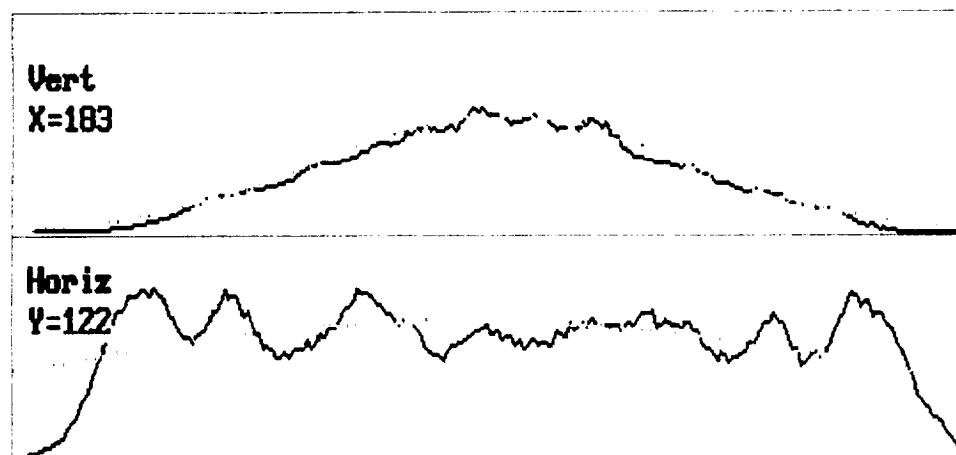


**Figure 9-7.** Normal-mode 1064-nm pulsed laser I/O data, 80%R and 60%R output couplers, two-linear-pump-head configuration with reflectors.

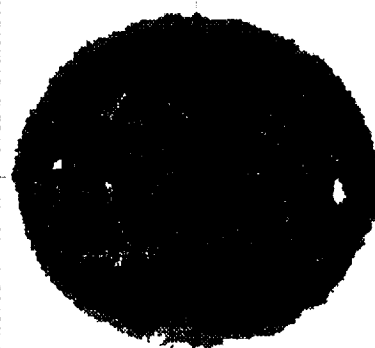
(Gaussian Fit Data)		
	Vert	Horiz
Correlation Coeff.	= 0.947	0.660
Peak Position	= 122	172
Beam Dia. @ $1/e^2$ [mm]	= 4.915	10.980
Percent of Peak	= 56.251	65.714

Cursor Location	
<b>CENTROID</b>	
(X,Y) = (183,122)	
Pixel Location	
X (Vert)	= 183
Y (Horiz)	= 122

Active Cursor: Contour



LEFT MOUSE BUTTON draws profile.



Press <ESC> to abort printing.

Figure 9-8. Normal-mode output beam profile from the diode-pumped pulsed Nd:YAG laser, linear pump head configuration.

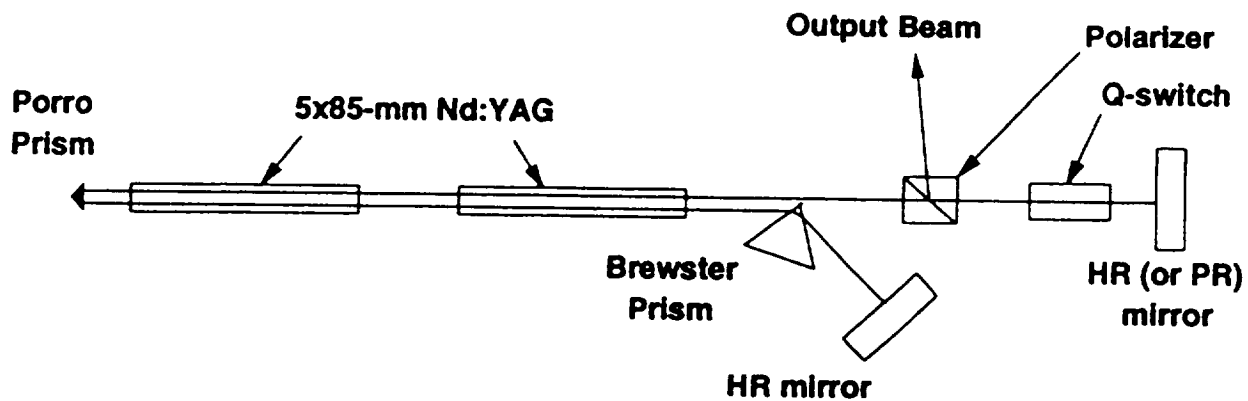


**Figure 9-9.** Optical schematic of the porro-prism resonator used with the two-linear-pump-head configuration.

## 9.4 Actively Controlled Q-switch Development

The development of the controlled opening Q-switch followed closely the work of Schmid [12]. The critical design-verification experiment that we carried out was configured as follows. We installed a lithium niobate Q-switch in a polarization-coupled Nd:YAG laser excited by a linear flashlamp. The laser resonator was formed by two HR mirrors spaced 80 cm apart. Figure 9-10 is a block diagram of the Q-switch electronics. The HV supply was adjusted to the 1/4-wave voltage for maximum hold-off, 1140 V. The Eimac Y-483 planar triode is used to control the voltage across the Q-switch during pulse build-up and extraction. The triode cath-

ode is held at a positive voltage, keeping the tube completely off, during the lamp pulse, and is switched to ground potential with a fast FET to initiate laser pulse buildup. The Q-switch voltage with the cathode grounded is determined by the grid voltage, which is controlled by the LeCroy 9101 arbitrary function generator (AFG), amplified by a factor of three. The composite amplifier consists of a ComLinear CLC231 operational amplifier followed by an Apex WB05 buffer, and provides an inverting gain of three up to 100 MHz, with over one ampere of output current. The grid voltage is held at -6 V while the cathode is switched to ground, which produces a Q-switch voltage of 940 V, corresponding to approximately 20% feedback to the laser cavity.

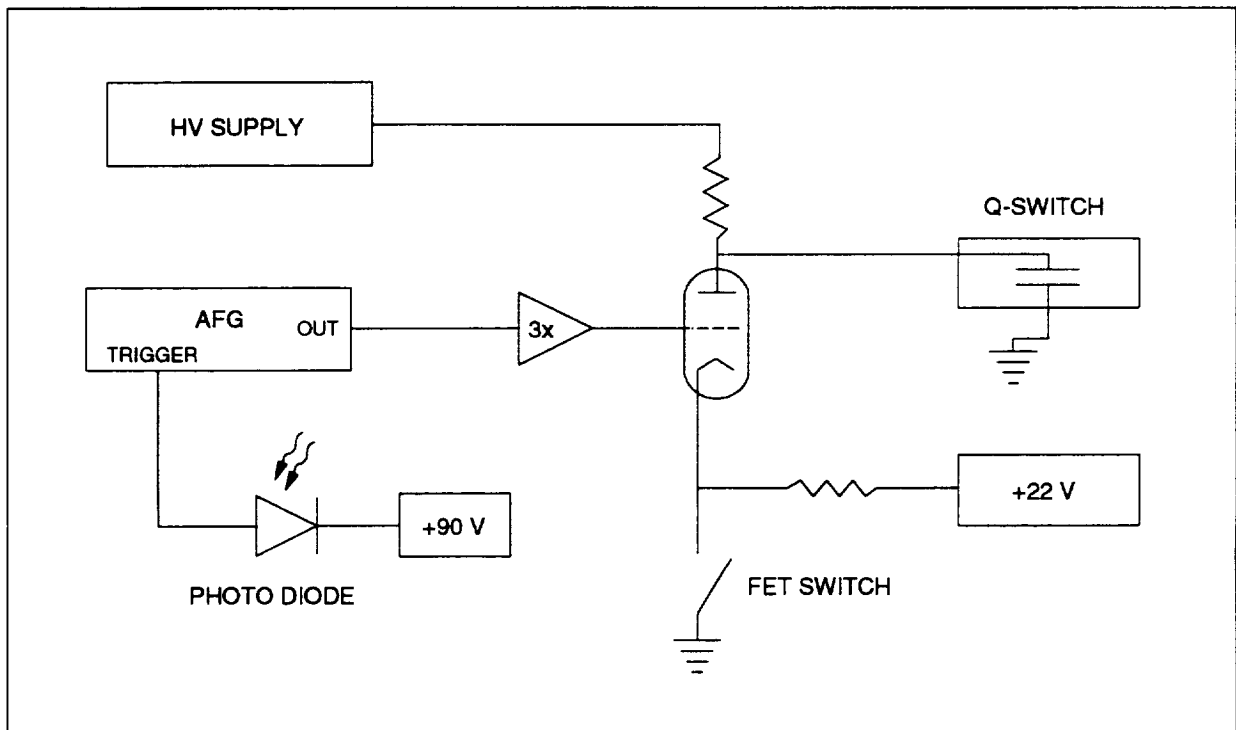


**Figure 9-10.** Block diagram of the controlled-opening Q-switch electronics.

Figure 9-11 shows the Q-switch voltage and the resulting laser pulse for this base line case where the Q-switch goes from hold-off to a fixed outcoupling. (This is essentially "conventional" Q-switching done with the ACQS circuitry). A narrow pulse approximately 50 ns wide is emitted several hundred ns after the Q-switch is opened. As shown in Figure 9-11, a second pulse was often detected close to 1  $\mu$ s after the first pulse. Figure 9-12 presents three traces on a shorter time scale with the digitizer triggered by the laser pulse. The average energy output under these conditions was 20 mJ.

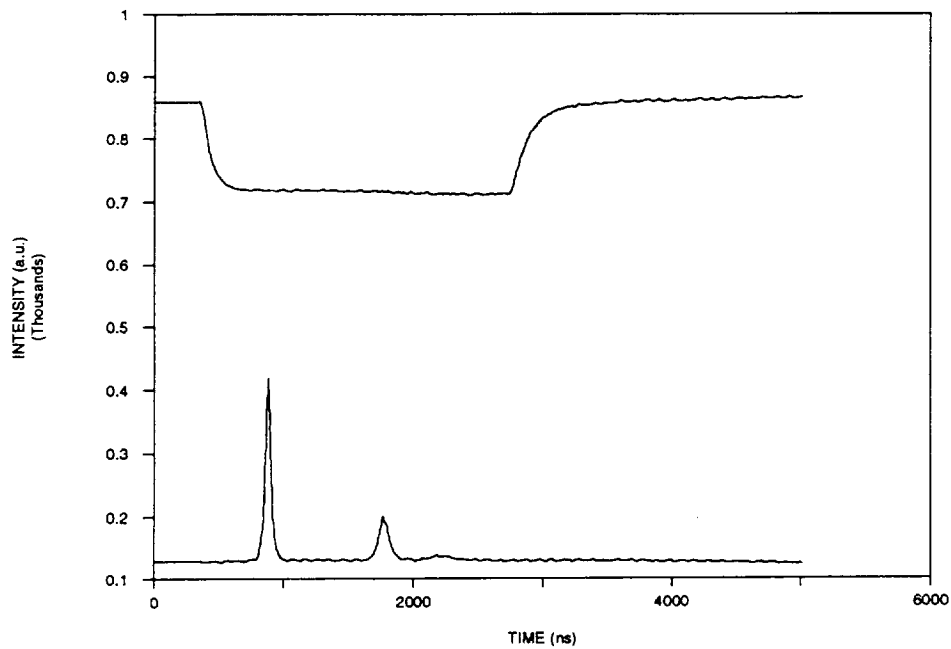


**Figure 9-11.** Q-switch voltage (upper trace) and laser output under the baseline, constant out-coupling conditions.

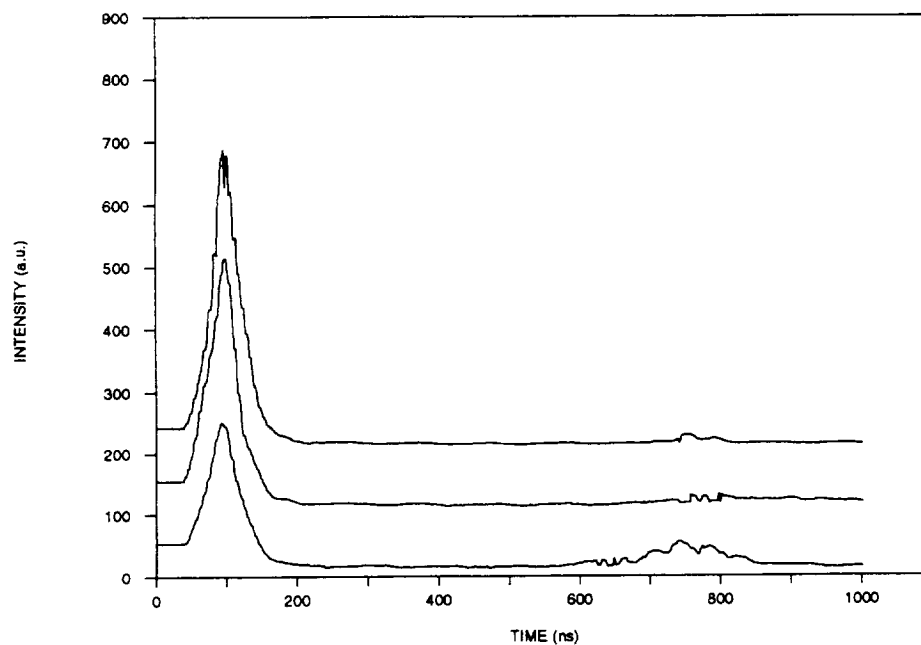


**Figure 9-12.** Three traces collected under the baseline conditions.

We then attempted to smoothly control the Q-switch voltage in order to maintain laser action and extract a larger fraction of the 80-mJ stored energy. We quickly found that the build-up time jitter was sufficiently large, several hundred ns, that the AFG needed to be triggered by the laser pulse itself. Early results are shown in Figure 9-13, where the lower trace corresponds to 30 mJ of output generated with a slowly changing grid voltage from the AFG, while the middle trace corresponding to 47 mJ, and the upper trace to 55 mJ were generated with step changes on the grid. Figures 9-14 and 9-15 present Q-switch and laser pulse waveforms at 30 mJ and 50-55 mJ outputs respectively generated with step changes of about 9 V and 20 V on the grid. In these figures the two traces were collected from different laser firings so the time registration is only approximate. Clearly the varying Q-switch voltage is having an effect, but the AFG needed to be triggered earlier. Note from Figures 9-14 and 9-15 that the Q-switch voltage responds nearly exponentially to sudden changes in grid voltage.

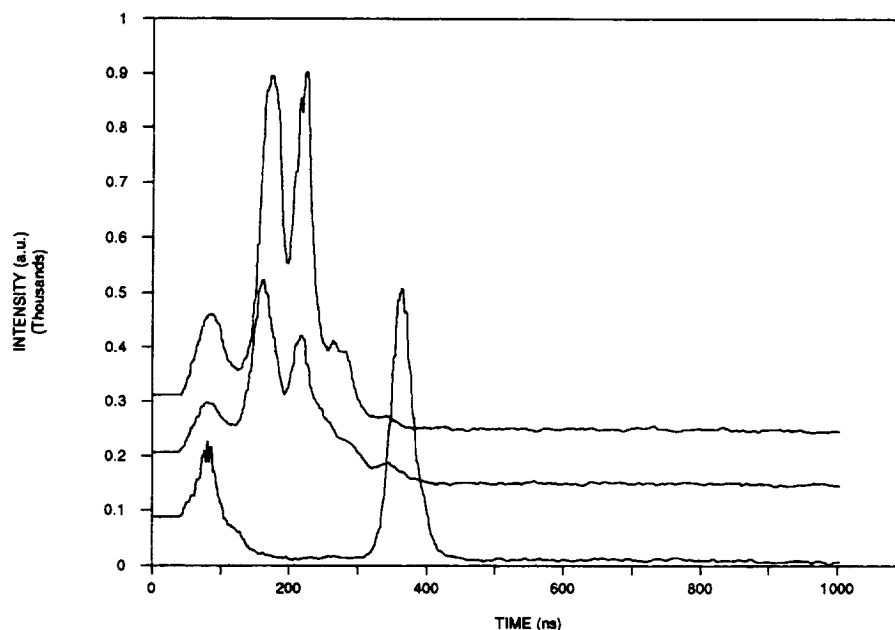


**Figure 9-13.** Three laser pulses corresponding to 30 mJ of output for the lower trace, 47 mJ for the middle trace, and 55 mJ for the upper trace.



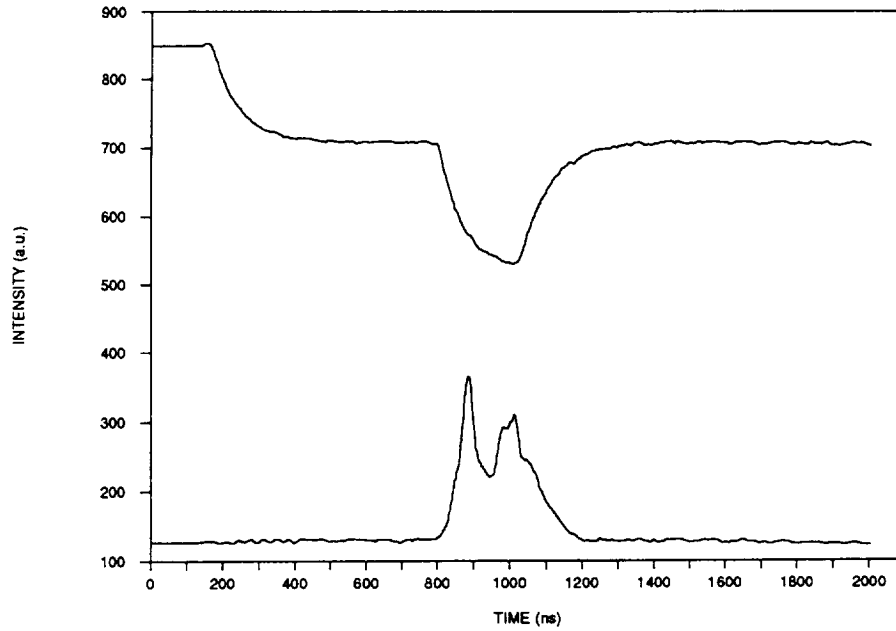


**Figure 9-14.** Q-switch voltage and laser pulse corresponding to 30 mJ of output resulting from a 9-V step to the grid.

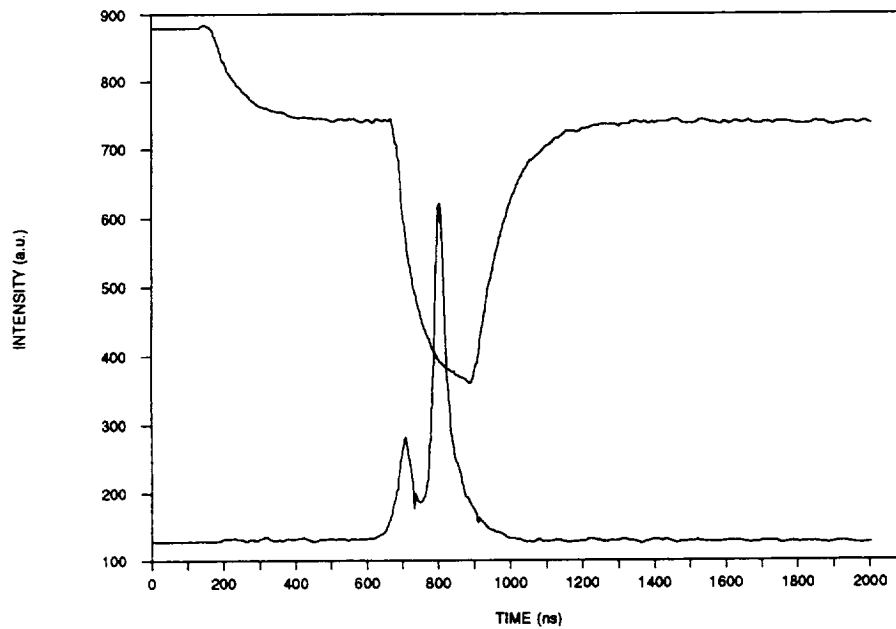


**Figure 9-15.** Q-switch voltage and laser pulse corresponding to 50-55 mJ of output resulting from a 20-V step to the grid.

Figures 9-16 through 9-18 illustrate the effect of changing the AFG trigger point relative to the developing laser pulse. Approximately 50 mJ was produced in each case by driving the grid with a 15-V step. In Figure 9-16 the AFG was triggered relatively late, so that the initial 20-mJ pulse had decayed almost to zero by the time the dropping Q-switch voltage began to couple-out an additional 30 mJ. In Figure 9-17, the AFG was triggered very early in the developing pulse, and a single, narrow emission was the result. For Figure 9-18, the AFG trigger point was adjusted to produce the most uniform pulse. The resulting 48-mJ pulse had a FWHM of about 150 ns. The high frequency fluctuations are due to mode-beating, and the lower frequency fluctuations are probably due to competition between spatial modes.

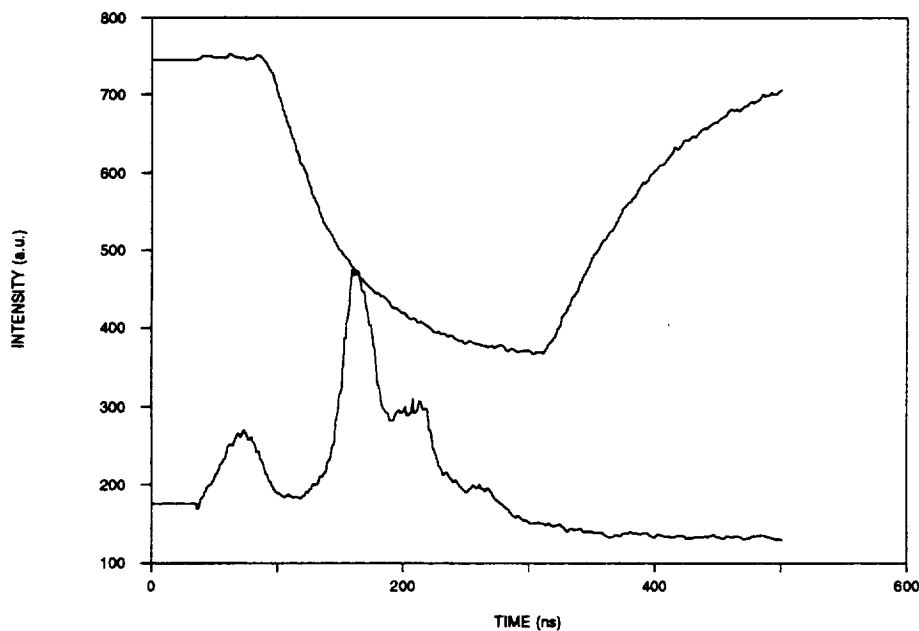


**Figure 9-16.** Q-switch voltage waveform and laser pulse with the AFG triggered late.

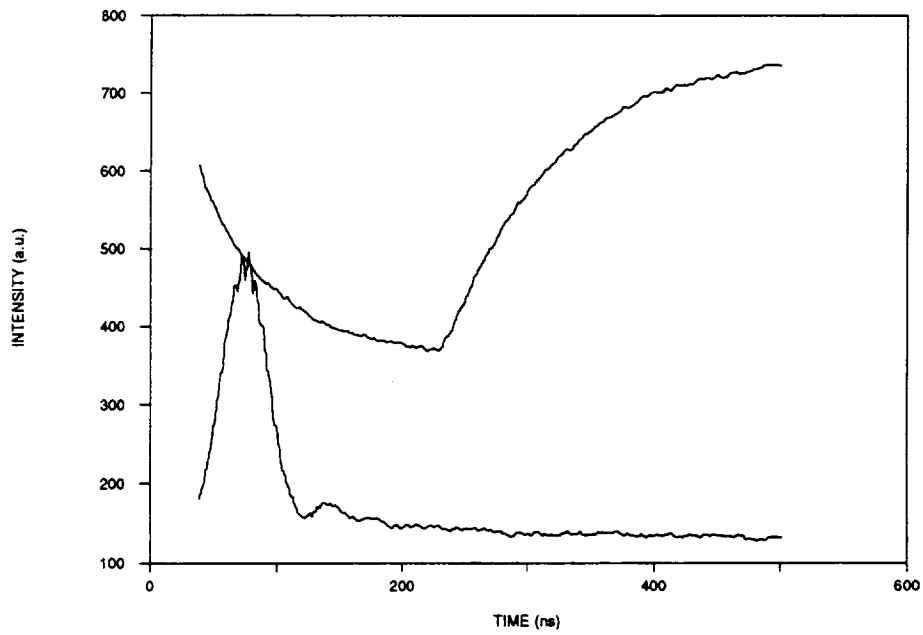


**Figure 9-17.** Q-switch voltage waveform and laser pulse with the AFG triggered early.

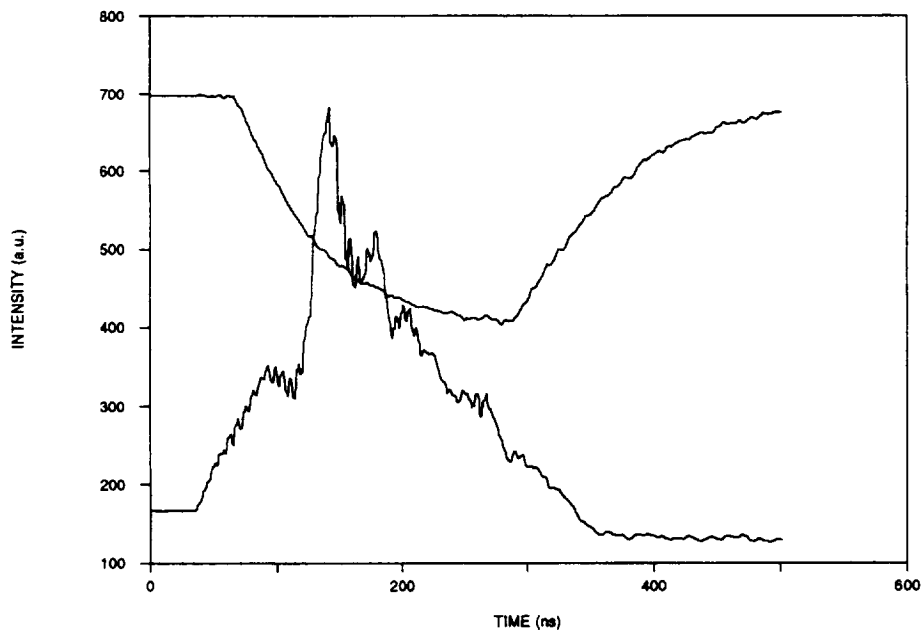


**Figure 9-18.** Q-switch voltage waveform and laser pulse with the AFG trigger optimized for pulse uniformity.

We next tried to reduce the spike near the leading edge of the pulse by modifying the grid drive from the AFG. Figure 9-19 shows the result of using a double step function, where the grid was first stepped up by 9 V for 125 ns, then by another 6 V to 15 V for 125 ns. Now the spike occurred at the trailing edge. Note the cusp in the Q-switch voltage waveform. Figure 9-20 was generated by first driving the grid with a 12-V step, then with another 3 V. The pulse energy was 46 mJ and the FWHM was about 250 ns. When we increased the magnitude of the grid drive the pulse energy increased but it also became more unstable. Figures 9-21 and 9-22 illustrate this tendency at pulse energies of 55 mJ and 57 mJ, respectively. Figure 9-22 shows that the instability was not reproducible pulse-to-pulse, with some pulses having quite large peak intensities. Although in theory active feedback could be applied to the grid in an attempt to suppress these fluctuations, a more efficient approach would be to first improve the passive stability of the laser.

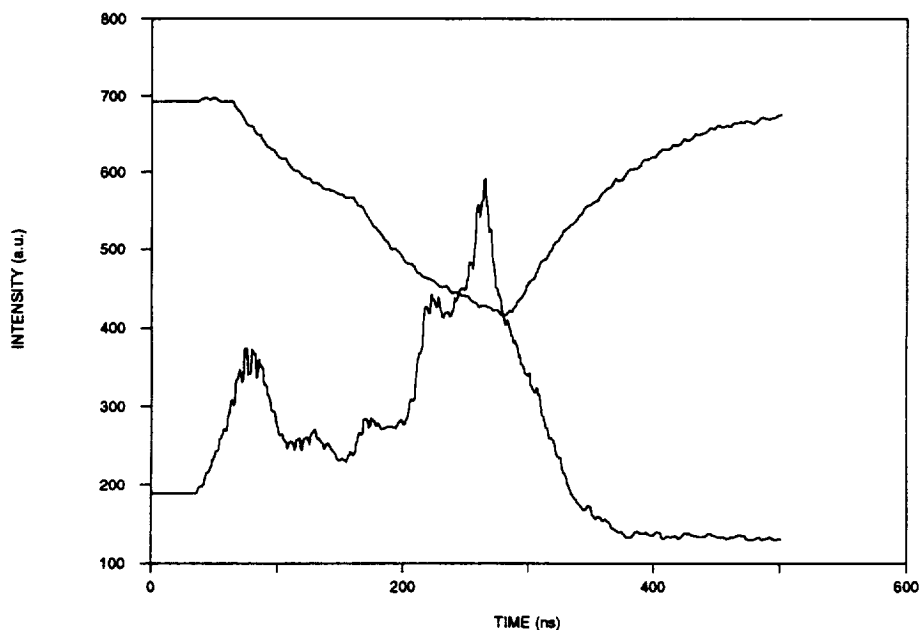


**Figure 9-19.** Q-switch voltage waveform and laser pulse with the AFG driving the grid with a 9-V then 6-V double-step.

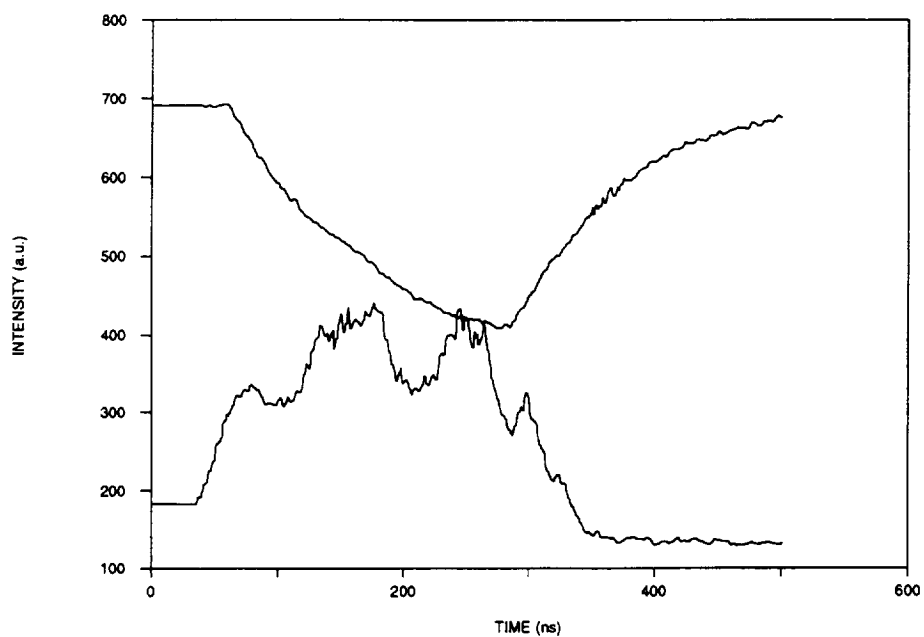


**Figure 9-20.** Q-switch voltage waveform and laser pulse with the AFG driving the grid with a 12-V then 3-V double-step.

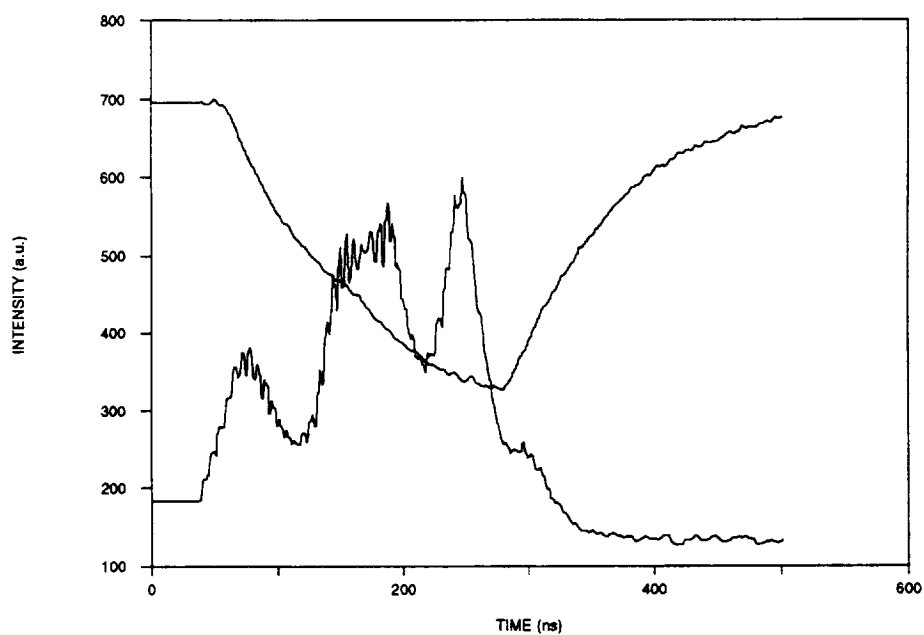


**Figure 9-21.** Q-switch voltage waveform and laser pulse with the AFG driving the grid with a 16-V then 4-V double-step.

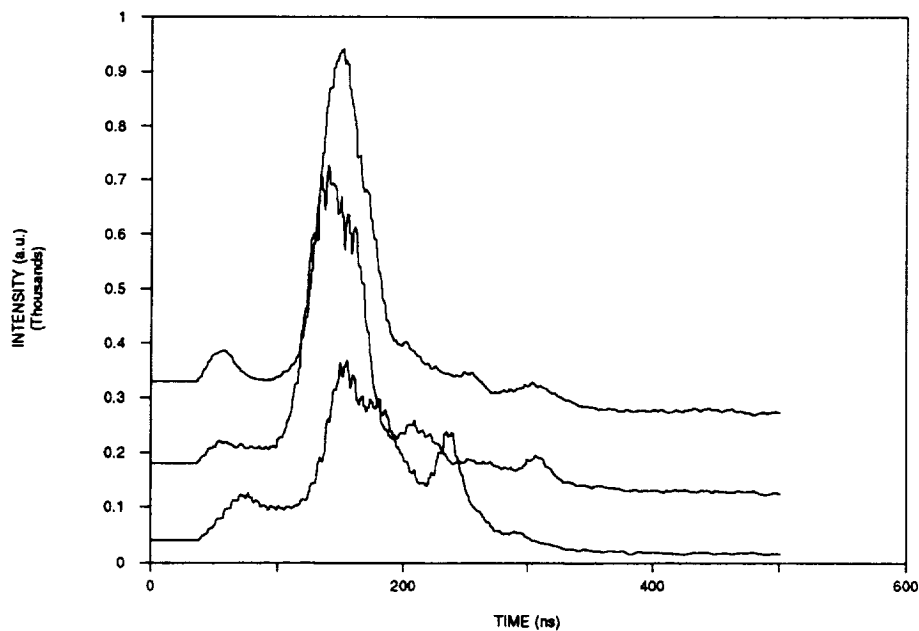


**Figure 9-22.** Three laser pulses generated under similar conditions showing the pulse-to-pulse variability prevalent at 57 mJ.

## 9.5 Summary of Pulsed Laser Results

In the course of the diode-laser-pumped work we designed, fabricated, and tested two side-pumping configurations: a "radial" pump head and a "linear" pump head. Nd:YAG in a rod geometry was selected as the gain medium for the reasons given in Section 6. The radial and linear heads were evaluated in terms of gain distribution, normal-mode and Q-switched operation. We obtained up to 90 mJ of output energy from the radial head in normal-mode operation and 40 mJ with "conventional" Q-switching (low-order, multi-transverse-mode). The total diode-laser pump energy was 350 mJ, hence the overall optical conversion efficiency was 26 % for normal-mode operation and 11 % for Q-switched operation.

The actively-controlled Q-switching (ACQS) effort was carried out using a flashlamp-pumped, Nd:YAG test bed. This was to allow maximum flexibility in the ACQS effort and to allow the diode-laser-pumped work to go on in parallel with and independent of the ACQS work. The intent was to integrate the ACQS hardware into the diode-laser-pumped oscillator at the end of the ACQS effort. We were not able to carry out this integration step within the time frame of the Phase II program. This is the next logical step in the development effort, which could be carried out in a Phase III effort at SEO or by NASA researchers.

The ACQS experiments succeeded in demonstrating pulse-stretching in a Q-switched Nd:YAG oscillator. We obtained greater than 50-mJ pulse energies in pulses with 100- to 200-ns pulsewidths (FWHM). This is suitable for use in a Nd:YAG amplifier chain for the generation of Joule-level output energies that are subsequently converted to the green region via SHG.

## 10 Summary and Conclusions

To summarize, the program succeeded in demonstrating, in laboratory laser experiments, the technical goals of the program: 1) an all-solid-state, broadly tunable, single-frequency, Ti:Al<sub>2</sub>O<sub>3</sub> master oscillator, and 2) a technique for obtaining "long" (nominally 100- to 200-ns FWHM) laser pulses from a Q-switched, Nd oscillator at energy levels commensurate with straightforward amplification to the Joule level.

In keeping with one of the overall SBIR program objectives, SEO intends to continue the development of these lasers beyond the now completed Phase II contract, and to ultimately produce commercial lasers either as scientific laser products or as components of more sophisticated laser systems such as differential absorption lidar (DIAL) systems.

## 11 References

1. G.A. Rines, J. Harrison, and P.F. Moulton, "Narrowband high-energy titanium doped sapphire lidar transmitter for spacecraft remote sensing," Final Technical Report, NASA Contract# NAS1-18457, November 1990.
2. G.A. Rines, P.F. Moulton, and J. Harrison, "Narrowband, High-Energy Ti:Al<sub>2</sub>O<sub>3</sub> Lidar Transmitter for Spacecraft Sensing," *Proceedings of the Tunable Solid-State Lasers Topical Meeting, Optical Society of America*, 1989.
3. J.L. Emmett, W.F. Krupke and J.B. Trenholme, "Future development of high-power solid-state laser systems," *Sov. J. Quantum Electron.*, **13**, pp.1-23, 1984.
4. G.A. Rines and P.F. Moulton, "Performance of gain-switched Ti:Al<sub>2</sub>O<sub>3</sub> unstable-resonator lasers," *Opt. Lett.*, **15**, pp. 434-436, 1990.
5. G.A. Rines and P.F. Moulton, "Performance of gain-switched Ti:Al<sub>2</sub>O<sub>3</sub> unstable-resonator lasers," presented at the *Optical Society of America Topical Meeting on Advanced Solid-State Lasers* in Salt Lake City, UT, 5-7 March 1990 (paper MC1).
6. Steve Tidwell, Jon F. Seamans and Dennis Lowenthal, "Lens array coupling of 10-W diode bars for cw end pumping," presented at the *1991 Annual Meeting of the Optical Society of America* in San Jose, CA, 3-8 November 1990.
7. D.C. Shannon and R.W. Wallace, "High-power, Nd:YAG laser end pumped by a cw, 10 mm x 1µm aperture, 10-W laser-diode bar," *Opt. Lett.*, **16**, pp. 318-320, 1991.

8. C.F. Rae, J.A.C. Terry, B.D. Sinclair, M.H. Dunn, and W. Sibbett, "Single-frequency, end-pumped Nd:YLF laser excited by a 12-mJ diode-laser array," *Opt. Lett.*, **17**, pp. 1673-1675, 1992.
9. J.E. Murray, "Pulsed Gain and Thermal Lensing of Nd:LiYF<sub>4</sub>," *IEEE J. Quantum Electron.*, **QE-19**, pp. 488-491, 1983.
10. H. Vanherzeele, "Optimization of a cw mode-locked frequency-doubled Nd:LiYF<sub>4</sub> laser," *Appl. Opt.*, **27**, pp. 3608-3615, 1988.
11. *CRC Handbook of Lasers with Selected Data on Optical Technology*, ed. R.J. Pressley, pp. 493-496, publ. by The Chemical Rubber Co., Cleveland, OH, 1971.
12. W. E. Schmid, "Pulse Stretching in a Q-Switched Nd:YAG Laser," *IEEE J. Quantum Electron.*, **QE-16**, pp. 790-794, 1980.
13. T. Baer, "Large-amplitude fluctuations due to longitudinal mode coupling in diode-pumped intracavity-doubled Nd:YAG lasers," *J. Opt. Soc. Am. B*, **3**, pp. 1175-1180, 1986.
14. G.E. James, E.M. Harrell II, and R. Roy, "Intermittency and chaos in intracavity doubled lasers," *Physical Review A*, **41**, pp. 2778-2790, 1990.
15. D.W. Anton, D.L. Sipes, T.J. Pier, and M.R. Ressler, "Intracavity Doubling of CW Diode-Pumped Nd:YAG Lasers with KTP," *IEEE J. Quantum Electron.*, **28**, pp. 1148-1157, 1992.
16. H. Nagai, M. Kume, I. Ohta, H. Shimizu, and M. Kazumura, "Low-Noise Operation of a Diode-Pumped Intracavity-Doubled Nd:YAG Laser Using a Brewster Plate," *IEEE J. Quantum Electron.*, **28**, pp. 1164-1168, 1992.
17. G. Cerullo, S. De Silvestri, V. Magni, O. Svelto, and L.J. Qian, "13.5 W cw TEM<sub>00</sub> green beam by intracavity frequency doubling of a Nd:YLF laser," presented at the *1993 Conference on Lasers and Electro-Optics* in Baltimore, MD, 2-7 May 1993 (paper CWD7).



## 12 List of Acronyms and Abbreviations

ACQS	actively controlled Q-switch
AFG	arbitrary function generator
AOA	Adaptive Optics Associates
Ar	argon
AR	anti-reflection
CPM	critical phase-matching
CW	continuous wave
DIAL	differential absorption lidar
FFT	fast Fourier transform
FWHM	full width half maximum
GaAlAs	gallium aluminum arsenide
GGG	gadolinium gallium garnet
HR	high reflector
KTP	potassium titanyl phosphate
LaRC	Langley Research Center (NASA)
LBO	lithium triborate
NASA	National Aeronautics and Space Administration
NCPM	non-critical phase-matching
Nd:YAG	neodymium-doped, yttrium aluminum garnet
Nd:YLF	neodymium-doped, yttrium lithium fluoride
OPC	Opto-Power Corporation
PR	partial reflector
RIN	relative intensity noise
rms	root mean square
RTV	room temperature vulcanization
SBIR	Small Business Innovation Research
SDL	Spectra Diode Laboratories
SEO	Schwartz Electro-Optics
SHG	second harmonic generation
SROL	stable relaxation-oscillation laser
Ti:Al <sub>2</sub> O <sub>3</sub>	titanium-doped sapphire

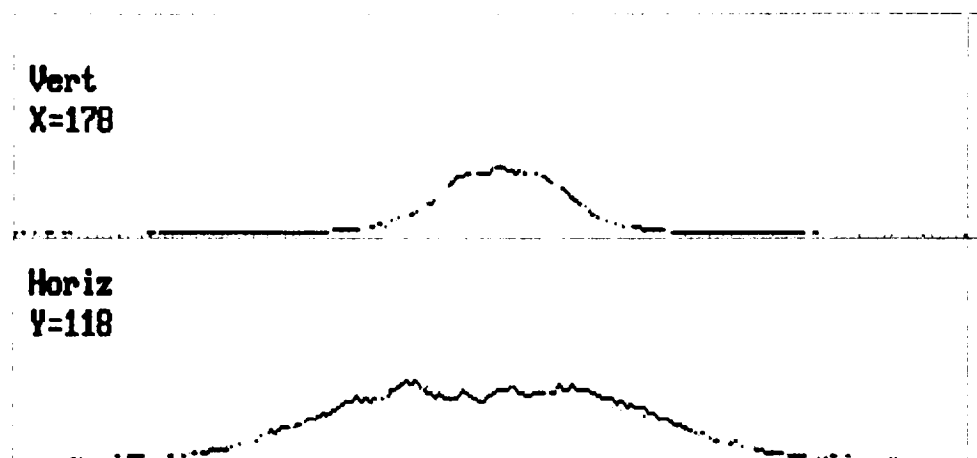
### **13 Appendix A: 10-W Diode Laser Pump Profiles**

Pump intensity profiles for the focused, 10-W, diode-laser are presented on the following pages. See Section 8.2.2 and the individual figure captions for a description of the experimental conditions.

	Vert	Horiz
Correlation Coeff.	= 0.982	0.945
Peak Position	= 122	178
Beam Dia. @ $1/e^2$ [mm]	= 1.628	3.347
Percent of Peak	= 32.9%	38.403

Cursor Location
<b>CENTROID</b>
(X,Y) = (178,118)
Profile Location
X (Vert) = 178
Y (Horiz) = 118

Active Cursor: Contour



LEFT MOUSE BUTTON draws profile.

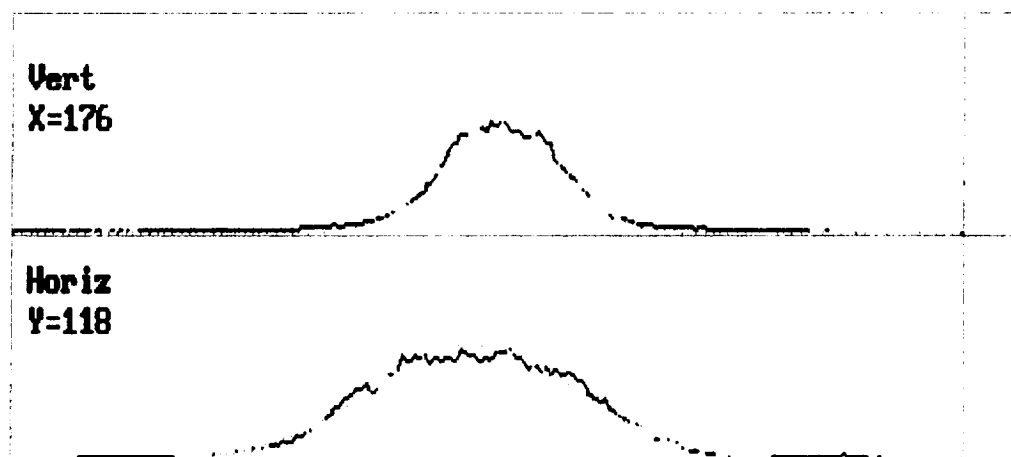
Press <ESC> to abort printing.

Figure A-1. Profile of the 10-W cw diode laser pump beam, 3 mm before the focus.

(Gaussian fit data)		
	Vert	Horiz
Correlation Coeff.	= 0.972	0.957
Peak Position	= 122	176
Beam Dia. @ $1/e^2$ [mm]	= 1.557	2.378
Percent of Peak	= 54.497	54.276

Current Location	
<b>CENTROID</b>	
(X,Y) = (176,118)	
Profile Location	
X (Vert)	= 176
Y (Horiz)	= 118

Active Cursor: Contour



LEFT MOUSE BUTTON draws profile.

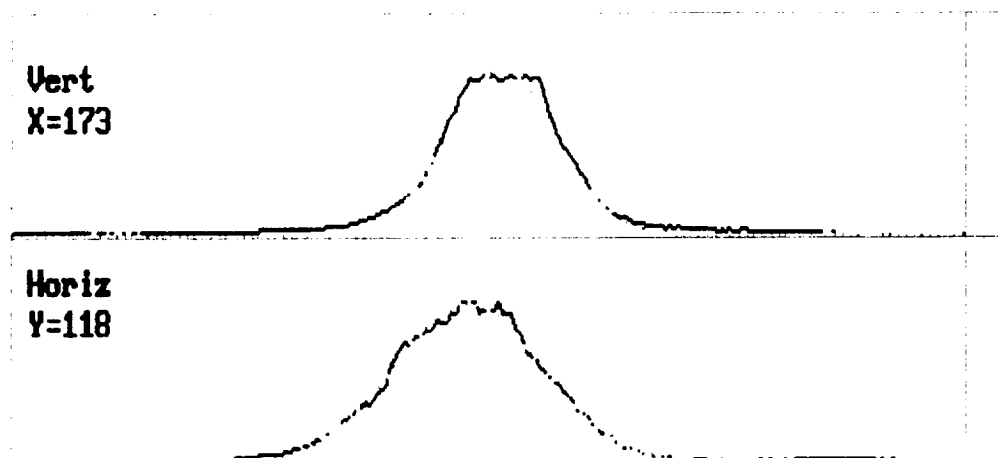
Press <ESC> to abort printing.

Figure A-2. Profile of the 10-W cw diode laser pump beam, 2 mm before the focus.

	Vert	Horiz
Correlation Coeff.	= 0.968	0.971
Peak Position	= 122	174
Beam Dia. @ 1/e <sup>2</sup> [mm]	= 1.463	1.711
Percent of Peak	= 79.277	74.356

Cursor Location  
**CENTROID**  
 (X,Y) = (173,118)  
 Profile Location  
 X (Vert) = 173  
 Y (Horiz) = 118

Active Cursor: Contour



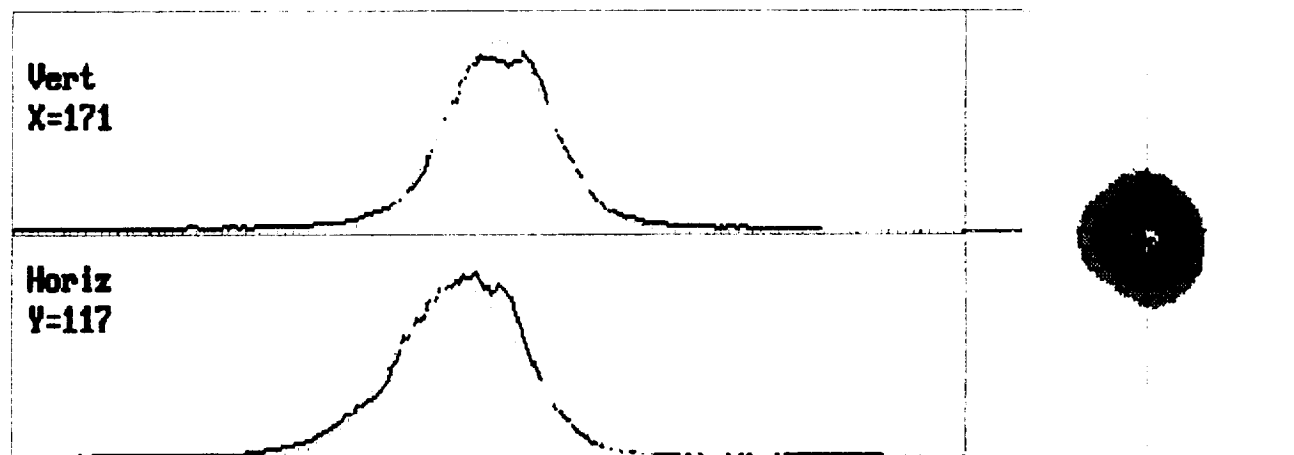
LEFT MOUSE BUTTON draws profile.

Press <ESC> to abort printing.

Figure A-3. Profile of the 10-W cw diode laser pump beam, 1 mm before the focus.

(Gaussian Fit Data)			(Cursor Location)	
	Vert	Horiz	CENTROID	
Correlation Coeff.	= 0.959	0.946	(X,Y) = (171,117)	
Peak Position	= 121	172	-Profile Location-	
Beam Dia. @ 1/e <sup>2</sup> [mm]	= 1.438	1.481	X (Vert) = 171	
Percent of Peak	= 91.732	81.382	Y (Horiz) = 117	

Active Cursor: Contour



LEFT MOUSE BUTTON draws profile.

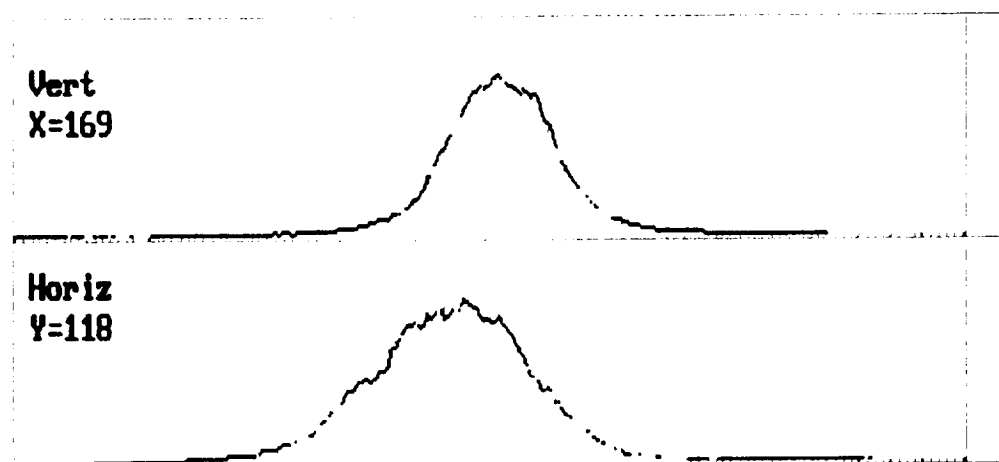
Press <ESC> to abort printing.

Figure A-4. Profile of the 10-W cw diode laser pump beam, at the focus.

	Vert	Horiz
Correlation Coeff.	= 0.969	0.958
Peak Position	= 122	169
Beam Dia. @ $1/e^2$ [mm]	= 1.411	1.790
Percent of Peak	= 75.868	74.425

Cursor Location  
**CENTROID**  
 (X,Y) = (169,118)  
 Profile Location  
 X (Vert) = 169  
 Y (Horiz) = 118

Active Cursor: Contour



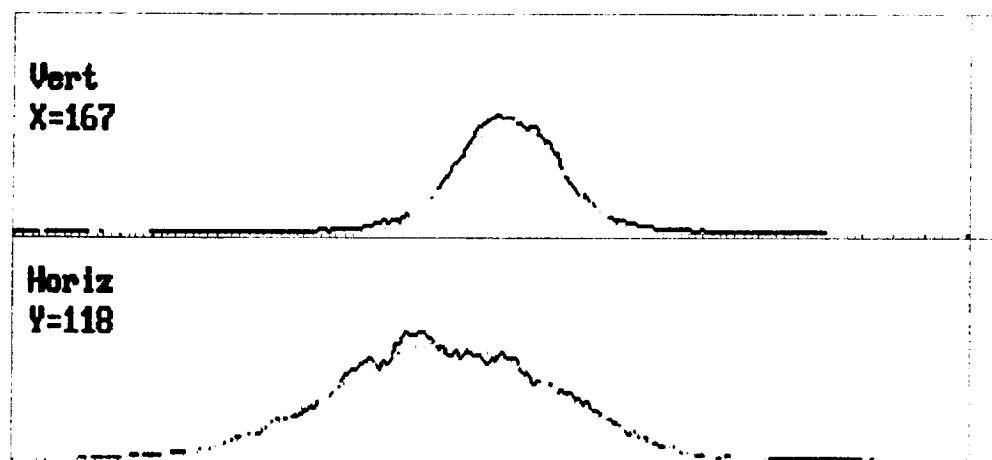
LEFT MOUSE BUTTON draws profile.

Press <ESC> to abort printing.

Figure A-5. Profile of the 10-W cw diode laser pump beam, 1 mm after the focus.

<Gaussian Fit Data>			<Cursor Location>	
	Vert	Horiz	<b>CENTROID</b>	
Correlation Coeff.	= 0.975	0.958	(X,Y) = (167,118)	
Peak Position	= 122	167	-Profile Location-	
Beam Dia. @ 1/e <sup>2</sup> [mm]	= 1.376	2.552	X (Vert) = 167	
Percent of Peak	= 55.113	55.431	Y (Horiz) = 118	

Active Cursor: Contour



LEFT MOUSE BUTTON draws profile.

Press <ESC> to abort printing.

Figure A-6. Profile of the 10-W cw diode laser pump beam, 2 mm after the focus.

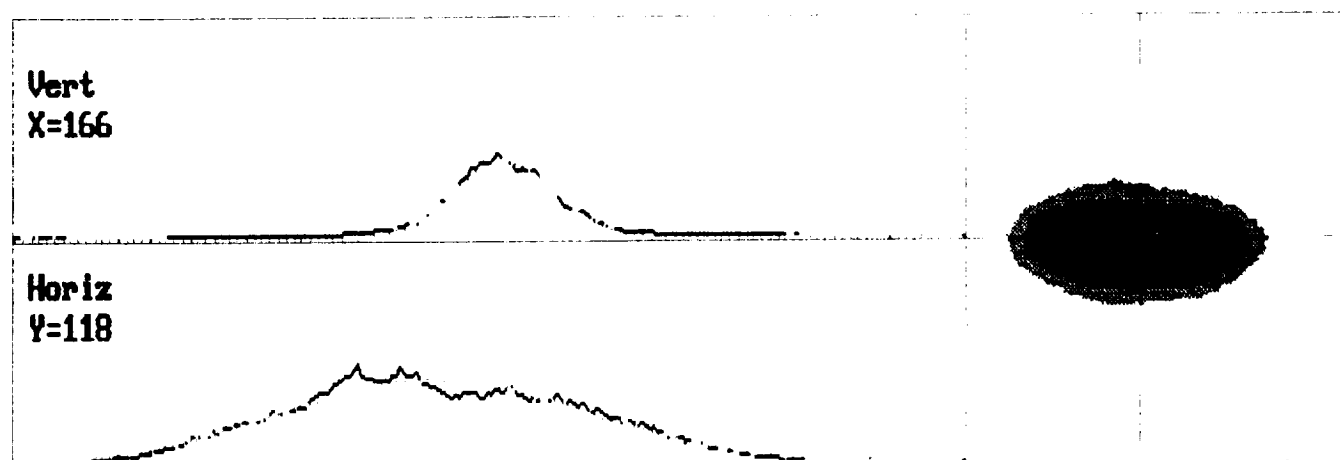




<Gaussian Fit Data>		
	Vert	Horiz
Correlation Coeff.	= 0.981	0.946
Peak Position	= 123	165
Beam Dia. @ $1/e^2$ [mm]	= 1.361	3.688
Percent of Peak	= 37.393	40.857

<Cursor Location>
<b>CENTROID</b>
(X,Y) = (166,118)
Profile Location-
X (Vert) = 166
Y (Horiz) = 118

Active Cursor: Contour



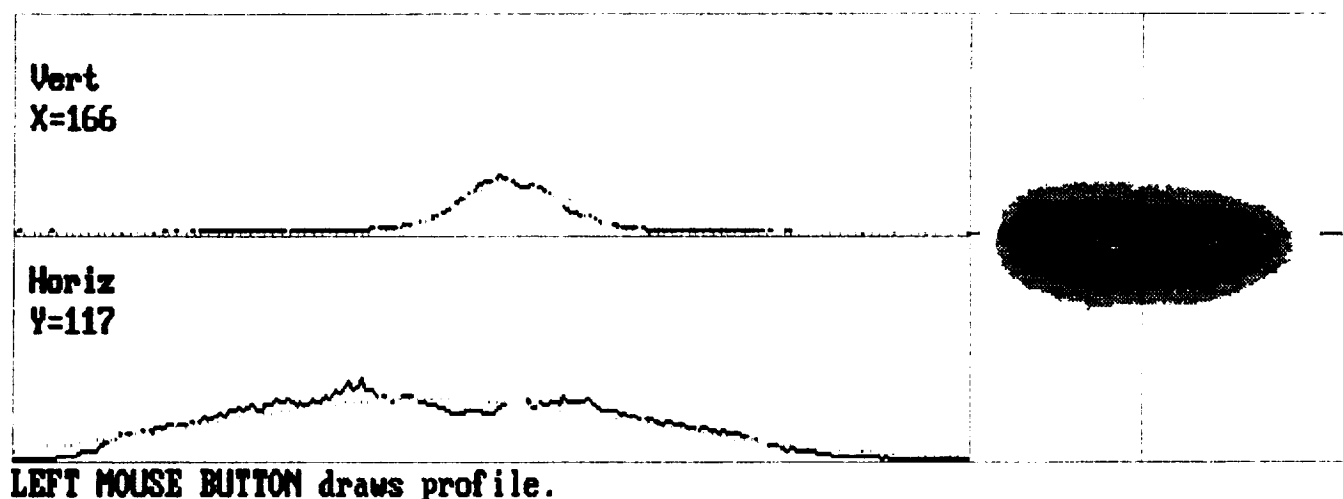
LEFT MOUSE BUTTON draws profile.

Press <ESC> to abort printing.

Figure A-7. Profile of the 10-W cw diode laser pump beam, 3 mm after the focus.

<Gaussian Fit Data>			<Cursor Location>	
	Vert	Horiz	<b>CENTROID</b>	
Correlation Coeff.	= 0.986	0.935	(X,Y) = (166,117)	
Peak Position	= 123	162	-Profile Location-	
Beam Dia. @ 1/e <sup>2</sup> [mm]	= 1.344	5.089	X (Vert) = 166	
Percent of Peak	= 25.737	29.154	Y (Horiz) = 117	

Active Cursor: Contour



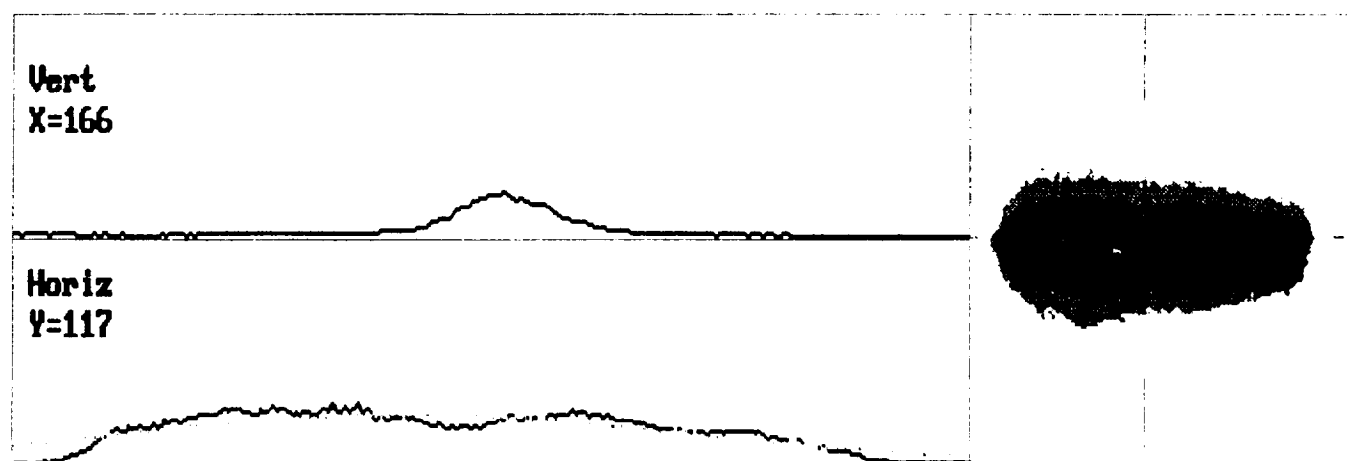
Press <ESC> to abort printing.

Figure A-8. Profile of the 10-W cw diode laser pump beam, 4 mm after the focus.

<Gaussian Fit Data>		
	Vert	Horiz
Correlation Coeff.	= 0.000	0.916
Peak Position	= 0	158
Beam Dia. @ 1/e <sup>2</sup> [mm]	= 0.000	6.487
Percent of Peak	= 0.000	23.634

<Cursor Location>	
<b>CENTROID</b>	
(X,Y) = (166,117)	
Profile Location-	
X (Vert)	= 166
Y (Horiz)	= 117

Active Cursor: Contour



LEFT MOUSE BUTTON draws profile.

Press <ESC> to abort printing.

Figure A-9. Profile of the 10-W cw diode laser pump beam, 5 mm after the focus.

## **14 Appendix B: CW Laser Development -- Recent Results**

Further experiments were recently carried out with the diode-pumped, intracavity-doubled, cw, Nd:YLF laser described in Section 8 of this report. These additional experiments, which were performed under separate funding, are presented in this Appendix. Recent advances in SHG output power obtained from the laser are described in Section 14.1. High-frequency noise measurements are presented and discussed in Section 14.2.

### **14.1 Increased SHG Output Power**

Previously we reported SHG output of 900 mW in a single beam from the cw, green laser. This was obtained with the configuration shown in Figure 8-22, using a dual-band HR to combine the bidirectional green into a single output. We made several modifications and improvements to the resonator configuration, as described below, and obtained 1.25 W of total SHG output in two beams.

We modified the resonator design so that only one cylindrical HR was required, instead of two, to compensate for the asymmetric thermal lensing. This required a slight modification of the mode size in the crystal and a small change in the cylindrical radius of the HR. This modification simplified the resonator optics, and also allowed us to outcouple the SHG through a flat optic instead of a cylinder.

We obtained higher-quality substrates and coatings for the cylindrical HR and the flat HR. The previous coatings were more lossy than expected at 1047 nm, which degraded the performance of the laser. The new coatings showed better performance as 1047-nm high reflectors.

We mounted the LBO crystal in a heated ceramic cell designed at SEO. We also built a plexiglass cover for the laser, to protect the LBO crystal from air currents. The improvements in power stability resulting from these changes have already been discussed in Section 8.4.3.

We replaced the 5-cm-focal-length lens and flat HR at the end of the resonator with a single 5-cm-concave HR. This preserved the same resonator mode, while eliminating two intracavity surfaces. No adverse alignment sensitivity effects were observed in the new configuration. A dual-band HR was not readily available in the 5-cm-concave radius, so the mirror we used was only a 1047-nm HR. For this reason we obtained two green output beams.

The new laser configuration is shown in Figure B-1. (This is the configuration in which the laser was delivered to NASA LaRC.) With this laser we obtained a total of 1.25 W of output at 523.5 nm, with 10 W of pump power delivered to the Nd:YLF crystal. The output was in two beams, with approximately 575 mW in one beam and 675 mW in the other. Our previous experience indicates that the same output power could be obtained in a single beam by replacing the 5-cm-cc, 1047-nm HR with a 5-cm-cc, dual-band HR. However, the laser displays more high-frequency intensity noise in the single-output configuration, as discussed in the next section.

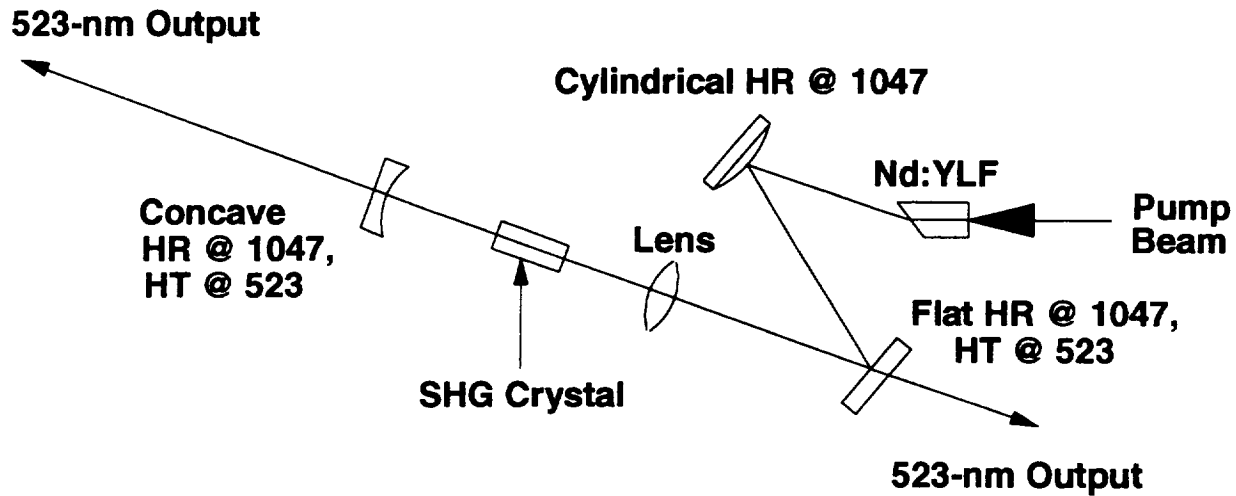


**Figure B-1.** Modified cw green laser configuration.

## 14.2 High-Frequency Noise Measurements

Chaotic high-frequency intensity noise is typical of diode-pumped, cw, intracavity-doubled Nd lasers, as described by Baer and others [13,14]. The noise arises from coupling of longitudinal modes through the nonlinear second harmonic generation effect in the intracavity SHG crystal. A variety of different approaches have been investigated to overcome this so-called "green problem," such as single-frequency operation [13], intracavity polarization rotation schemes [15], and birefringent filter techniques [16]. Our baseline design was for a single-frequency ring laser, since single-frequency operation appears to be a straightforward solution to the noise problem. However, the ring laser performance was not satisfactory in other respects (see Section 8.3.3). We accordingly proceeded with a standing-wave design, anticipating the need to measure, characterize, and minimize any observed high-frequency noise.

We measured and characterized the high-frequency intensity noise in the fundamental and SHG output beams under various operating conditions. This high-frequency noise is independent of the long-term power stability of the laser. Throughout these measurements the laser displayed excellent long-term stability at SHG output power levels up to 1.25 W. However, chaotic high-frequency intensity noise was present, its magnitude depending on the particular laser configuration.

Two types of noise measurements were performed. A Stanford Research Systems SR770 FFT Network Analyzer was used to obtain noise spectra in the 0 - 100 kHz frequency band. Data were stored on the network analyzer and later transferred to a computer for analysis. The

results were plotted as relative intensity noise normalized to unit Hz (RIN/Hz) vs. frequency. The RIN plots appear at the end of this section. In addition, peak-to-peak noise measurements were taken over various frequency ranges from 0 - 1 MHz using an oscilloscope.

The noise measurements were taken under various operating conditions, summarized as follows. Noise at the SHG wavelength was characterized in the configuration shown in Figure B-1. Noise at the fundamental wavelength was characterized by replacing the 5-cm-cc, 1047-nm HR with a 5-cm-cc, 1047-nm output coupler (1.85% T), which produced approximately 1.2 W of 1047-nm output. In each of these configurations, the effects of temperature-tuning the SHG crystal on and off phase-match were observed. The effects of angle-tuning the SHG crystal on and off normal incidence were investigated as well. In the case of angle-tuning off normal incidence, the SHG crystal had to be temperature-tuned from about 172°C to about 175°C in order to maintain phase-matching. Finally, the noise obtained with a single-output green beam (using a dual-band HR) was compared to the noise obtained with a dual-output green beam (using a 1047-nm HR).

The results of the noise measurements are summarized in Table B-1. Root mean square (rms) noise values are listed for various frequency ranges and operating conditions. The "OSC" column lists rms noise values obtained from peak-to-peak noise readings on the oscilloscope. The "FFT" column lists rms noise values obtained from the FFT network analyzer by integrating the RIN data over frequency and taking the square root. These two methods are not in perfect agreement due to several factors: the subjective choice of a representative frequency in a given range on the oscilloscope; different filtering in the oscilloscope and the FFT digitizer; and averaging of FFT spectra over 20 sweeps.

The data clearly indicate that in some configurations the laser suffers from severe intensity noise, with rms noise values up to 30% or higher in the 0 - 1 MHz frequency band. The severe chaotic noise occurs only in the presence of nonlinear outcoupling. When nonlinear outcoupling is not present (no SHG), the noise in the fundamental beam is reduced to 2-3% rms. The magnitude of the chaotic noise when nonlinear outcoupling is present depends on the laser configuration. The highest noise values occur in the 1-beam SHG output configuration, in which one of the green output beams is redirected back through the SHG crystal. Greater noise also occurs when the SHG crystal faces are at normal incidence; the noise is reduced when the crystal is angle-tuned a few degrees off normal incidence. These observations indicate that the magnitude of the chaotic noise increases drastically when there is optical feedback to the SHG crystal, either from the redirected green beam or from the SHG crystal faces. Therefore it is necessary to minimize the optical feedback in the resonator.

The minimum SHG noise occurs in the 2-beam output configuration with the SHG crystal angle-tuned a few degrees off normal incidence. This configuration essentially minimizes optical feedback to the SHG crystal. In this configuration, rms noise values of 2-3% in the 0 - 1 MHz frequency range were measured at SHG output levels over 1 W. This is the configuration in which the laser was delivered to NASA LaRC.

**Table B-1. RMS Noise Values**

Wavelength: SHG Output: Temp-tuning: Angle-tuning:	523 nm 1-beam on p-m off nrml		523 nm 2-beam on p-m off nrml		1047 nm -- off p-m off nrml		1047 nm -- on p-m nrml	
Frequency Range:	OSC	FFT	OSC	FFT	OSC	FFT	OSC	FFT
0 - 100 Hz	1.2%		0.4%		0.1%		0.7%	
0 - 1 kHz	6%		0.6%		0.13%		2.0%	
0 - 10 kHz	18%	8%	1.4%	0.4%	0.4%	0.1%	7.9%	2.9%
0 - 100 kHz	32%	23%	2.4%	1.0%	2.0%	1.4%	30%	18.5%
0 - 1 MHz	38%		3%		2.6%		43%	

In summary, we were able to demonstrate a configuration of the laser in which the SHG noise level was 2-3% rms in the 0 - 1 MHz frequency band. (For comparison, a typical Ar-ion laser noise specification is 0.5% rms over the 10 Hz - 2 MHz frequency band.) This is still significant noise, and for applications that require high stability the laser might not be suitable. However, for this application, pumping the  $\text{Ti:Al}_2\text{O}_3$  master oscillator in a lidar system, the noise is probably within acceptable limits. Small fluctuations in master oscillator output are not likely to affect the injection-seeding process.

While the minimum noise level that we demonstrated is probably adequate for this application, lower noise would certainly be preferred. One advantage of a low-noise master oscillator would be to provide a low-noise probe for monitoring the length of the slave-oscillator resonator. This would be desirable for "locking" the injection seeder to a single longitudinal mode of the slave oscillator. We are therefore considering further noise-minimization techniques. The single-frequency-operation technique has already been discussed. In addition, a recent report [17] suggests that low-noise operation of an intracavity-doubled, Nd laser may be achieved while running many longitudinal modes. In that report the spot size ratio between the gain medium and the SHG crystal is described as an important parameter. Another approach would be to further characterize and reduce the "fundamental" laser noise due to factors other than nonlinear

outcoupling and feedback. For example, there is a noise signature around 90 kHz that may be related to the diode switching power supply. In any case, noise minimization will be one important task to be pursued in future cw green laser development.

The RIN noise plots obtained with the FFT network analyzer appear in Figures B-2 and B-3. Figure B-2 shows the noise in the 1047-nm output beam with the SHG crystal temperature-tuned on/off phase-match (nonlinear outcoupling present/not present). It also shows the further noise reduction obtained by angle-tuning the SHG crystal off normal incidence. Figure B-3 shows the noise in the 523-nm output beam under various conditions, 1-beam vs. 2-beam and normal-incidence vs. off-normal-incidence. As described above, the lowest noise occurs in the 2-beam output configuration with the SHG crystal angle-tuned off normal incidence. Note that relative intensity noise is defined as

$$RIN = \langle \Delta P \rangle^2 / \langle P \rangle^2$$

where  $\langle P \rangle$  is the average laser intensity, and  $\langle \Delta P \rangle$  is the rms intensity fluctuation spectral density.  $\langle \Delta P \rangle$  is normalized to unit  $\text{Hz}^{1/2}$ , and RIN to unit Hz, to allow equivalent noise comparisons over different bandwidths. In order to convert from RIN data to rms noise values, it is necessary to integrate over frequency and take the square root.



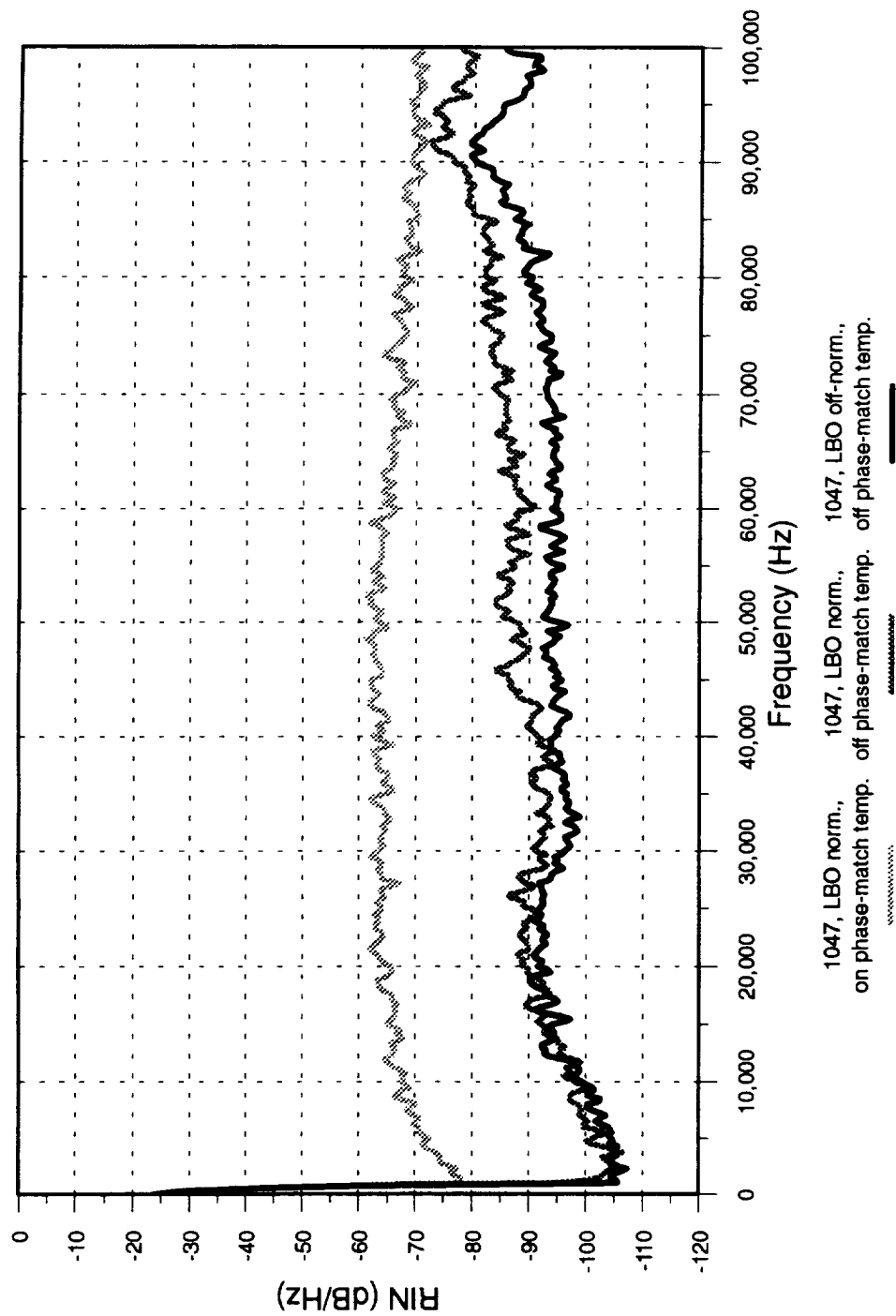


Figure B-2. Relative intensity noise data at the fundamental wavelength.

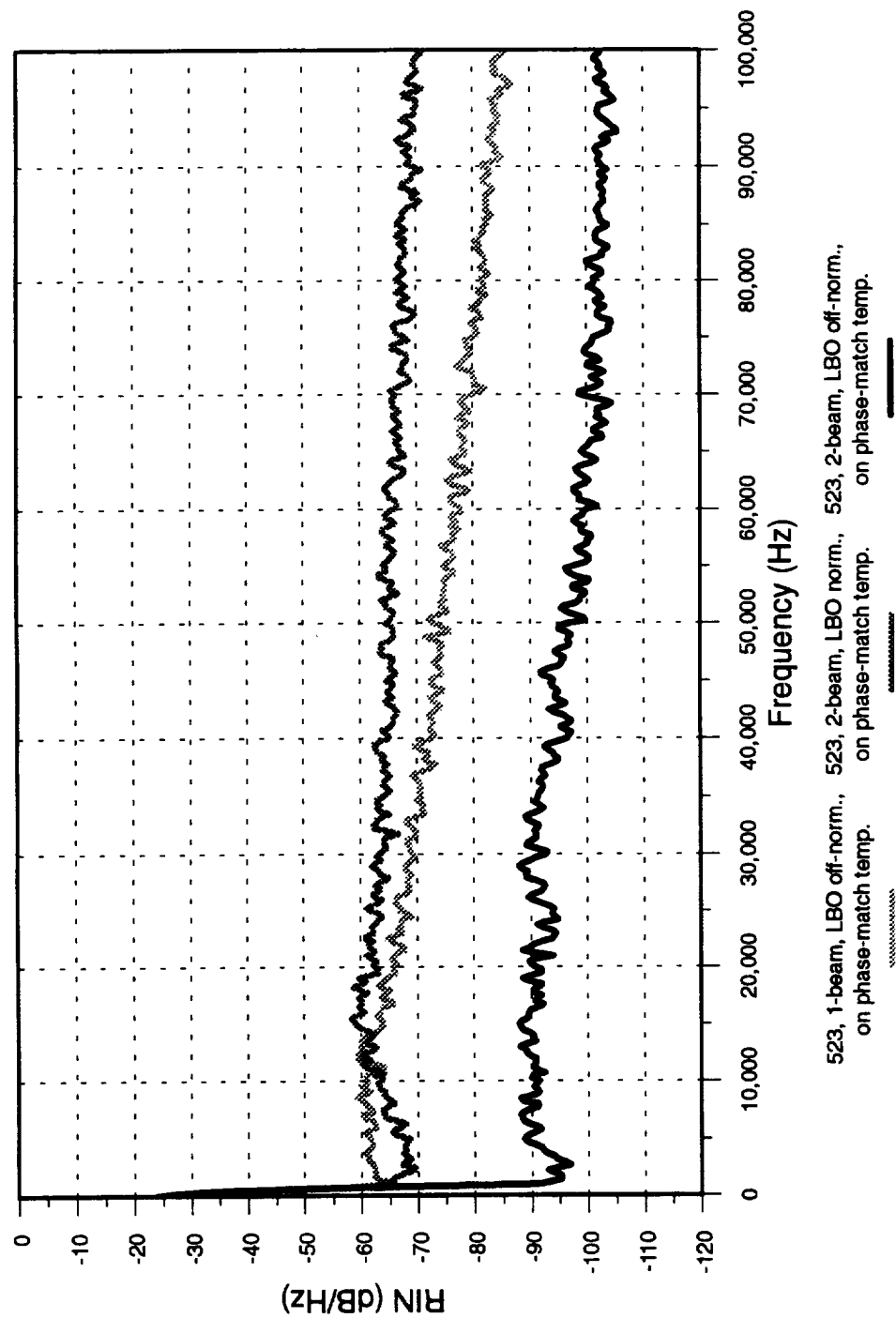


Figure B-3. Relative intensity noise data at the second harmonic wavelength.





REPORT DOCUMENTATION PAGE			Form Approved OMB No. 0704-0188	
Public reporting burden for this collection of information is estimated to average 1 hour per response, including the time for reviewing instructions, searching existing data sources, gathering and maintaining the data needed, and completing and reviewing the collection of information. Send comments regarding this burden estimate or any other aspect of this collection of information, including suggestions for reducing this burden, to Washington Headquarters Services, Directorate for Information Operations and Reports, 1215 Jefferson Davis Highway, Suite 1204, Arlington, VA 22202-4302, and to the Office of Management and Budget, Paperwork Reduction Project (0704-0188), Washington, DC 20503.				
1. AGENCY USE ONLY (Leave blank)	2. REPORT DATE March 1994	3. REPORT TYPE AND DATES COVERED Contractor Report, 4/10/91 - 12/17/93		
4. TITLE AND SUBTITLE Development of Lasers Optimized for Pumping Ti:Al <sub>2</sub> O <sub>3</sub> Lasers		5. FUNDING NUMBERS  C NAS1-19304  WU 324-02-03		
6. AUTHOR(S)  Glen A. Rines and Richard A. Schwarz				
7. PERFORMING ORGANIZATION NAME(S) AND ADDRESS(ES) Schwartz Electro-Optics, Inc. Research Division 45 Winthrop Street Concord, MA 01742		8. PERFORMING ORGANIZATION REPORT NUMBER		
9. SPONSORING/MONITORING AGENCY NAME(S) AND ADDRESS(ES)  National Aeronautics and Space Administration Langley Research Center Hampton, VA 23681-0001		10. SPONSORING/MONITORING AGENCY REPORT NUMBER  NASA CR-4573		
11. SUPPLEMENTARY NOTES Langley Contracting Officer's Technical Representative: James Barnes Final Technical Report				
12a. DISTRIBUTION/AVAILABILITY STATEMENT  Unclassified - Unlimited  Subject Category 36			12b. DISTRIBUTION CODE	
13. ABSTRACT (Maximum 200 words)  On this project we completed laboratory demonstrations of: 1) an all-solid-state, broadly tunable, single-frequency, Ti:Al <sub>2</sub> O <sub>3</sub> master oscillator, and 2) a technique for obtaining "long" (nominally 100- to 200-ns FWHM) laser pulses from a Q-switched, Nd oscillator at energy levels commensurate with straightforward amplification to the joule level.  We designed, constructed and evaluated a diode-laser-pumped, Nd:YLF laser with intracavity SHG. With this laser we obtained greater than 0.9 W of cw, output power at 523.5 nm with 10 W of diode-laser pump power delivered to the Nd:YLF crystal. With this laser as a pump source, we demonstrated, for the first time, to our knowledge, an all-solid-state, single frequency, Ti:Al <sub>2</sub> O <sub>3</sub> laser with sufficient output power to injection seed a high-energy oscillator over a 200-nm bandwidth.  The pulsed laser work succeeded in demonstrating pulse-stretching in a Q-switched Nd:YAG oscillator. We obtained greater than 50-mJ pulse energies in pulses with 100- to 200-ns pulsewidths (FWHM).				
14. SUBJECT TERMS  titanium sapphire lasers, neodymium lasers, diode-laser-pumped, Nd:YLF			15. NUMBER OF PAGES 108	
			16. PRICE CODE A06	
17. SECURITY CLASSIFICATION OF REPORT Unclassified	18. SECURITY CLASSIFICATION OF THIS PAGE Unclassified	19. SECURITY CLASSIFICATION OF ABSTRACT	20. LIMITATION OF ABSTRACT	



National Aeronautics and  
Space Administration  
Langley Research Center  
Mail Code 180  
Hampton, VA 23681-00001

---

Official Business  
Penalty for Private Use, \$300

**BULK RATE**  
**POSTAGE & FEES PAID**  
NASA  
Permit No. G-27

